UNIVERSITY OF CALIFORNIA,

IRIVNE

# Understanding Ferryl Basicity And Proximal Histidine Ligation

DISSERTATION

submitted in partial satisfaction of the requirements

for the degree of

DOCTOR OF PHILOSOPHY

In Biological Sciences

by

Aaron Patrick Ledray

Dissertation Committee:

Professor Michael T. Green, Chair

Professor Celia W. Goulding

Professor Thomas L. Poulos

2021

# DEDICATION

To my parents, my sister, and all the friends met along the way on this incredible journey:

It’s been a genuine dream come true, and I owe it all to you.

# TABLE OF CONTENTS

# LIST OF FIGURES

# LIST OF TABLES

# ACKNOWLEDGEMENTS

I would first like to acknowledge Dr. William Safranek, who started me down this path by lending me a pathogenic microbiology textbook as a second-year undergraduate student. He introduced me to the research world and was my first academic role model. We lost professor Safranek in 2014, but his memory continues to be an inspiration. He left a deep impression with his passion as an educator and joy as a researcher.

My undergraduate advisor, Dr. Stephen J. King, took a chance on me as an undergraduate and gave me plenty of room to develop my own projects. This was by far the most beneficial educational experience I had and including me with group trips to national conferences was wildly inspirational. His laboratory gave me enough responsibility to feel like I had a purpose in science and like I belonged as a scientist – I am exceptionally grateful for having that opportunity.

My Ph.D. advisor Dr. Michael T. Green brought me into the group as a student without much of a chemistry background. I am extremely thankful for the time I had in his group to explore spectroscopy and structure, and the wide room to express myself throughout the journey. I learned methods I never heard of and went to national laboratories to perform my own experiments around-the-clock. In the Green lab, I learned that science can be an adventure, that extreme data scrutiny pays off, and how to conduct myself as a serious researcher.

Finally, I would like to thank my labmates for their support keeping the ship afloat, help with trips to the synchrotron, and growing with me over the past few years. I would particularly like to thank my colleague and friend Dr. Kaustuv Mittra, who taught me plenty of chemistry, but more importantly, learned plenty more chemistry with me.

# VITA

B.S. in Biotechnology and Biomedical Sciences, minors in Chemistry and Music (2015)

Laboratory of Dr. Stephen J. King (2013-2015)
University of Central Florida

Ph.D. in Biological Sciences (2021)

Laboratory of Dr. Michael T. Green (2015 – 2021)

University of California, Irvine

## SELECT PUBLICATIONS

1. Ledray AP, Mittra K, Green MT. NRVS Investigation of Ascorbate Peroxidase Compound II: Observation of Iron(IV)oxo Stretching. [accepted] J. Inorg. Biochem.

2. Ledray AP, Krest C, Yosca T, Mittra K, Green MT. Ascorbate Peroxidase Compound II is an Iron(IV)oxo Species. J. Am. Chem. Soc. 2020, 142, 48, 20419-20425. PMID: 33170000.

3. Bierma JC, Roskamp KW, Ledray AP, Kiss AJ, Cheng CC, Martin RW. Controlling Liquid-Liquid Phase Separation of Cold-Adapted Crystallin Proteins from the Antarctic Toothfish. J Mol Biol. 2018 Dec 7;430(24):5151-5168. PMID: 30414964.

4. Sabblah TT, Nandini S, Ledray AP, Pasos J, Calderon JLC, Love R, King LE, King SJ. A novel mouse model carrying a human cytoplasmic dynein mutation shows motor behavior deficits consistent with Charcot-Marie-Tooth type 2O disease. Sci Rep. 2018 Jan 29;8(1):1739. PMID: 29379136.

5. Yosca TH, Ledray AP, Ngo J, Green MT. A new look at the role of thiolate ligation in cytochrome P450. J Biol Inorg Chem. 2017 Apr;22(2-3):209-220. PMID: 28091754.

# ABSTRACT OF THE DISSERTATION

Understanding Ferryl Basicity

And Proximal Histidine Ligation

By

Aaron Patrick Ledray

Doctor of Philosophy in Biological Sciences

University of California, Irvine, 2021

Professor Michael T. Green, Chair

Our current understanding of biological C-H bond activation in heme enzymes points to an important role of basic ferryl intermediates in how Nature supports this chemistry. Among heme proteins, only the thiolate-ligated enzymes have been demonstrated to react with unactivated C-H bonds. Strong electron donation from the proximal thiolate ligand results in a basic Compound II species, an iron(IV) hydroxide. This is important for balancing the reduction potential of Compound I and avoiding deleterious autoxidation of the protein superstructure. However, recent neutron crystallography experiments point to a basic ferryl species present in a histidine-ligated heme enzyme as well, which have been previously shown to only support unprotonated oxos. Our work demonstrates that ascorbate peroxidase, the histidine-ligated heme enzyme, really has an unprotonated iron(IV) oxo Compound II species (APX-II). We further examine the iron(III)

hydroxide state of ascorbate peroxidase in order to better understand the reported crystal structure and what it represents. We conclude with a vibrational spectroscopic method to observe the Fe-O bond in APX-II and assign it to an Fe(IV) to a doubly bound oxygen atom, split between multiple vibrational modes resulting in apparent stretching frequencies of 770 and 732 $cm^{-1}$, or 1.67 and 1.69 Å, respectively. This is well within range of what is expected for an iron(IV) oxo.

# Chapter I: Introduction:

## Heme and heme-containing enzymes:

Heme-containing proteins can be found throughout Nature, serving an impressively broad range of biological functions. While not every form of life uses heme, there is strong evidence that heme biosynthesis dates back to the last universal common ancestor (LUCA) between the domains Archaea and Bacteria.[1] The range of functions of heme proteins span from enzymes that catalyze reactions that break some of the most difficult to rupture bonds commonly encountered (the unactivated C-H bond) to proteins that gingerly bind $O_2$ reversibly as part of physiological respiration, such as hemoglobin. A long-standing goal of heme protein research is to understand how Nature tunes the common elements around the heme cofactor to afford different reactive pathways, such as between systems that bind dioxygen and systems that use oxygen to react with substrates.

The heme cofactor is shown in Figure 1.1 in two representations. The protoporphyrin IX macrocycle is a tetrapyrrole ring without a central atom. With the addition of an iron atom, the molecule is called heme. The four ligating nitrogen atoms of the protoporphyrin IX molecule act as equatorial ligands but leave the axial ligands free. The depiction of the ring around a central Fe atom, shown at the top-right of the figure, represents heme and allows for depiction of the distal and proximal axial ligands to be included. Shown in Figure 1.1 is a 6-coordinate heme system, with a proximal ligand from a protein R-group histidine, and a distal ligand of an oxygen atom with a bond order of 2. In heme enzymes, the proximal ligand is the primary influence upon the electronic structure of the central Fe atom. In enzymes, the proximal ligand always is a protein amino acid residue, which additionally tethers the cofactor to the protein.

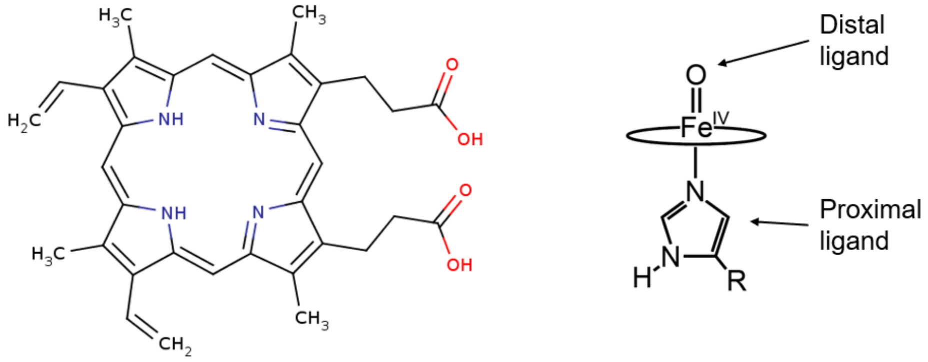

Protoporphyrin IX

6-coordinate heme system

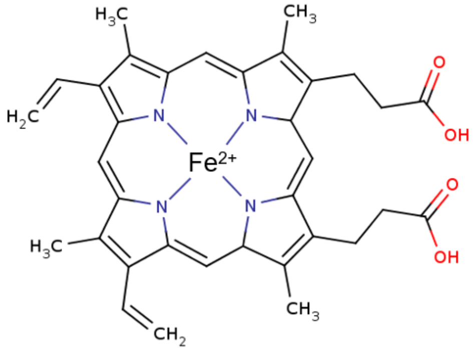

Heme

**Figure 1.1**: The heme macrocycle. (Top Left): Protoporphyrin IX consists of the ring without a central metal atom. (Bottom): Heme is the protoporphyrin IX macrocycle with a central Fe atom. Note, no proximal or distal ligands are present. (Top right): Heme-cartoon depiction of an intermediate in an enzyme. The ring represents the protoporphyrin IX macrocycle. The proximal ligand here comes from a histidine protein R-group, from beneath the heme plane. Depicted is heme b.

There are different types of heme as well – shown in Figure 1.1 is heme b. The c-type hemes are covalently attached to the protein through thioether linkages to vinyl carbons on the ring (via a CxxCH heme-binding motif) which provides structural stability when compared to heme b counterparts.[2,3] By serving as an adapter molecule for an iron atom, heme allows Life to exploit Fe(II)/Fe(III)/Fe(IV) redox to serve a wide range of cellular functions. While modification to the heme macrocycle is a point of variation, properties such as reduction potential can be more readily tuned over a wide range using just the protein folding environment.[2,4,5] Considering only bis-His axial ligation, heme b is found with a range of potentials from -150 to +380 meV vs. NHE, while heme c proteins have a range of potentials from -450 to +380 meV.[6] The covalent bond has an effect on the spin state of the iron atom, but much more of the focus on the role of the additional linkage in heme c versus heme b has been on the stability of enzymes.[7,8]

Broadly speaking, the heme cofactor's utility is dictated by the protein, but the primary distinguishing features remain in close proximity to the porphyrin macrocycle. The capacity for a heme enzyme to react *in vivo* is controlled by how the heme is made accessible and at what point in the catalytic process. This is choreographed by a ballet of other enzymes, such as reduction partners which use NADH or NADPH as a cofactor to reduce cytochrome P450 (a heme enzyme) prior to binding $O_2$ and building up to the oxidative power of the reactive intermediate species, all of which is permitted only after the enzyme has bound to substrate and started down the reaction pathway.[9] By controlling when the oxidative intermediate is generated to only when the substrate is already bound through requiring the reduction partners to recognize only the substrate-bound state, Nature has produced a control point that stops the investment of cellular resources into non-productive chemical reactions.

Figure 1.2 shows three proteins containing heme b in order to highlight structural/functional diversity from the protein environment tuning the cofactor. Depicted are a subunit of hemoglobin, horseradish peroxidase (HRP), and cytochrome P450. Hemoglobin is a multimeric protein that binds reversibly to dioxygen by alternating between two conformational states, the low-affinity for oxygen T state and the high-affinity oxy R state.[10–12] Dioxygen is a small molecule compared to the substrate molecules for P450 and horseradish peroxidase – while the propionates are observable at the surface in this depiction, in the tetrameric complex the heme groups are buried and the heme cofactors are hidden and not accessible to molecules larger than dioxygen. Oxygen affinity between the T and R states in the α and β subunits can be mostly attributed to proximal ligand changes that change the oxygen binding constrant.[11] HRP is a histidine-ligated heme system, like hemoglobin, but it instead natively reacts with hydrogen peroxide to oxidize a range of substrates. The active site of HRP is large and can bind a diverse array of substrate molecules,[13–15] whereas native myoglobin sterically hinders substrate access to the heme cofactor.[13,16,17] Additionally, HRP (typical for peroxidases) possesses an arginine residue in the distal pocket – this is important in the catalytic cycle for peroxidases, which we will discuss in a later section of this chapter.[17] P450 possess a thiolate proximal ligand as opposed to the histidine proximal ligand shown in Hb and HRP. The intermediate species produced during the catalytic cycle of P450 are more reactive and P450 enzymes accordingly have well-buried active sites clearly separated from solvent with predicted networks of channels connecting the buried heme cofactor to the surface.[18] Before P450 can produce reactive intermediates, substrates must first bind.[19] In this way, the spring-loading of P450's reactive mechanism requires that a target is already present, protecting the system from misfiring.

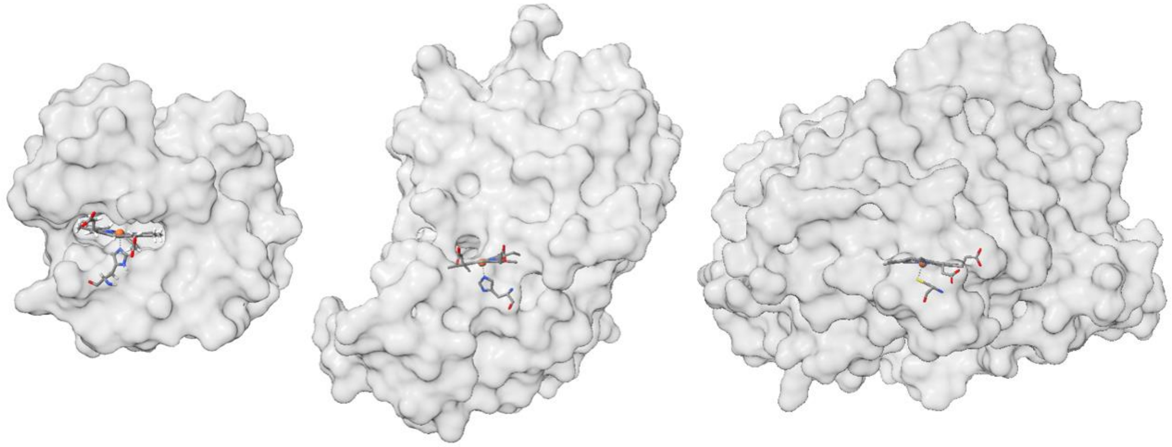

**Figure 1.2**: Surface projections of heme proteins. (Left): Hemoglobin subunit, PDB: 6BB5. (Middle): Horseradish peroxidase, PDB: 2ATJ. (Right): Cytochrome P450, PDB: 4ZFA. While the heme appears accessible in the hemoglobin model, in the multimeric form (the *in vivo* structure), the heme groups are well-buried.

The first reactive intermediate species is Compound I. In heme enzymes capable of C-H bond activation, this is referred to as the *active oxidant*.[20] This is because Compound I is the actual species to break the unreactive C-H bond as part of the H-atom abstraction mechanism, in which hydrogen atom transfer from a substrate molecule breaks the C-H bond and leaves a substrate radical.[21] Compound II in the context of P450 and other C-H bond activators is the *rebound intermediate*, a proposed short-lived species that exists before hydroxide ligand is transferred to a substrate carbocation.[20] In the context of peroxidases, Compound I is instead the *principal* oxidant, and Compound II is the *secondary* oxidant. Both are responsible for the one-electron oxidation of some substrate – but in the context of other long-studied systems such as ascorbate peroxidase, the role of the enzyme is more accurately to scuttle $H_2O_2$ from the cellular environment and Compounds I and II are steps to return to the catalytic resting state. In ascorbate peroxidase, Compounds I and II natively react with ascorbate, which is in ample supply and quickly returns the enzyme to the ferric oxidation state.[22] In peroxidases, Compound I is still an additional oxidation state above Compound II, but that additional electron equivalent is delocalized over the heme macrocycle. This results in an increased reactivity of Compound I as compared to compound II, but this is a very different situation than the Compound I / Compound II contrast with P450s that was mentioned earlier.

To that end, it is important to make nomenclature distinctions between the different heme enzymes according to their activity classifications. Figure 1.3 will assist in this. Peroxidases react with $H_2O_2$ and cleave the O-O bond to produce Compound I. Oxygenases are enzymes that bind to atmospheric dioxygen and cleave the O-O bond after weakening it over several steps. The ultimate fate of the oxygen atom from the dioxygen bound to an oxygenase is incorporation into substrate. Notably, oxygenases form an intermediate prior to Compound I formation that is the same as that formed from reacting a peroxide with $H_2O_2$, a Fe(III)-$OOH_2$ intermediate. This species can also be accessed in oxygenases by reacting directly with $H_2O_2$, via the *peroxide shunt*. In the following chapters of this text, the intermediate species Compounds I and II are prepared using a peroxyacid that forms the same Fe(III)-OOH intermediate observed in oxygenase activity. This species precedes the genuine peroxide shunt's Fe(III)-$OOH_2$ product, which generates Compound I upon releasing water.

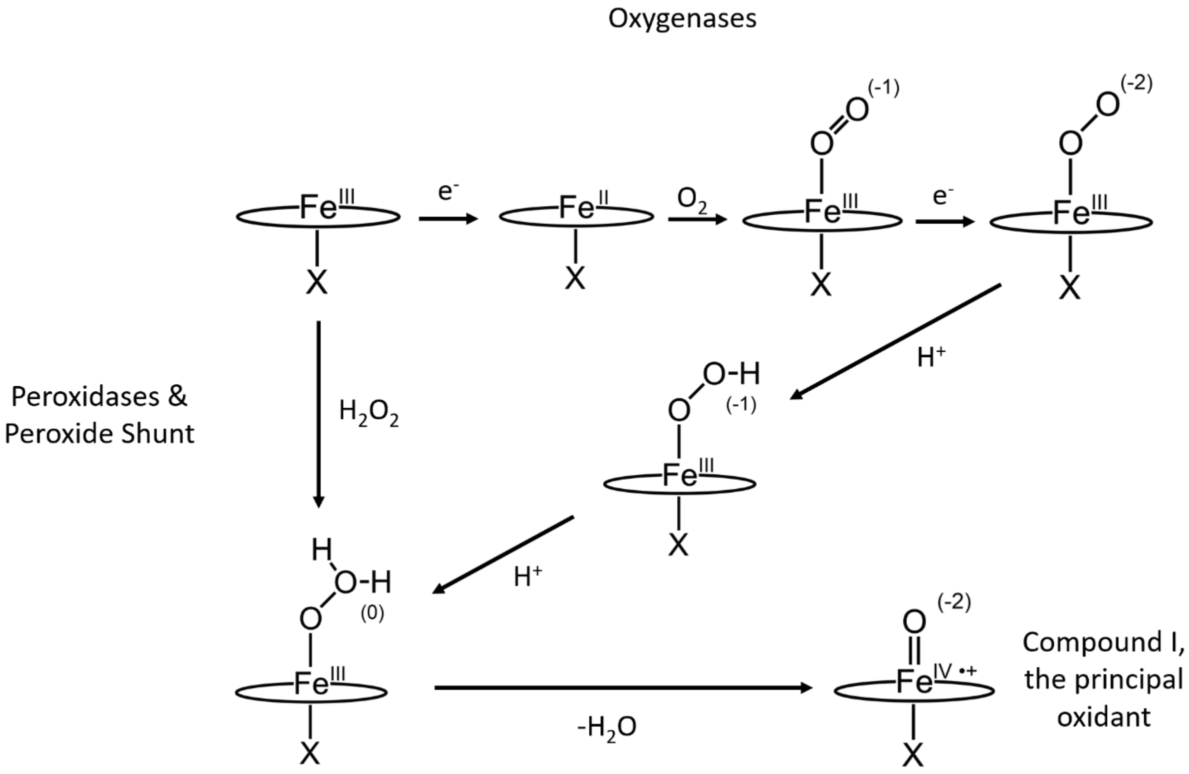

**Figure 1.3**: A broad overview of heme enzymes. The X represents a variable proximal ligand. Oxygenases will bind $O_2$ and break down the O-O bond. Peroxidases directly bind $H_2O_2$. Oxygenases may also directly bind $H_2O_2$, though they form the same intermediate species in the regular breaking of $O_2$.

Heme peroxidases generally have proximal nitrogen ligands from a histidine amino acid residue. In oxygenases like cytochrome P450, this is instead a sulfur atom from a cysteine residue. The proximal ligand serves as one of the major points of influence upon the heme cofactor's function – it is the thiolate ligand found in P450 and other heme monooxygenases that is behind the activation of molecular oxygen, which is a process that involves active site water molecules carefully coordinated to the dioxygen ligand.[20,23,24]

It is in conjunction between active site access and reactive capability, the heme oxygenase and peroxidase enzymes can tune the fate of the oxygen atom in Compound I. In order to understand how Nature can break the C-H bond, it is necessary to understand the forces that dictate the reactivity of Compound I.

While the surface and active site accessibility obviously has an important role in the function P450's substrate hydroxylation mechanism, this has more to do with restricting the buildup of the active intermediate species and directing it towards the proper substrate in the same manner as to which a cannon is loaded with reactive materials only when ready to fire, and the barrel of the cannon directs that activity towards a precise target. A precise understanding of the chemistry around the heme is central to understanding heme-catalyzed C-H bond activation. To employ explosive metaphors again – we must first understand gunpowder before we can build rockets.

## Biological C-H bond activation:

C-H bond activation is the breaking of the C-H bond as part of a substrate functionalization mechanism. Enzymes such as P450 are able to selective catalyze the functionalization of unactivated C-H bonds, meaning individual C-H bonds can be distinguished and broken with high regio- and stereoselectivity. This is notable because of the strength of the unactivated C-H bond in a saturated hydrocarbon, ~ 95-100 kcal/mol.[25] Nature regularly breaks these bonds at atmospheric pressures and ambient and physiological temperatures, in aqueous conditions, and selectively installs functional groups. Understanding this chemistry was considered a "holy grail" target by organic chemists in the mid-1990s, and although many catalysts have been discovered to functionalize aryl C-H bonds, alkyl C-H bonds are much more difficult.[26,27]

Figure 1.4 shows lauric acid, a substrate for several fatty acid hydroxylases from the cytochrome P450 family, highlighting an unactivated C-H bond in the ω-1 position. It is worth noting that all other C-H bonds are not shown, which is typical of depictions of organic molecules. As there are many C-H bonds along the molecule, and because they are so unreactive, it is standard not to show the C-H bond. Many Fatty acid hydrolase cytochrome P450s can hydroxylate this position, either selectively or along with the ω and ω-2 positions.[28–31]

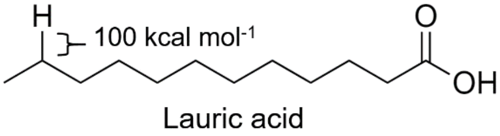

**Figure 1.4**: Lauric acid. This depiction is important because it, typical of organic chemistry depictions, does not show the C-H bonds. This is because of their commonality and unreactive nature. Highlighted is a single C-H bond that can be broken as part of the hydroxylation of ω-1 hydroxylation mechanism by cytochrome P450.

Heme enzymes are not the only systems known to use iron to cleave C-H bonds. Methane monooxygenase uses a diiron center, and αKG-dependent dioxygenases use a single nonheme iron.[32] As a C-H bond activator, cytochrome P450 has often been likened to a molecular blowtorch – this is specifically accurate because, like a blowtorch, oxygen is being burned as a tremendous amount of energy is released upon a subject.

## Understanding P450 Chemistry:

Central to understanding the chemistry of cytochrome P450s is understanding the properties of their reactive intermediates. P450s possess a proximal thiolate ligand coming from a cysteine amino acid residue. Strong electron donation from this sulfur ligand is believed to affect the Fe-O bond on the opposite side of the heme, weaking the Fe-O bond in the intermediate species in a manner that may predispose P450 towards reacting with C-H bonds.[20] Compound I is formally an Fe(V) species. In Compound I, thiolate ligation results in the extra oxidizing equivalent over the ferryl state existing delocalized over the heme macrocycle and thiolate ligand.[33] This is in contrast to histidine-ligated heme enzymes, where proximal ligation from a nitrogen atom limits the extra oxidizing equivalent in Compound I to the porphyrin ring.[34] In P450s, Compound II is a Fe(IV)-OH species, with a $pK_a \sim 12$.[35] This basic ferryl species is thought to be exclusive to heme enzymes with strong electron donors as proximal ligands, such as those that can perform C-H bond activation.

Figure 1.5 shows the general catalytic cycle for Cytochrome P450, highlighting the positions of Compounds I and II. Resting state enzyme first binds to substrate before electron delivery partners reduce the iron to the ferrous state. Dioxygen then binds before the complex is reduced again and twice protonated, resulting in the evolution of a water molecule and the generation of Compound I, the *active oxidant*. H-atom abstraction from substrate results in protonation of the oxo moiety and reduction of the formal Fe(V) center. This produces Compound II, the *rebound intermediate*. The electronically neutral radical of the substrate and the hydroxide ligand of Compound II react to form a hydroxylated product and resting state ferric enzyme. The peroxide shunt is also shown, similar to Figure 1.3 – here it directly forms Compound I while releasing a water molecule, not showing the Fe(III)-OOH$_2$ intermediate. The hydroperoxo intermediate can be additionally accessed by reacting with peroxyacids. The hydroperoxo intermediate is then protonated prior to generating Compound I and releasing a water molecule.

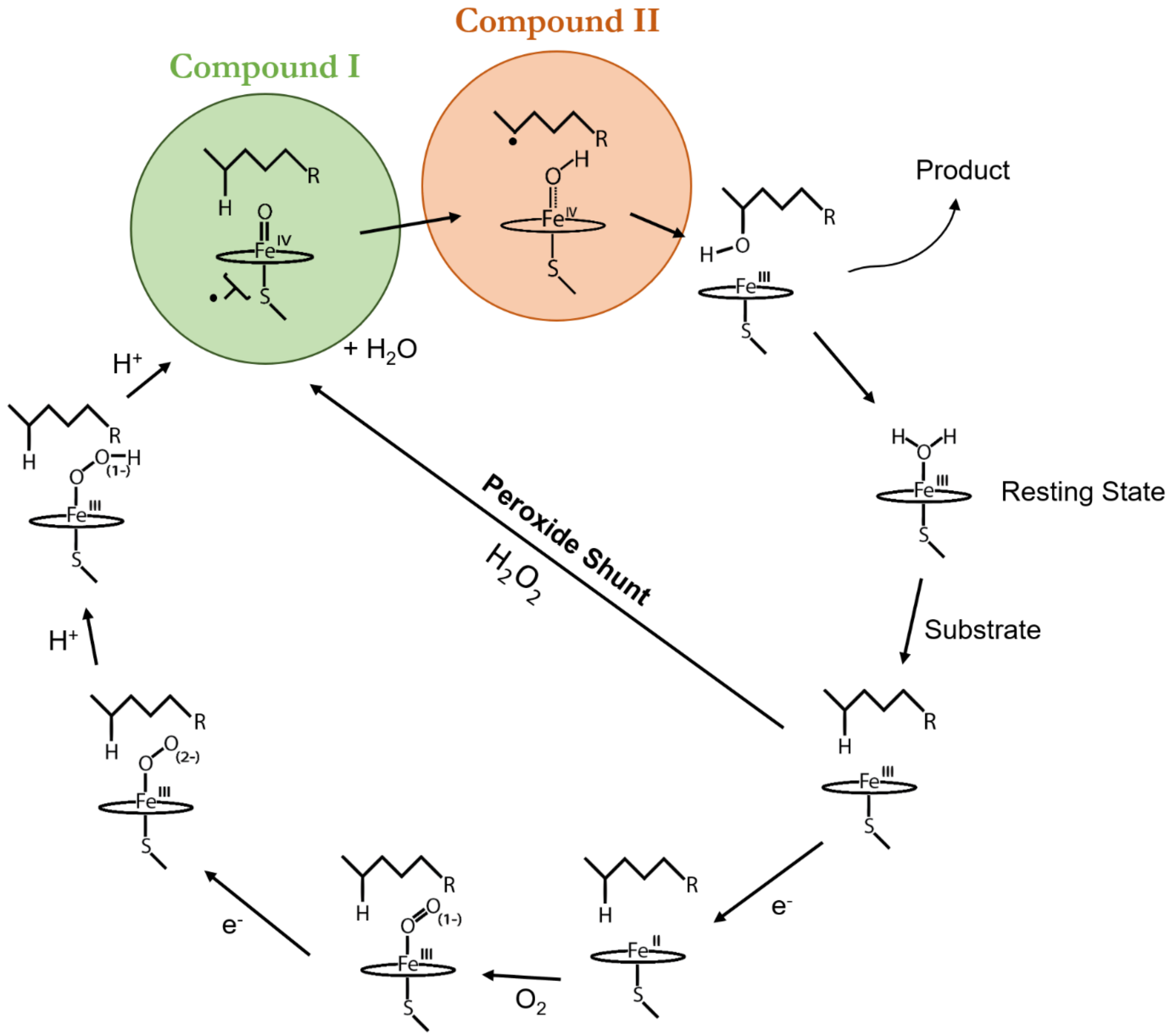

**Figure 1.5**: Catalytic cycle of Cytochrome P450. Also shown is the peroxide shunt, by which resting state enzyme reacts with hydrogen peroxide to form the intermediate prior to forming Compound I. Depicted for the distal ligand is the ligand charge.

As mentioned earlier, C-H bonds have high dissociation free energies and thus make for very difficult bonds to cleave. In hydrocarbons, dissociation energies (bond dissociation enthalpies, BDEs) range from 90 kcal mol$^{-1}$ for a terminal C-H bond in toluene to 105 kcal mol$^{-1}$ in methane.[25]

It is obvious that Compound I must be a potent oxidant. P450-I was a long-sought intermediate that eluded researchers in part because of its reactivity, with its eventual characterization in 2010 owed to a variant from *Sulfolobus acidocaldarius* that allowed P450-I to be generated in observable yields.[33] EXAFS characterization describe P450-I as an S=1 iron(IV) oxo unit, with a short Fe-O bond of 1.67 Å. Later work by Mittra et al. suggested P450-I has a two-electron reduction potential of 1.09 V (at pH 7 vs NHE).[36]

Compound II in P450 is best described as an iron(IV) hydroxide with a p$K_a$ of 11.9, and a variable Fe-O distance of 1.84 and 1.68 Å between protonated hydroxide and unprotonated oxo.[35] This is far more basic than what is observed with similar ferryl heme systems, but there is little to compare this to – the also thiolate-ligated heme enzyme chloroperoxidase (which has been shown to cleave activated C-H bonds) appears to also be basic but without signs of an observable p$K_a$; the intermediate Compound II could not be prepared above pH 7 as the enzyme converts to an unreactive form..[37–39]

Figure 1.6 shows a scheme of the competing forces in H-atom abstraction and autooxidation in cytochrome P450, which will be useful for the discussion about how Compounds I and II balance each other. The C-H bond depicted has 100 kcal mol$^{-1}$ – a free energy description of this bond-breaking process would require that the resultant O-H bond formed in Compound II would have to be stronger in order to drive the reaction forward. We can evaluate the O-H bond strength using the equation below for an aqueous proton-coupled reaction:[20,40,41]

$$D(O-H) = 23.06 * E_I^0 + 1.37 * pKa_{II} + 57.6 \pm 2\ kcal/mol \qquad (1)$$

This equation shows how the O-H bond strength in Compound II depends upon the one-electron reduction potential of Compound I, and the $pK_a$ of the ferryl moiety in Compound II.

However, it has been difficult to obtain the one-electron reduction potential for P450-I. The methods used by Mittra et al. instead calculated the two-electron potential for the reduction of Compound I through restricted open shell methods in a thiolate-ligated iron-porphine model.[36] Equation (2) allows the D(O-H) of Compound II to be evaluated as a function of the D(O-H) in ferric water-bound P450 and the two-electron reduction potential for P450-I ($E_I^{0'}$):

$$D(O-H)_{Comp-II} + D(O-H)_{ferric} = 2\big(23.06 * E_I^{0'} + 1.37 * pH + 57.6\big) \qquad (2)$$

Evaluating the above equation with the 1.09 V for the two-electron reduction potential for P450-I and the $D(O\text{-}H)_{\text{ferric}}$ of 90 kcal/mol at pH 7 reported by Mittra yields a $D(O\text{-}H)_{\text{Comp-II}}$ of 95 kcal mol$^{-1}$. This is downhill of an unactivated CH bond by ~6 kcal mol$^{-1}$.[42] Evaluating equation (1) with the $D(O\text{-}H)_{\text{Comp-II}}$ obtained through equation (2) and $pKa_{\text{Comp-II}}$ gives 0.91 ± 0.087 V for P450-I, yet Calculations by Mittra et al. suggest a proton coupled reduction potential for P450-I of 1.22 V at pH 7.

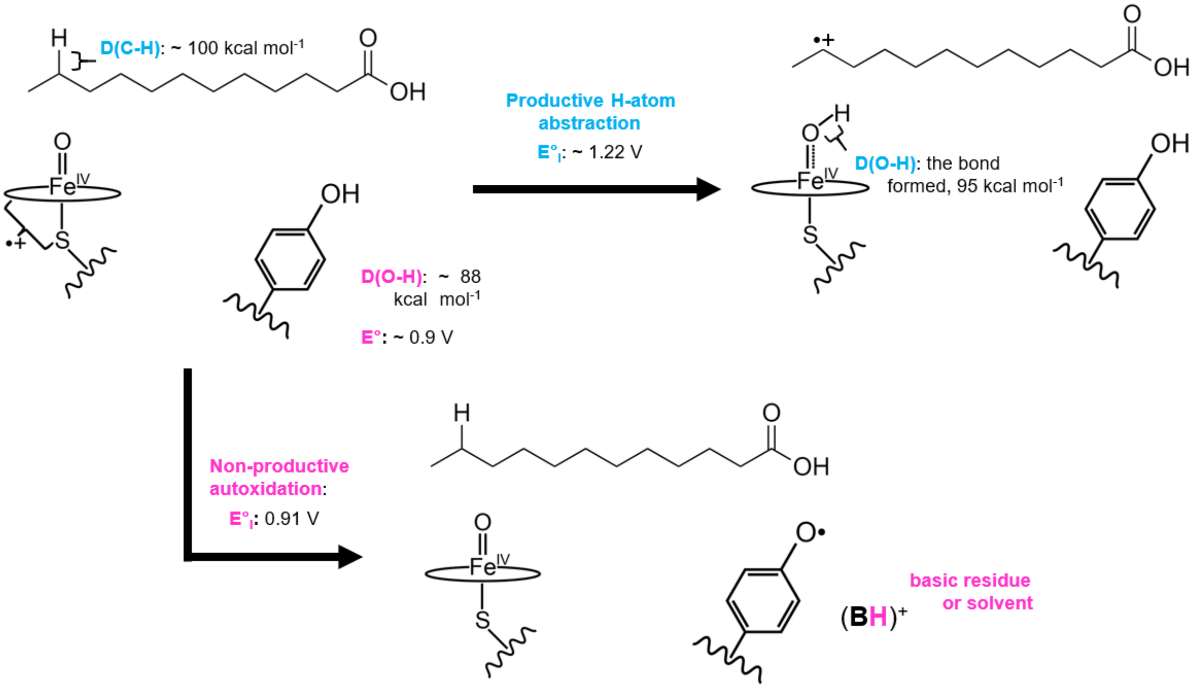

**Figure 1.6**: The protective role of the thiolate. Shown is P450-I bound to lauric acid. In the productive hydroxylation pathway (blue), the C-H bond of lauric acid (100 kcal $mol^{-1}$) is broken, driven by the proton-coupled reduction potential of P450-I, and the pKa of Compound II, or the basicity. Non-productive autoxidation is shown in pink and is driven by the one-electron reduction potential for P450-I, 0.91 V. The phenolic proton is shown here transferred to **B:**, a basic residue or solvent molecule.

Returning to Figure 1.6, we would like to highlight the text in pink showing components for an autoxidation event. The D(O-H) bond in tyrosine is, for example, significantly weaker at 88 kcal $mol^{-1}$ and has a reduction potential of ~ 0.9 V. With the high reduction potential of P450-I, it is interesting that productive H-atom abstraction occurs at all and without the oxidative power of P450-I shunting elsewhere on the enzyme’s superstructure. The one-electron reduction potential shown for P450-I for oxidation of the tyrosine residue is 0.91 V, significantly weaker than the 1.22 V for the proton-coupled one-electron reduction potential driving productive hydroxylation. Why, then, is the proton-coupled reduction potential of P450-I not driving it towards non-productive oxidation events? This has to do with the lack of available protons when Compound I is formed and substrate is bound, limiting H-atom abstraction to the productive pathway. The proton-coupled reduction potential is then pitted against one-electron reduction events to determine the fate of P450-I, but recall that there is still a 6 kcal mol$^{-1}$ barrier.

In the report detailing the pKa of P450-II, the authors discuss an analysis of the nonproductive pathway compared to productive hydroxylation, in which it is argued that the relative free energy between the two pathways varies with the pKa of Compound II and eventually changes sign. A hypothetical pKa of 3.5 would favor non-productive tyrosine oxidation by 14 kcal mol$^{-1}$, and a pKa of 12 lowers this preference for the nonproductive pathway to 3 kcal mol$^{-1}$. A Marcus theory analysis between pKas 3.5 and 12 reveals a > 10,000 fold reduction in the rate constant for non-productive oxidation events with the lifting of Compound II pKa, lowering rate constants to less than 50 s$^{-1}$ and making them non-competitive with C-H bond activation.[35]

## Section II: Peroxidases and distal ligand assignments

Peroxidases function by using the reduction of $H_2O_2$ to catalyze a range of oxidate reactions across a variety of organic substrates.[34] Peroxidases can be categorized by two superfamilies with one containing the evolutionarily related monomeric proteins found in fungi, plants, and bacteria, and the chordate peroxidase-cyclooxygenases forming the other superfamily.[43,44] Despite having a low sequence homology, proteins belonging to the first superfamily share a large degree of structural similarity, containing two antiparallel α-helices that constitute the heme binding site and a proximal histidine ligand from the C-terminal helix (of the two conserved helices).[34,45] The N-terminal helix provides catalytically relevant histidine and arginine residues, which are essential for the heterolytic cleavage of the O-O bond after binding $H_2O_2$.

The first superfamily of peroxidases is further divided into three classes.[43] Class I mostly contains intracellular and non-glycosylated heme peroxidases, excluding eukaryotic enzymes containing an endoplasmic reticulum signal sequence. Class II contains the fungal glycosylated heme enzymes containing disulfide bonds and other posttranslational modifications. Class III consists of enzymes similar to those in class II, but from plants – phylogenetic analysis of peroxidases across the superfamily indicate that class I and II/III enzymes diverged earlier from a common ancestor.[46]

Common among heme peroxidases is the scheme for Compound I formation, shown below in Figure 1.7. Ferric enzyme binds to $H_2O_2$ directly, and with the assistance of a water molecule the distal oxygen atom is protonated, promoting heterolytic cleavage of the O-O bond.[47] The distal oxygen atom leaves as a water molecule, resulting in the formation of the principal oxidant, Compound I.

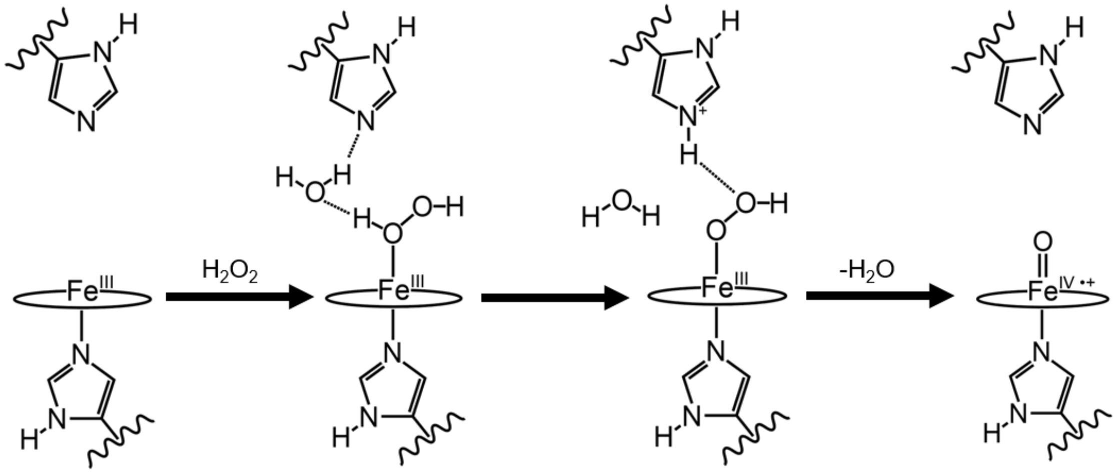

**Figure 1.7**: Peroxidase Mechanism of Compound I formation. Resting state ferric enzyme binds to $H_2O_2$, where a bridging water molecule facilities N-H bond formation and breaking one of the O-H bonds of $H_2O_2$. Water is thus the source of the electrons in the initial reduction of $H_2O_2$. The distal histidine is then deprotonated, producing water. This results in the intermediate species Compound I in peroxidases. Not shown is an active site arginine residue, which hydrogen bonds to the β-oxygen atom in the second and third steps. This electron withdrawing effect weakens the O-O bond.

For the purposes of this text and the comparison to thiolate-ligated heme enzymes, we will be focusing our discussion on class I peroxidases. These intracellular enzymes do not possess the posttranslational modifications found in the other classes. As of such, they can be expressed recombinantly in bacteria and prepared at high concentrations.

## Distal ligand assignments in peroxidase Compound II

Precise physical descriptions of the ferryl unit in Compound II in heme enzymes started to emerge in the mid-1980s. Vibrational spectroscopy had been used to characterize Compound II in the histidine-ligated systems horseradish peroxidase (a class I peroxidase) and myoglobin, which showed Fe-O stretching features at 797 and 779 $cm^{-1}$ respectively.[48,49] Assignments were done on the basis of $H_2{}^{18}O$ isotopic substation and no observed shift with $^2H_2O$. Compound II in both systems was a long-living intermediate – in horseradish peroxidase, HRP-II was prepared by rapidly mixing and freezing to prepare HRP-I first, then intentionally reducing it in the laser beam during a resonance Raman experiment to generate Compound II, which was stable on the order of minutes. Myoglobin on the other hand rapidly converts to Compound II, but after 2-3 minutes of exposure to the laser, reversion to metmyoglobin was observed. The authors were able for both studies to collect data for the unreduced ferryl intermediate Compound II, and in both cases, they were unprotonated.

In contrast to measurements on histidine-ligated systems, Compound II in chloroperoxidase (a thiolate-ligated heme enzyme despite the confusing *-peroxidase* nomenclature) was shown in 2004 to be basic.[37] The Fe-*K* X-ray absorption edge and EXAFS region indicate the oxidized chloroperoxidase species has a long Fe-O bond at 1.82 Å, which matched DFT descriptions for a protonated ferryl species, an iron(IV) hydroxide. However, with technological advances in the field of X-ray crystallography, long Fe-O bonds as indicators for protonated ferryls were not exclusive to the thiolate-ligated heme systems.

Advances in macromolecular X-ray crystallography at the turn of the century allowed for much higher resolution crystal structures of proteins. For small molecules, the ~ 0.5 Å resolution (or better) attainable allowed for bond densities themselves to be studied, while the resolution of ~ 2 Å more readily obtained with protein crystals could distinguish protein R-groups, but this was not high enough to make claims of bond orders.[50] Only with subatomic resolution $\leq$ 0.8 Å, hydrogen atom density may be observed. However, this resolution is sufficient to look for the indirect effects of protonation instead by examining a lengthening of an interatomic bond. The 1.60 Å resolution X-ray crystal structure of HRP-II from 2002 demonstrates this – the authors reported a 1.8 Å Fe-O bond, which, similar to the EXAFS measurement of CPO-II, indicated a protonated ferryl. This stood in direct opposition to the prior resonance Raman measurements of HRP-II. The next decade produced a series of publications that eventually established what was behind this disagreement, ultimately concluding that researchers were observing photoreduced species on the beamline and that the long Fe-O bonds were not of the ferryl species. This is discussed further in Chapter III.

With the photoreduction problem now understood, it was re-established that a protonated Compound II intermediate would require a donating proximal ligand. Figure 1.8 shows a comparison between Compound II in cytochrome P450 and horseradish peroxidase using only spectroscopic data.[35,48] P450-II is a basic species with a long Fe-O bond of 1.84 Å, while HRP-II appears to be an unprotonated iron(IV) oxo species invariant down to pH 5. With no sign of $^2$H isotopic shifts, an unprotonated description is consistent. Additionally, analysis using Badger's rule, an empirical rule linking bond distances to their stretching frequencies, indicates a Fe-O bond distance of 1.66 Å. The use of Badger's rule to evaluate vibrational spectra is discussed in Chapter IV. Reports of long Fe-O bonds in histidine ligated systems had been refuted, and it became clear that a histidine ligand could not support a basic ferryl.

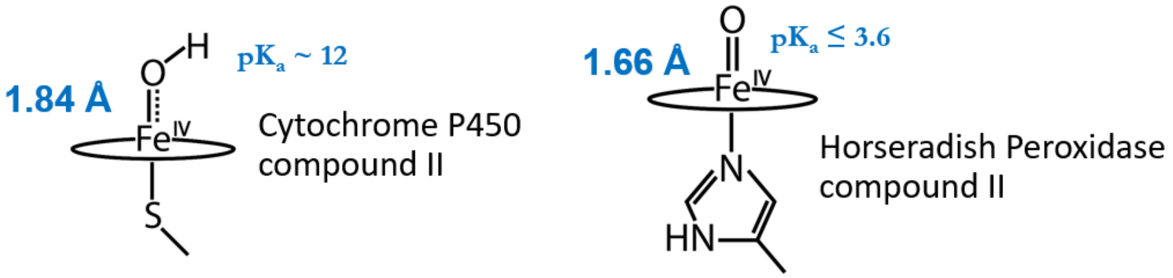

**Figure 1.8**: Comparison of Compound II between thiolate and histidine proximal ligands. Shown are the bond distances from spectroscopic measurements alone.

Characterization of catalase from *Helicobacter pylori*, a tyrosine-ligated heme enzyme, pointed to a $pK_a$ of 13.1 in Compound II.[51] Similar to how the elevated $pK_a$ in P450-II allows for a diminished P450-I reduction potential, a diminished potential in catalase from an even *more* basic Compound II would increase selectivity for peroxide disproportionation over one-electron reactions, like oxidation of the protein superstructure. Peroxidases function through two successive one electron reactions.[34] Given this, a radically different Compound II species for peroxidases is expected when compared to heme oxygenases.

## Section III: The Direct Visualization of an Fe(IV)-OH Intermediate in a peroxidase:

In a 2016 *Nature Communications* article, Kwon et al. report the direct visualization of an iron(IV) hydroxide in ascorbate peroxidase Compound II (APX-II).[52] Ascorbate peroxidase is a class I heme peroxidase, prototypical of its class with a proximal histidine ligand and relatively small size at 27 kDa. What makes this report so compelling is that the authors used neutron crystallography, a method that uses diffracted neutrons to produce a density map of atomic nuclei. Unlike X-ray crystallography which is usually limited in its ability to observe H-atoms (without extremely high resolution data), neutron crystallography can observe the density for exchanged deuterons in a crystal. Additionally, neutrons are intrinsically non-ionizing, thus removing the experimental problem of photoreduction on the beamline. Kwon et al. observe a density in the distal position of the heme iron which they model as an -OH ligand, positioned 1.88 Å away from the heme iron.

Figure 1.9 shows a re-processing of the publicly available diffraction data from the neutron crystallography experiment, PDB: 5JPR, and the X-ray crystallography experiment, 5JQR (see next paragraph for details on joint refinement). The neutron and X-ray diffraction structure factors were download, along with the PDB model itself for 5JPR. The distal ligand was removed from the PDB structure file. We then co-refined the model with the neutron and X-ray density maps, producing the structure shown below in WinCoot. This exercise was to reproduce the methods used for ligand assignment in the 2016 report. In order to be unbiased, the model is refined first without any ligand present in the distal position. The ligand is then modeled in based on the Fo-Fc map – in this case, the *neutron* Fo-Fc map alone, as just that map would contain density from a proton (deuteron). Accordingly, the X-ray Fo-Fc map shows just a spherical density for an oxygen atom. In our attempts to reprocess the data, the neutron Fo-Fc maps consistently show a density that fits an -OH ligand approximately 1.9 Å away. Even in co-refinements using X-ray data from known reduced (long Fe-O bonds) APX species, the neutron Fo-Fc map points to a hydroxide ligand.

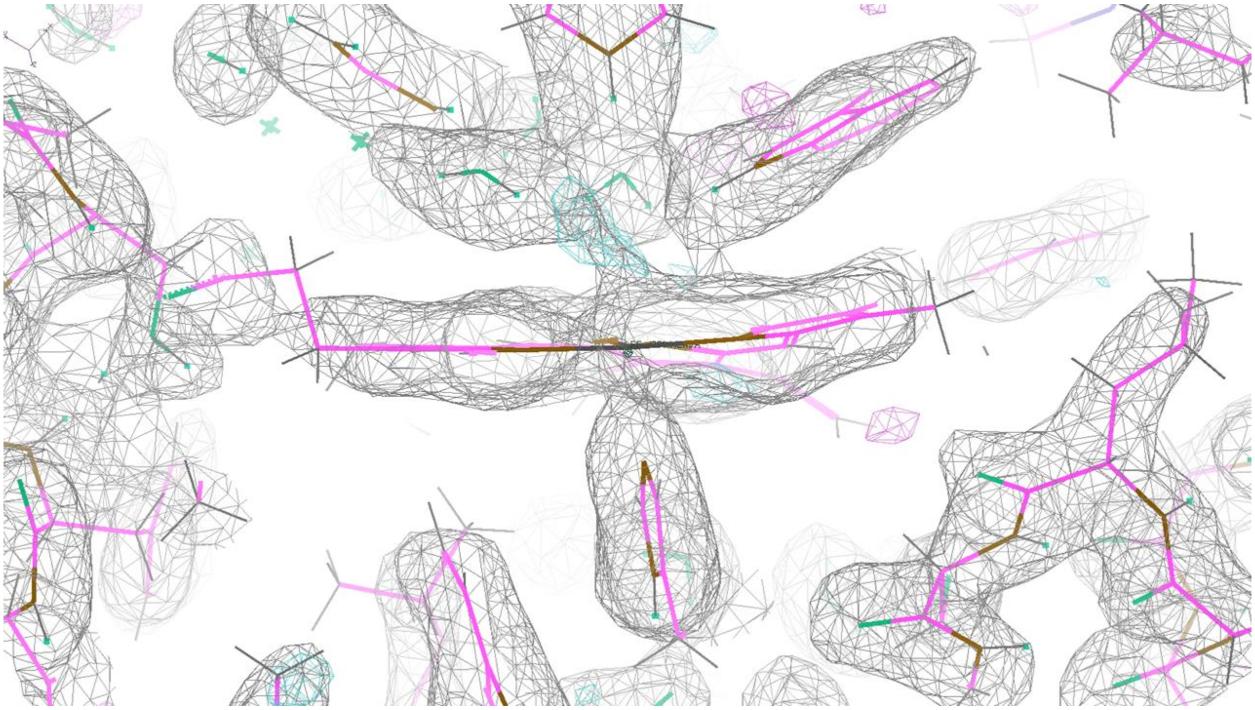

**Figure 1.9**: Co-refinement of X-ray and neutron diffraction data from Kwon et al. Refinement was performed by the author of this manuscript to produce this figure as part of a re-analysis of published data. Not included in this structural model is a distal ligand – this is to produce the Fo-Fc *neutron* difference map density here drawn in cyan. This oblong shape is approximately 2 Å away from the central Fe atom modeled position and possesses enough size to reasonably hold a -OH ligand. We believe an -OH ligand to be an accurate depiction of the neutron data.

It is important to understand the specific points of using both X-ray and neutron crystallographic data for the discussions that follow in this text. First, neutron crystals are soaked or grown in $D_2O$ in order to exchange many of the protein's protons with deuterons. This serves the dual purpose of being a larger target (twice as much signal!) and solving a complication with methylene scattering – the negative scattering length of a H-atom is about half the positive value for carbon, such that a -$CH_2$- bridging group would be observed as a break in the density.[53] This can be observed in Figure 1.9 on the left side of the heme ring, where the methylene bridge to the propionate groups show a break in the density map. To overcome these breaks in the density, a companion set of X-ray data are often used to co-refine the model. A neutron diffraction experiment also takes days to collect and requires a millimeter-scale crystal, and even then, the resolution of this structure is significantly lower than the X-ray data. In the 2016 report discussed, the neutron data are at a resolution of 2.2 Å. This is an important distinction, because the final assignment of the -OH ligand placed the oxygen atom 1.88 Å away. This precise bond distance comes from the X-ray data, not the neutron data.

How, then, are the authors sure the X-ray data do not reflect a photoreduced species instead, artificially lengthening the Fe-O bond? In Chapter III, we discuss the multi-crystal X-ray crystallography technique, in which researchers limit the X-ray dose on an entire structure by limiting the dose upon a set of many single crystals, combining data to achieve a pristine structure. The authors of the 2016 article used these techniques and compared their results to a previous study where they first applied the method on two histidine-ligated peroxidases.[54] For one ferryl intermediate, they successfully used the multi-crystal method to produce a structure with a short Fe-O bond. The other intermediate, APX-II, showed a long Fe-O bond of 1.86 Å.

But, even if the X-ray crystal structure is reduced, what can be made of the neutron structure? The confirming experiments that APX-II was made in the 2016 report was microspectrophotometry, where the Q-bands in the UV/Visible absorption spectrum are observed showing markers for APX-II, and crystal K-edge X-ray absorption spectroscopy, in which a shift in the K-edge is observed when compared to ferric crystals, consistent with a raise in oxidation state. Crystals of APX-II were prepared by soaking ferric crystals in 0.2 mM oxidant (*m*-chloroperbenzoic acid) for ~ 40 seconds. It is worth noting that the large neutron crystal (0.7 x 0.5 x 0.4 $mm^3$) was not *specifically* examined by a control experiment, as reported in the article. XAS on APX-II crystals and crystal UV/Visible spectroscopy appear to only be demonstrations of the method, rather than confirming experiments. Chapter III of this text further scrutinizes the control experiments, in effort to understand the source of our disagreement.

### Can a proximal histidine ligand support a basic Compound II species?

The authors of the 2016 reported direct visualization of an iron(IV) hydroxide in a peroxidase prepared their samples at pH 8.5. If their findings are indeed true, this would mean APX-II is unusually basic, and the link discussed earlier between a basic ferryls and biological C-H bond activation may need revisiting. APX has not been shown to perform two-electron chemistry, but functions as a typical class I peroxidase.

In chapter II, we will show that we have isolated the same enzyme, APX from soybean, recombinantly expressed in *E. coli.* using a barrage of spectroscopic techniques, we probe the distal ligand for signs of protonation.

Chapter III contains an analysis of the establishing experiments from the 2011 paper, *Nature of the Ferryl Heme in Compounds I and II*, and the 2016 paper, *Direct visualization of a*

*Fe(IV)-OH intermediate in a heme enzyme*, along with an endeavor to isolate the Fe(III)-OH form of APX.

Finally, chapter IV introduces a new technique, nuclear resonance vibrational spectroscopy (NRVS), which allows us to directly visualize the Fe-O bond. We apply this to APX-II, to verify our previous work.

## Section IV: Introduction to methods utilized in this text:

### UV/Visible electronic absorption spectroscopy:

The discovery of *cytochrome P450* is credited to a 1958 publication by Klingenberg, who showed that liver microsomes from rats could bind to CO to produce a pigment. [55] In 1964, Omura and Sato demonstrated that the origin of this pigment was a heme enzyme, naming it cytochrome P450 after the absorption maximum of 450 nm in the CO-bound state.[56] UV/Visible absorption spectroscopy has since been the backbone of heme enzyme research.

Figure 1.10 shows a representative UV/Vis spectrum of a heme enzyme. The Soret band is the intense absorption feature in the blue region of the visible spectrum, arising from a $\pi - \pi^*$ electronic transition, from the π-conjugated porphyrin ring. The Soret band is named after the its discoverer, Jacques-Louis Soret, who observed light transmitted through a 1:1000 dilution of blood in his 1883 report.[57] The α Q-band originates from a the weakly-allowed electronic transition to the $S_1$ state (the Soret being the strong transition from $S_0$ to $S_2$), and the β Q-band comes from transitions to higher vibrational levels in the $S_1$ state.

The $R_z$, or Reinheitszahl value, is the ratio of absorbance due to heme-absorbing features (the Soret) to absorbance due to protein ($A_{280}$). This ratio is a measure of purity and is a good indicator for the grade of enzyme – spectroscopy grade requires very high purities, although the $R_z$ of that can range depending on the system (1.8 – 2.2).

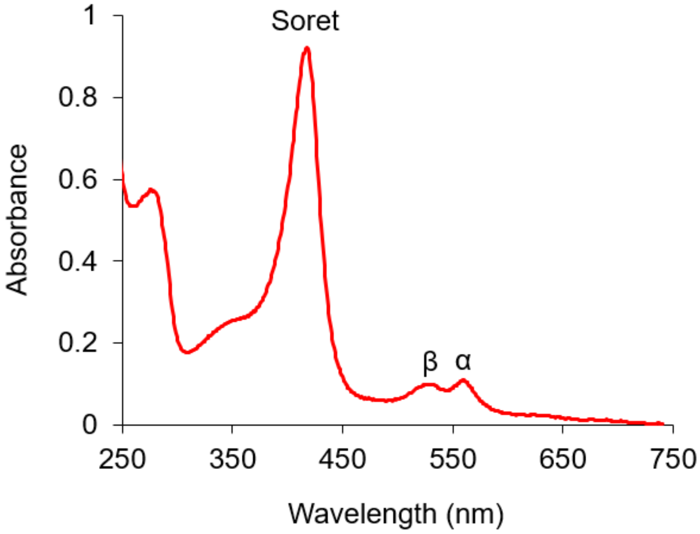

**Figure 1.10**: Ultraviolet/Visible absorption spectrum of heme enzymes. Depicted are the Soret bands, and β- and α-Q bands.

<u>Stopped-Flow UV/Visible spectroscopy:</u>

As an extension of UV/Visible spectroscopy, stopped-flow techniques here use a syringe-driven, rapid mixing setup. Effectively, this allows for reproducible mixing and aging, then collecting on the scale of milliseconds entire UV/Visible absorption spectra. The simplest application in this text is the 1:1 mixing of 20 µM APX with oxidant to fill the cuvette with 10 µM APX and immediately begin collecting spectra. In a simple pH-jump experiment, ferric APX at 20 µM in a weak buffer is mixed 1:1 with a strong, high pH-buffer, and spectra are collected before the protein becomes irreversibly damaged and the spectra rapidly bleach. In more elaborate mixes, such as mixing 1:1 to produce an intermediate and then mixing that solution 1:1 to rapidly change the pH, we note that it is critical that all syringes in the flow setup be displaced such that there is no backflow.

### Freeze-quench:

The freeze-quench apparatus is a single ram that drives 1 – 4 syringes over a distance that is programmed into a controller. Using different ratios of syringe barrels, aging lines, and mixer setups, quite a diverse range of reactions can be performed with the apparatus. The reacted sample sprays from the last mixer – this is routinely sprayed into liquid ethane which rapidly freezes the sample in a manner that minimize ice crystal formation.

We note that with the freeze-quench apparatus, key to it working reliably is following proper cleaning procedure of the sample tubing and especially the mixer. Sonicating will help clean debris, and if that does not restore flow, the mixers can be disassembled manually and cleaned. The mixers are checked before and after the quench.

### Hand-mixing-quench:

For reactions with a time scale of tens of seconds, the freeze-quench apparatus is not ideal. An aging line would have to be filled, and then that would need to be filled again in a second push from the ram to eject the aged sample, wasting the sample's cost in protein at least once over. In these cases, we pursued hand-mixing strategies. Enzyme was pipetted up at high concentrations

(~3 mM) and mixed in a tube containing a concentrated amount of oxidant. In a timed 30 second period, the sample was mixed up and down via pipetting, until it was shot into liquid ethane. Because of the limited mixing volume of the pipette (1 ml), multiple hand-quenches were mixed together and ground up into a powder to constitute one batch preparation of intermediate.

## Mössbauer Spectroscopy:

The Mössbauer effect is the recoilless emission of γ-photons in solid substrates corresponding to nuclear resonances, where most of the recoil energy is converted to lattice vibration energy but a recoil-free fraction remained in solid samples. Mössbauer spectroscopy provides a rich tool for examining iron, as it is very sensitive to changes in the structural and electronic environment around the iron atom. Samples must be enriched with $^{57}$Fe in order to be observed, as $^{57}$Fe has a nuclear spin of $I_g$ = ½, whereas the most common isotope of iron, $^{56}$Fe, is $I_g$ = 0. Without a magnetic nuclear ground and excited state, a resonant nuclear absorption event does not take place and there is no change in the signal from the γ-photon.

Figure 1.11 shows an overview of a Mössbauer spectroscopy experiment. Shown is spectrum for a single S = 1, Fe(IV) species in a heme enzyme. In this system, there are two nuclear excited states. These absorption energies are accessed by modulating the γ-photon energy. The $^{57}$Co source atoms become $^{57}$Fe via β decay, resulting in an excited $^{57}$Fe nuclear state which relaxes to the ground state, emitting a 14.4 keV γ-photon. By situating the source on a motor, the Doppler effect allows the photon's energy to be modulated on the scale of neV. The spectrum shown in Figure 1.14 is in units mm/s, but this could just as well be in relative neV from the Mössbauer resonance of 14.4 keV. The spectrum shows two dips in the signal corresponding to the absorption events at those particular energies, and less of the incident photon traveling through the sample and into the detector.

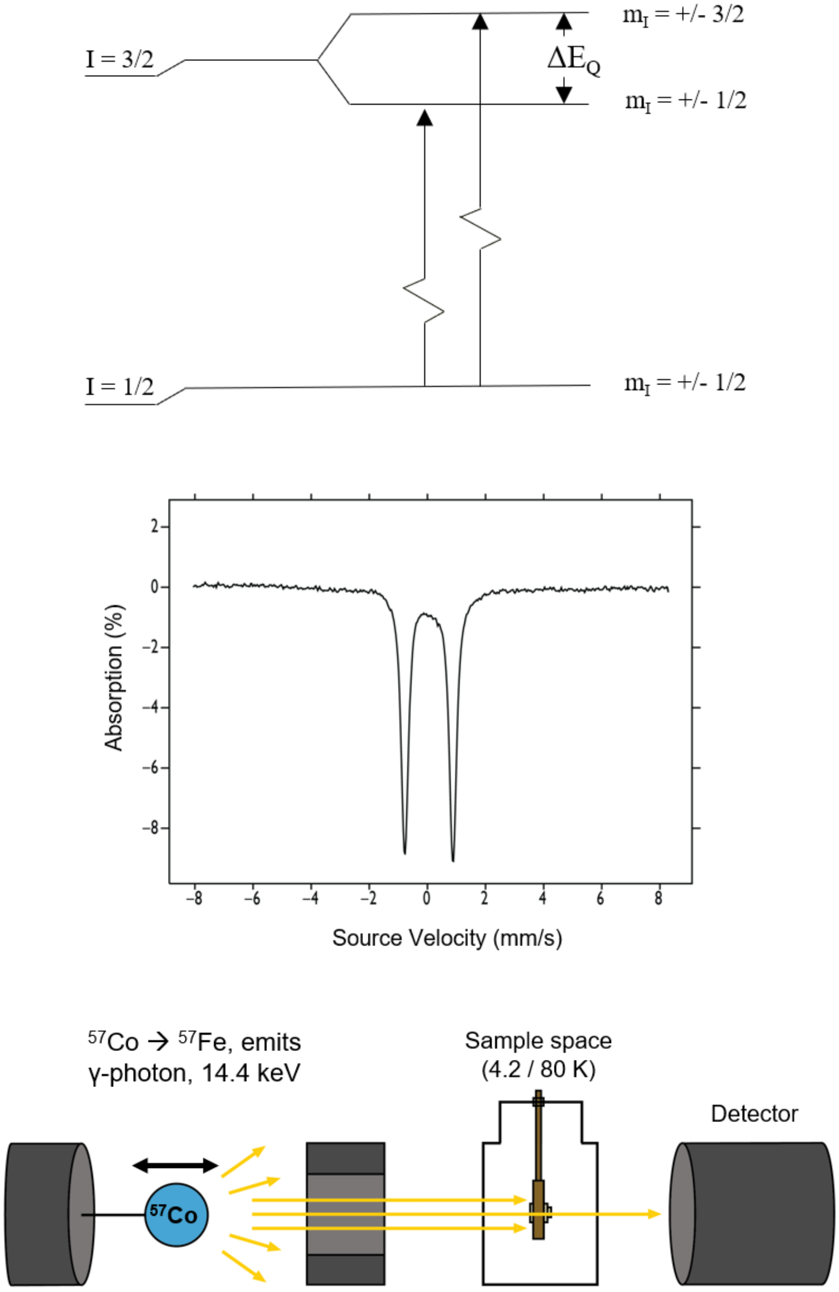

**Figure 1.11**: Overview of Mössbauer Spectroscopy: (Top): Quadrupole splitting of a $^{57}$Fe nuclear excited state in a S = 1 system. (Middle): Representative Mössbauer spectrum showing the nuclear absorption events. (Bottom): The experimental setup – a $^{57}$Co source on a motor is the origin of the monochromatic 14.4 keV photon beam, which is energy-shifted by the motor to access the nuclear resonance energies of the $^{57}$Fe sample. Photons pass through the sample and hit a detector – signal drops when a photon instead is absorbed by the sample.

Mössbauer spectra are sensitive to the electric field around the nucleus. Magnetic spectra (S = non-integer) show instead six features for nuclear energy state transitions. The quadrupole splitting, $\Delta E_Q$, is the electronic interaction of the different $m_I$ levels. The different shaped nuclei in the excited state have differences in their electrostatic interactions with the electric field gradient (EFG) tensor. Increased asymmetry in the EFG tensor will increase $\Delta E_{Q.}$ The isomer shift, δ, is a measure of s-electron density around the nucleus. As it is influenced by oxidation state, spin state, and structural factors, it is not directly a probe for oxidation state – but it can be established in a particular system how δ responds – for example in heme enzymes, Fe(IV) displays δ = ~ 0 mm/s, Fe(III) shows δ = ~ 0.6 mm/s, and Fe(II) δ = 0.8 – 1.2 mm/s.

X-ray absorption spectroscopy:

The X-ray absorption spectrum of a sample exhibits a sharp rise in the absorption coefficient, called an edge, that corresponds to a 1s electron being ejected from the absorbing atom (for K-edge XAS). Figure 1.12 shows the major features of an X-ray absorption spectrum, highlighting the pre-edge, edge, and EXAFS regions. The edge is dependent upon the ionization potential of a bound electron, which increases in energy as the oxidation state of the atom is raised. The EXAFS refer to both the region of the spectrum (modulations in the X-ray absorption coefficient), and the techniques applied to study structure from such data. EXAFS yields structural information with 4-5 Å of the absorbing atom, giving radial distance information about what type of atom, how many, and at what distance. Fitting these data result in structural information with hundredths of an Ångstrom resolution on individual bond distances.

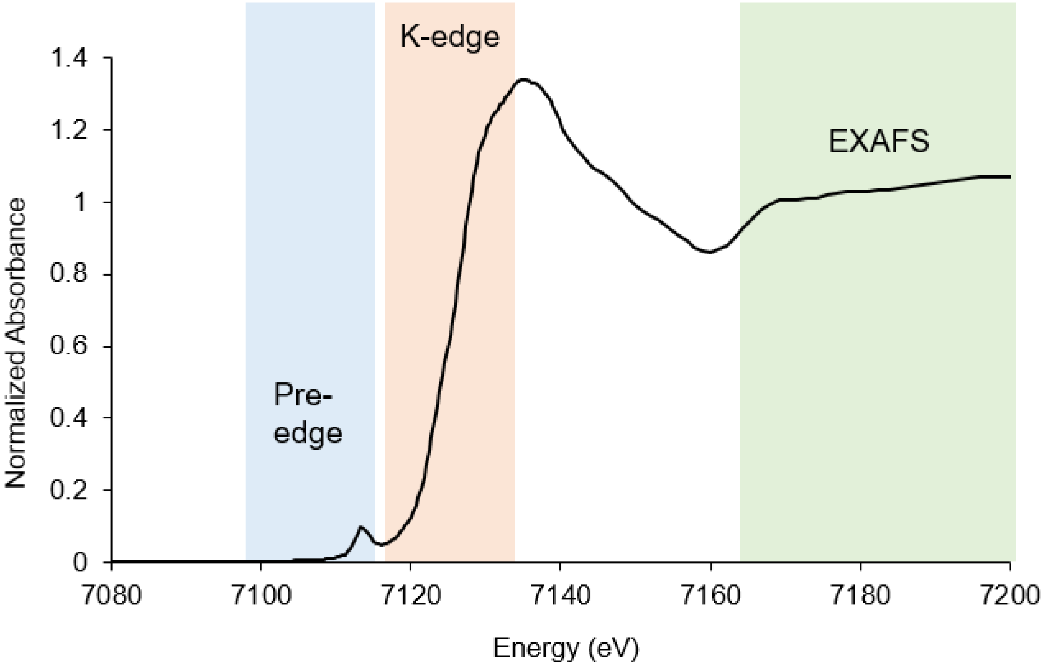

**Figure 1.12**: An X-ray absorption spectrum for a heme enzyme. The major regions of the spectrum are highlighted.

Figure 1.13 shows the porphyrin scattering paths considered when fitting EXAFS data for heme enzymes. In addition to the primary coordination sphere of ligating nitrogen atoms from the porphyrin ring, the proximal and distal ligands must be included. Because of the rigid and symmetrical geometry of the porphyrin ring, scattering paths comprised of 1) Fe → $C_\alpha$, 2) Fe → N → $C_\alpha$, and 3) Fe → $C_{meso}$ trajectories allow for a more accurate description of the photoelectron's path. It is problematic to include more variables in fitting, as this can lead to inaccurate descriptions of the data, but with the known geometry of the porphyrin ring and the number of contributions each trajectory would have relative to each other, the porphyrin contribution is restricted, and each variable is not adjusted independently.

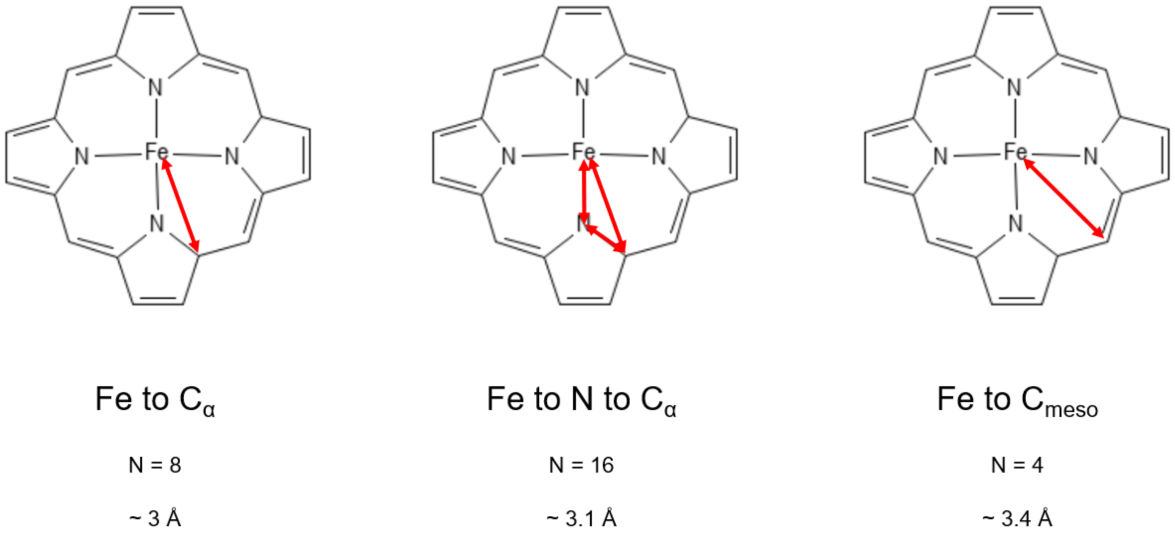

Fe to $C_\alpha$

N = 8

~ 3 Å

Fe to N to $C_\alpha$

N = 16

~ 3.1 Å

Fe to $C_{meso}$

N = 4

~ 3.4 Å

**Figure 1.13**: Porphyrin scattering paths used for fitting EXAFS data for heme enzymes. Not depicted are the direct scattering paths to the 4 axial nitrogen ligands are also included in fitting EXAFS data, along with the distal ligand (oxygen) and proximal ligand (nitrogen) scattering paths.

### Nuclear Resonance Vibrational Spectroscopy

Chapter 4 explores this technique in detail. Briefly, vibrational levels of a molecule are coupled to a nuclear resonance. By coupling to the nuclear resonance, only vibrations involving the probe nucleus are observed. In heme enzymes, this means $^{57}$Fe-enriched samples can be probed for their iron-only vibrational spectrum. As with Mössbauer spectroscopy, excitation is with a 14.4 keV photon, however meV range energies are surveyed to observe phonon generation.

### Handling *m*-CPBA:

Meta-chloroperbenzoic acid is not stable at purities > 77%, and less so in aqueous solution. For these reasons, we periodically prepare fresh *m*-CPBA at 99% purity every 3-6 months from the 4 °C-stable 77% concentration by washing approximately 5 grams of 77% pure *m*-CPBA with 1 L of cold water, 1 L of cold 100 mM potassium phosphate buffer at pH 7.5, then another 1 L of water. This was to remove the water-soluble components, and purity is assessed after washing by NMR. Dried *m*-CPBA was stored at -20 °C.

For reactions in which a dilute amount of *m*-CPBA is required, 100 mg of the purified *m*-CPBA was dissolved into 5 ml acetonitrile to create a stock solution in which all *m*-CPBA dissolves. Dilutions were then made from this stock solution to ensure accurate concentrations. For reactions that required much higher concentrations of *m*-CPBA, it was necessary to prepare solutions of 30% acetonitrile and 70% $H_2O$ in order to keep all the oxidant soluble. Cloudiness in the solution indicates *m*-CPBA is precipitating from solution, which can interfere with the mixers of the freeze-quench apparatus.

### Spin states of relevant heme systems:

Shown below in Figure 1.14 are the spin states for the relevant forms of APX in this text. Resting state ferric APX has 5 electrons populating the d-orbitals of the heme iron and exists as a 5-coordinate, high-spin species. Chapter II focuses on the ferryl intermediate APX-II. APX-II is an integer spin system and is thus EPR silent and presents as a quadrupole doublet by Mössbauer spectroscopy. Chapter III focuses on the low-spin ferric form of APX, a $S = 1/2$ system.

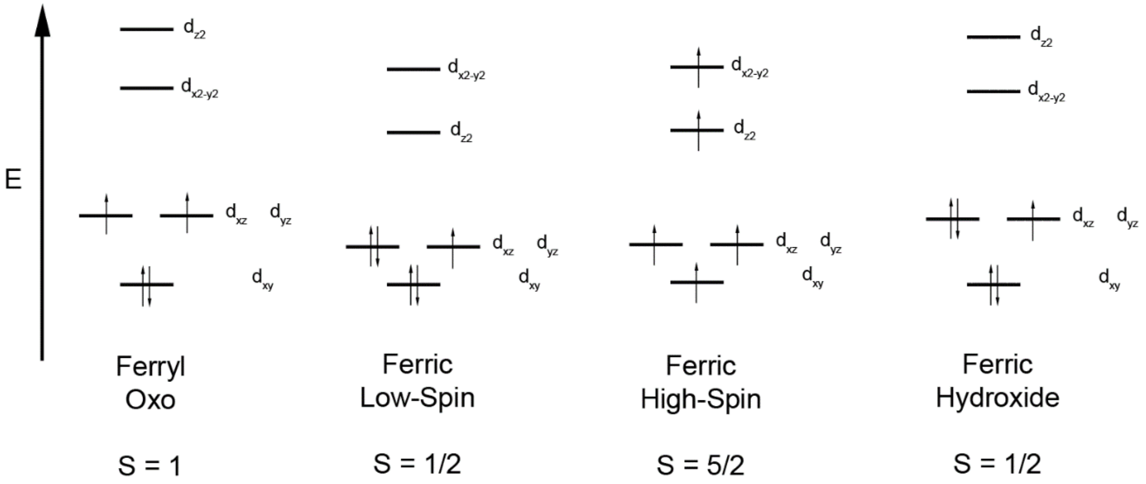

**Figure 1.14**: Spin state diagrams for the ferryl, ferric low-spin, ferric high-spin, and ferric hydroxide forms of APX.

Visualization and Modeling Software:

Molecular graphics for this text were prepared using UCSF ChimeraX.[58] Preparing the computational models for simulating spectra was done in GaussView6.[59] Preparation of PDB files was done in PyMol.[60] Generally, extraneous elements were removed from the PDB file in PyMol, prior to producing the graphic in UCSF ChimeraX. PDB structures pruned down to the relevant atoms in PyMol served as the starting point for DFT calculations. WinCoot was for visualizing neutron and electron density maps, and visualizing the co-refinement process of structural data.[61] The co-refinement process was performed using the *Phenix* software package.[62]

**References:**

1. Ducluzeau, A.-L. & Nitschke, W. When Did Hemes Enter the Scene of Life? On the Natural History of Heme Cofactors and Heme-Containing Enzymes. in *Cytochrome Complexes: Evolution, Structures, Energy Transduction, and Signaling.* 13–24 (Springer, Dordrecht, 2016).

2. Kim, H. J., Khalimonchuk, O., Smith, P. M. & Winge, D. R. Structure, function, and assembly of heme centers in mitochondrial respiratory complexes. *Biochimica et Biophysica Acta - Molecular Cell Research* **1823**, 1604–1616 (2012).

3. Kranz, R. G., Richard-Fogal, C., Taylor, J.-S. & Frawley, E. R. Cytochrome c Biogenesis: Mechanisms for Covalent Modifications and Trafficking of Heme and for Heme-Iron Redox Control. *Microbiol. Mol. Biol. Rev.* **73**, 510–528 (2009).

4. Tezcan, F. A., Winkler, J. R. & Gray, H. B. Effects of ligation and folding on reduction potentials of heme proteins. *J. Am. Chem. Soc.* **120**, 13383–13388 (1998).

5. Bhagi-Damodaran, A., Petrik, I. D., Marshall, N. M., Robinson, H. & Lu, Y. Systematic tuning of heme redox potentials and its effects on O2 reduction rates in a designed oxidase in myoglobin. *J. Am. Chem. Soc.* **136**, 11882–11885 (2014).

6. Bowman, S. E. J. & Bren, K. L. The chemistry and biochemistry of heme c: Functional bases for covalent attachment. *Natural Product Reports* **25**, 1118–1130 (2008).

7. Barker, P. D. & Ferguson, S. J. Still a puzzle: Why is haem covalently attached in c-type cytochromes? *Structure* **7**, R281–R290 (1999).

8. Stevens, J. M., Daltrop, O., Allen, J. W. A. & Ferguson, S. J. C-type cytochrome

formation: Chemical and biological enigmas. *Acc. Chem. Res.* **37**, 999–1007 (2004).

9. Guengerich, F. P. Mechanisms of Cytochrome P450-Catalyzed Oxidations. *ACS Catalysis* **8**, 10964–10976 (2018).

10. Ahmed, M. H., Ghatge, M. S. & Safo, M. K. Hemoglobin: Structure, Function and Allostery. in *Subcellular Biochemistry* **94**, 345–382 (Springer, 2020).

11. Bringas, M., Petruk, A. A., Estrin, D. A., Capece, L. & Martí, M. A. Tertiary and quaternary structural basis of oxygen affinity in human hemoglobin as revealed by multiscale simulations. *Sci. Rep.* **7**, 1–10 (2017).

12. Hub, J. S., Kubitzki, M. B. & de Groot, B. L. Spontaneous quaternary and tertiary T-R transitions of human hemoglobin in molecular dynamics simulation. *PLoS Comput. Biol.* **6**, 1–11 (2010).

13. Krainer, F. W. & Glieder, A. An updated view on horseradish peroxidases: recombinant production and biotechnological applications. *Applied Microbiology and Biotechnology* **99**, 1611–1625 (2015).

14. Henriksen, A., Smith, A. T. & Gajhede, M. The structures of the horseradish peroxidase C-ferulic acid complex and the ternary complex with cyanide suggest how peroxidases oxidize small phenolic substrates. *J. Biol. Chem.* **274**, 35005–35011 (1999).

15. Henriksen, A. *et al.* Structural interactions between horseradish peroxidase C and the substrate benzhydroxamic acid determined by X-ray crystallography. *Biochemistry* **37**, 8054–8060 (1998).

16. Conyers, S. M. & Kidwell, D. A. Chromogenic substrates for horseradish peroxidase.

*Anal. Biochem.* **192**, 207–211 (1991).

17. Finkelstein, I. J., Ishikawa, H., Kim, S., Massari, A. M. & Fayer, M. D. Substrate binding and protein conformational dynamics measured by 2D-IR vibrational echo spectroscopy. *Proc. Natl. Acad. Sci. U. S. A.* **104**, 2637–2642 (2007).

18. Urban, P., Lautier, T., Pompon, D. & Truan, G. Ligand access channels in cytochrome P450 enzymes: A review. *International Journal of Molecular Sciences* **19**, (2018).

19. Shakunthala, N. New cytochrome P450 mechanisms: Implications for understanding molecular basis for drug toxicity at the level of the cytochrome. *Expert Opinion on Drug Metabolism and Toxicology* **6**, 1–15 (2010).

20. Yosca, T. H., Ledray, A. P., Ngo, J. & Green, M. T. A new look at the role of thiolate ligation in cytochrome P450. *J. Biol. Inorg. Chem.* **22**, 209–220 (2017).

21. Reece, S. Y., Hodgkiss, J. M., Stubbe, J. A. & Nocera, D. G. Proton-coupled electron transfer: The mechanistic underpinning for radical transport and catalysis in biology. in *Philosophical Transactions of the Royal Society B: Biological Sciences* **361**, 1351–1364 (Royal Society, 2006).

22. Mittler, R. & Zilinskas, B. A. Purification and characterization of pea cytosolic ascorbate peroxidase. *Plant Physiol.* **97**, 962–8 (1991).

23. Makris, T. M., Denisov, I., Schlichting, I. & Sligar, S. G. Activation of molecular oxygen by cytochrome P450. in *Cytochrome P450: Structure, Mechanism, and Biochemistry: Third edition* 149–182 (Springer US, 2005).

24. Poulos, T. L. Structural biology of heme monooxygenases. *Biochemical and Biophysical*

*Research Communications* **338**, 337–345 (2005).

25. Blanksby, S. J. & Ellison, G. B. Bond dissociation energies of organic molecules. *Acc. Chem. Res.* **36**, 255–263 (2003).

26. Arndtsen, B. A., Bergman, R. G., Mobley, T. A. & Peterson, T. H. Selective Intermolecular Carbon-Hydrogen Bond Activation by Synthetic Metal Complexes in Homogeneous Solution. *Acc. Chem. Res.* **28**, 154–162 (1995).

27. Hartwig, J. F. Catalyst-controlled site-selective bond activation. *Accounts of Chemical Research* **50**, 549–555 (2017).

28. Kim, D., Cha, G. S., Nagy, L. D., Yun, C. H. & Guengerich, F. P. Kinetic analysis of lauric acid hydroxylation by human cytochrome P450 4A11. *Biochemistry* **53**, 6161–6172 (2014).

29. Lim, Y. R. *et al.* Regioselective oxidation of lauric acid by CYP119, an orphan cytochrome P450 from sulfolobus acidocaldarius. *J. Microbiol. Biotechnol.* **20**, 574–578 (2010).

30. Different Mechanisms of Regioselection of Fatty Acid Hydroxylation by Laurate (ω-1) - Hydroxylating P450s, P450 2C2 and P450 2E1. *J. Biochem.* **115**, 338-344 (1994).

31. Benveniste, I., Salaün, J.-P., Simon, A., Reichhart, D. & Durst, F. Cytochrome P-450-Dependent ω-Hydroxylation of Lauric Acid by Microsomes from Pea Seedlings. *Plant Physiol.* **70**, 122–126 (1982).

32. Krebs, C., Fujimori, D. G., Walsh, C. T. & Bollinger, J. M. Non-heme Fe(IV)-oxo intermediates. in *Accounts of Chemical Research* **40**, 484–492 (American Chemical

Society, 2007).

33. Rittle, J. & Green, M. T. Cytochrome P450 Compound I: Capture, Characterization, and C-H bond Activation Kinetics. *Science.* **330**, 933–937 (2010).

34. Dunford, H. B. & Dunford, H. B. *Peroxidases and catalases : biochemistry, biophysics, biotechnology, and physiology*. (John Wiley & Sons, 2010).

35. Yosca, T. H. *et al.* Iron(IV)hydroxide pKa and the Role of Thiolate Ligation in C-H Bond Activation by Cytochrome P450. *Science*. **342**, 825-829 (2013).

36. Mittra, K. & Green, M. T. Reduction Potentials of P450 Compounds I and II: Insight into the Thermodynamics of C-H Bond Activation. *J. Am. Chem. Soc.* **141**, 5504–5510 (2019).

37. Green, M. T., Dawson, J. H. & Gray, H. B. Oxoiron(IV) in Chloroperoxidase Compound II Is Basic: Implications for P450 Chemistry. *Science.* **304**, 1653–1656 (2004).

38. Zaks, A. & Dodds, D. R. Chloroperoxidase-Catalyzed Asymmetric Oxidations: Substrate Specificity and Mechanistic Study. *J. Am. Chem. Soc.* **117**, 10419–10424 (1995).

39. Manoj, K. M. & Hager, L. P. Chloroperoxidase, a janus enzyme. *Biochemistry* **47**, 2997–3003 (2008).

40. Warren, J. J., Tronic, T. A. & Mayer, J. M. Thermochemistry of Proton-Coupled Electron Transfer Reagents and its Implications. *Chem. Rev.* **110**, 6961–7001 (2010).

41. Mayer, J. M. Hydrogen Atom Abstraction by Metal-Oxo Complexes: Understanding the Analogy with Organic Radical Reactions. *Acc. Chem. Res.* **31**, 441–450 (1998).

42. De Visser, S. P., Kumar, D., Cohen, S., Shacham, R. & Shaik, S. A Predictive Pattern of

Computed Barriers for C-H Hydroxylation by Compound I of Cytochrome P450. *J. Am. Chem. Soc.* **126**, 8362–8363 (2004).

43. Zámocký, M., Furtmüller, P. G. & Obinger, C. Evolution of structure and function of Class I peroxidases. *Archives of Biochemistry and Biophysics* **500**, 45–57 (2010).

44. Zamocky, M., Jakopitsch, C., Furtmüller, P. G., Dunand, C. & Obinger, C. The peroxidase-cyclooxygenase superfamily: Reconstructed evolution of critical enzymes of the innate immune system. *Proteins Struct. Funct. Genet.* **72**, 589–605 (2008).

45. Battistuzzi, G., Bellei, M., Bortolotti, C. A. & Sola, M. Redox properties of heme peroxidases. *Archives of Biochemistry and Biophysics* **500**, 21–36 (2010).

46. Morgenstern, I., Klopman, S. & Hibbett, D. S. Molecular evolution and diversity of lignin degrading heme peroxidases in the agaricomycetes. *J. Mol. Evol.* **66**, 243–257 (2008).

47. Poulos, T. L. Heme Enzyme Structure and Function. *Chem. Rev.* **114**, 3919–3962 (2014).

48. Sitter, A. J., Reczek, C. M. & Terner, J. Heme-linked Ionization of Horseradish Peroxidase Compound II Monitored by the Resonance Raman Fe(IV)=O Stretching Vibration. *J. Biol. Chem.* **260**, 7515–22 (1985).

49. Sitter, A. J., Reczek, C. M. & Terner, J. Observation of the FeIVO stretching vibration of ferryl myoglobin by resonance Raman spectroscopy. *Biochim. Biophys. Acta (BBA)/Protein Struct. Mol.* **828**, 229–235 (1985).

50. Podjarny, A. *et al.* X-ray crystallography at subatomic resolution. *Europhysics News*. **33**, 113-117 (2002).

51. Yosca, T. H. *et al.* Spectroscopic Investigations of Catalase Compound II: Characterization of an Iron(IV) Hydroxide Intermediate in a Non-thiolate-Ligated Heme Enzyme. *J. Am. Chem. Soc.* **138**, 16016–16023 (2016).

52. Kwon, H. *et al.* Direct visualization of a Fe(IV)-OH intermediate in a heme enzyme. *Nat. Commun.* **7**, 13445 (2016).

53. Kwon, H., Smith, O., Raven, E. L. & Moody, P. C. E. Combining X-ray and neutron crystallography with spectroscopy. *Acta Crystallogr. Sect. D, Struct. Biol.* **73**, 141–147 (2017).

54. Gumiero, A., Metcalfe, C. L., Pearson, A. R., Raven, E. L. & Moody, P. C. E. Nature of the Ferryl Heme in Compounds I and II. *J. Biol. Chem.* **286**, 1260–8 (2011).

55. Klingenberg, M. Pigments of rat liver microsomes. *Arch. Biochem. Biophys.* **75**, 376–386 (1958).

56. Omura, T. & Sato, R. The Carbon Monoxide-binding Pigment of Liver Microsomes. *J. Biol. Chem.* **239**, 2370–2378 (1964).

57. J-L, S. Analyse spectrale: Sur le spectre d’absorption du sang dans la partie violette et ultra-violette. *Comptes rendus l’Académie des Sci.* **97**, 1269–1273 (1883).

58. Pettersen EF, Goddard TD, Huang CC, Meng EC, Couch GS, Croll TI, Morris JH, F. TE. UCSF ChimeraX: Structure visualization for researchers, educators, and developers. *Protein Sci.* 70–82 (2021).

59. Frisch, M. J. *et al. Gaussian 16*. (2016).

60. Schrodinger LLC. The PyMOL Molecular Graphics System, Version 1.8. (2015).

61. Emsley, P., Lohkamp, B., Scott, W. G. & Cowtan, K. Features and development of Coot. *Acta Crystallogr. Sect. D Biol. Crystallogr.* **66**, 486–501 (2010).

62. Liebschner, D. *et al.* Macromolecular structure determination using X-rays, neutrons and electrons: Recent developments in Phenix. *Acta Crystallogr. Sect. D Struct. Biol.* **75**, 861–877 (2019).

# Chapter II: Ascorbate Peroxidase Compound II is an Iron(IV) Oxo Species

## Introduction: The protonation state of APX-II:

The greater importance of the protonation state of ascorbate peroxidase Compound II (APX-II) lies in its connection to our understanding of the contributing factors that control metal-oxos and how Nature catalyzes C-H bond activation. Only thiolate-ligated heme enzymes such as cytochrome P450 (P450) and chloroperoxidase (CPO) are known to activate C-H bonds.[1–4] It has been argued that the strong electron donation from the axial thiolate ligand in P450 both increases the reactivity Compound I toward C-H bonds while at the same time protecting the enzyme from autoxidative damage by lifting the pKa of Compound II and favoring productive oxidation of substrate instead of the protein itself.[5–8]

It is the strong electron donation from an axial thiolate ligand that is responsible for the basic ferryl intermediate species Compound II.[5,6,9–11] Spectroscopic measurements of P450 Compound II (P450-II) show that it is best described as an Fe(IV)-OH species with a $pK_a$ of ~12.[6] At present, metal-hydroxide $pK_a$s (or metal-oxo basicities) form an essential component of our understanding of metal-oxo-mediated C-H bond activation.[12–22] In P450s, the elevated value of the $pK_a$ suggests a role for the thiolate ligand in promoting C-H bond cleavage at biologically viable reduction potentials, balancing reactivity of the principle oxidant species Compound I and the O-H bond strength of the product species of the initial hydrogen atom abstraction, Compound II.[6]

Histidine-ligated peroxidases (such as ascorbate peroxidase) produce similar compound I and Compound II species, although they typically function through two successive one-electron oxidations of their substrates.[2,23] They have not been shown to activate C-H bonds. As the histidine ligand is not as donating as the thiolate ligand, histidine-ligated Compound II species are generally thought to be more electrophilic in nature. Consequently, and in stark contrast for thiolate-ligated Compound II, there are no spectroscopic data to support the existence of an iron(IV) hydroxide species in histidine-ligated heme proteins.[24] Resonance Raman experiments on horseradish peroxidase Compound II (HRP-II) have shown an iron(IV) oxo stretch at pD 4, indicating that the $pK_a$ of HRP-II is $\leq 3.6$, while Mössbauer, resonance Raman, and X-ray absorption spectroscopies have been used to place an upper limit of $pK_a \leq 2.7$ for myoglobin Compound II, consistent with the view for an electrophilic species..[25,26]

The recent assignment of iron(IV) hydroxide center in APX-II mentioned in the prior chapter is at odds with the spectroscopic data for similar species, but the report is compelling.[27] Joint X-ray and neutron crystallographic structural data of APX-II in this report produced an Fe-O bond distance of ~1.88 Å. The neutron data reveal a cigar-shaped density what appears to be a hydroxide ligand bound to the heme iron. The investigators have argued that the presence of the hydroxide ligand indicates that APX-II is best described as an iron(IV) hydroxide species. However, the reported Fe-O bond distance is reminiscent of the distances found in photoreduced crystals of other histidine-ligated Compound II species.[28–32] However, the neutron crystallography method utilized should not produce such photoreduction artifacts.[33]

In the early 2000s, several high-resolution X-ray crystal structures of histidine-ligated Compound II were showing longer Fe-O bonds that were indicative of ferryl protonation. These long Fe-O bonds were, however, at odds with several spectroscopic measurements that pointed to a genuine iron(IV) oxo description for histidine-ligated Compound II[24,28] Thorough investigations of the disagreement between X-ray crystallography and spectroscopic data had led researchers to the conclusion the radiation dosage delivered during high-resolution X-ray experiments was sufficient to induce photoreduction of the heme iron, lengthening the Fe-O bond.[28,34,35] The ferryl centers within these crystals had been reduced to ferric or ferrous hydroxide species during the experiment. Later efforts to obtain the pristine and unreduced histidine-ligated Compound II structure pursued multicrystal techniques (limiting individual dosage-per-crystal and merging a structure from multiple diffraction maps) and the use of free electron lasers, both reporting authentic iron(IV) oxo centers in these systems.[34,35]

The 1.88 Å Fe-O distance reported for APX-II is too long to be associated with a histidine-ligated iron(IV) hydroxide intermediate, which should have an Fe-O distance of ~1.76 Å.[11,24,28,36,37] A 1.88 Å bond distance is situated right within the range expected for a ferric hydroxide species.[28] Photoreduction to a cryo-trapped ferric hydroxide species in an X-ray structure of a histidine-ligated Compound II crystal would not be unprecedented, given the history of problems associated with photoreduction in the X-ray beam. What makes this APX-II report so intriguing is that it employed neutron diffraction techniques that do not suffer from the effect of photoreduction.[33,38] However, while the neutron data appear to show a hydroxide ligand bound to the heme iron, they do not also reveal the oxidation state of the iron-hydroxide species within the crystal. Additionally, while the authors of the APX-II 2016 study went to great lengths using microspectrophotometry and X-ray fluorescence techniques to confirm the formation of an iron(IV) intermediate in APX-II crystals, it is not clear that these techniques were applied to the actual crystal used for neutron data collection as no control experiments were reported for the exact crystal.[27] As detailed in chapter III of this dissertation, it is also not clear that the initial multicrystal X-ray experiments on APX-II preserved the ferryl state.[37]

The existence of an iron(IV) hydroxide species in APX-II would be a clear outlier in peroxidase and globin chemistry. Given the central role of metal hydroxide $pK_a$s in metal-oxo-mediated C-H bond activation, it is important to understand if a histidine ligated-heme can support a genuine iron(IV) hydroxide center. In the past, it has been shown that a mixture of spectroscopic methods can be used to accurately determine the protonation state of ferryl species. The following chapter is our effort to characterize APX-II.

## Experimental Methods:

### Cloning the ascorbate peroxidase gene from *Glycine max:*

The gene APX1, cytosolic ascorbate peroxidase 1 from *Glycine max* soybean (UniProt Q43758_SOYBN) was codon-optimized for E. *coli* K12. A TEV protease cut site was added to the N-terminus of this (ENLYFQS)G where the following glycine residue comes from the amino acid residue following the start codon in the native sequence. A 6x histidine sequence was added to the N-terminus, following a new start codon. The whole gene construct was cloned into the pCWori vector by the ThermoFisher GeneArt Gene Synthesis service.

### Expression and Purification of ascorbate peroxidase:

Soybean ascorbate peroxidase was expressed in *E. coli* BL21 (DE3) cells for 36 hours in 2XYT media at 30 °C using ampicillin and IPTG induction. $^{57}$Fe APX was expressed in M9 minimal media for 48 hours with isotopic iron ($FeCl_3$) and induced with IPTG. Cells were harvested by centrifugation and lysed through sonication. Cell debris was removed through centrifugation before the lysates were subjugated to ammonium sulfate fractionation, where APX was found in the 40-50% ammonium sulfate fraction. This fraction was washed excessively with distilled water using an Amicon stirred cell and centrifuged at 20,000 rcf to remove a large portion of the protein content which precipitated from the low ionic strength leaving a clarified red solution. The solution was buffer exchanged into 50 mM Tris-HCl pH 6.4, filtered, and loaded on to a Q-Sepharose Fast Flow anionic exchange column. The column was washed with 50 mM Tris-HCl pH 6.4 and eluted with 250 mM KCl in the same buffer. All eluted fractions were collected and washed with distilled water via stirred cell buffer exchange, centrifuged to remove precipitated proteins, and then loaded onto a Q-Sepharose High Performance column. This was eluted with a gradient from 0 to 250 mM KCl in 50 mM Tris-HCl pH 6.4 after washing with multiple column volumes of the KCl-free buffer. Fractions with high $R_z$ values ($\geq 1.6$) were combined and loaded onto a size exclusion column, run in 50 mM potassium phosphate buffer, pH 7. Fractions were kept with $R_z$ values above 2, yielding a final protein purity of $R_z$ 2-2.2. Purified enzyme was frozen in liquid nitrogen for long-term storage in 1 ml aliquots at 1 mM. These aliquots were thawed immediately before sample preparation.

Notably, the original strategy planned for this purification was to use $Ni^{2+}$ Affinity chromatography and a polyhistidine tag on the N-terminus of APX for a faster procedure. Once bound to the nickel column, the protein can be eluted using two different methods – either the polyhistidine tag can be out-competed by the addition of imidazole, or the protonation state of the histidine monomers on the polyhistidine chain can be altered by lowering the pH, causing the $Ni^{2+}$/polyhistidine interaction to weaken and elution of the protein in what is referred to as the acid-elution method. The acid-elution method requires that the eluted fractions be received in a strongly buffered solution, such that the protein is not kept for very long at the lower pH. Neither method was suitable for our purposes. Imidazole-elution resulted in an irreversibly changed ferric spectrum for APX and a species that is no longer competent to produce APX-II. Using acid-elution methods produced very low $R_z$ values and limited the purity maximum achievable – following receiving the acid-eluted protein was a heme reconstitution step (as much of the heme dissociated with the drop in pH), and this step does not have much success meaning > 75% of the APX is lost at this stage. This was not suitable for our sample requirements.

The ammonium sulfate fractionation strategy was inspired by a 1991 paper by Mittler and Zilinskas in which snow pea ascorbate peroxidase was purified from the native organism.[39] The authors very slowly added ammonium sulfate to 50%. This method worked for us as a replacement for the $Ni^{2+}$ column. The method we developed was as follows: First, quickly add ammonium sulfate to 30% and centrifuge at 20,000 rcf to precipitate a large amount of protein content. The supernatant is kept and more ammonium sulfate is slowly added from 30% to 40% while gently stirring. Once completely dissolved, this is centrifuged again, and the precipitate is rejected. The supernatant is kept and again gently stirred, slowly increasing the ammonium sulfate from 40% to 50%. A large color change occurs as the clear deep red protein turns more milky and opaque clay-colored. This solution is then centrifuged, with ascorbate peroxidase in the precipitate. Once resolubilized in water, $R_z$ values should be 0.2 – 0.5, and most of the enzyme mass is retained, compared to $Ni^{2+}$ affinity methods.

The two ion exchange columns serve much of the cleaning work of purification. The first ion exchange column is a flow-through in which the protein content that binds to the column is removed from the flow-through which contains APX and 250 mM KCl. By doing a flow-through Fast Flow column before moving on to the High Purity column, higher $R_z$ values can be achieved because the gradient over the High Purity column is flowing through a much smaller protein mass making for a more even chromatogram with better flow. As there is a large protein content that remains bound to the column at 250 mM KCl (but washes off with 3M NaCl), it is best to remove that with a Fast Flow column, earlier. Careful handling of samples can result in $R_z = 2.2$ after the High Purity column, making size exclusion chromatography unnecessary. This is favorable because of the mechanical parameters around size exclusion chromatography – using ~2 mL dosages of high concentrated enzyme wastes a significant amount of sample lost in filters and small leaks and takes many runs to produce the volumes of enzyme needed for the spectroscopic techniques employed in this work.

### UV/Visible Spectroscopy of APX-II:

Ferric APX (11 µM) was reacted with 5 equivalents of *m*-CPBA in a 50 mM potassium phosphate pH 7 buffer. Spectra were recorded after maximum APX-II formation using a Cary-50 UV/Visible spectrophotometer.

### Preparation of Samples:

APX-II Mössbauer / XAS samples (~3 mM, ~90% yield) were made through reacting ferric APX with 5 equivalents of *m*-CPBA. The reaction was aged for several seconds and then rapidly quenched in liquid ethane. Mixing was performed by hand. Ethane was removed quickly at -80 °C, and samples were stored at 77 K.

### Electron Paramagnetic Resonance Spectroscopy (EPR):

Data were recorded on a Bruker EMX EPR spectrometer operating in X-band (9-10 GHz) with an Oxford ESR900 helium cryostat. Experiments were carried out at 20 K unless otherwise noted.

### Mössbauer Spectroscopy:

Data were collected using a spectrometer from WEB research in constant acceleration mode using transmission geometry and a 50 mT magnetic field applied parallel to the γ-beam. Spectra were recorded at 4.2 K using a Janis SVT400 cryostat. Isomer shifts were calibrated using the centroid of the spectrum of a foil of α-Fe at room temperature. Data analyses were performed using the program WMOSS from WEB research.

### X-ray Absorption Spectroscopy (XAS):

XAS data were collected in fluorescence mode at 10 K with a 30-element germanium detector (SSRL, BL7-3) using a Si(220) Phi = 0° double monochromator with a 9.5 keV cutoff for harmonic rejection. Mounted samples were moved in the beam after each scan to an unexposed region of the sample to minimize the effect of photoreduction. Thirty-six first scans were included in the APX-II EXAFS data set. Fitting of EXAFS and pre-edge data were performed using EXAFSPAK.

## Results and Discussion:

Our stopped-flow UV/Visible measurements revealed that in the reaction of ferric APX with the two-electron oxidant *m*-chloroperbenzoic acid, APX Compound I is first generated (APX-I, and iron(IV) oxo porphyrin radical species). In the absence of substrate, APX-I decays through oxidation of a protein residue to generate a cytochrome *c* peroxidase (CcP) Compound ES-like species, which has been referred to in the literature as APX-II.[23] We believe this residue is Trp179, analogous to the tryptophan residue in CcP oxidized upon CcP-ES formation, although the location of the protein radical has not been investigated here. Figure 2.1 shows the UV/Visible spectra of ferric APX and APX-II. The spectra are similar to those reported previously.[27,40] Figure 2.2 shows the EPR spectrum of APX-II, revealing a single S = 1/2 signal for a protein radical species consistent with the single unpaired electron on the protein from autooxidation as APX goes from APX-I to APX-II.

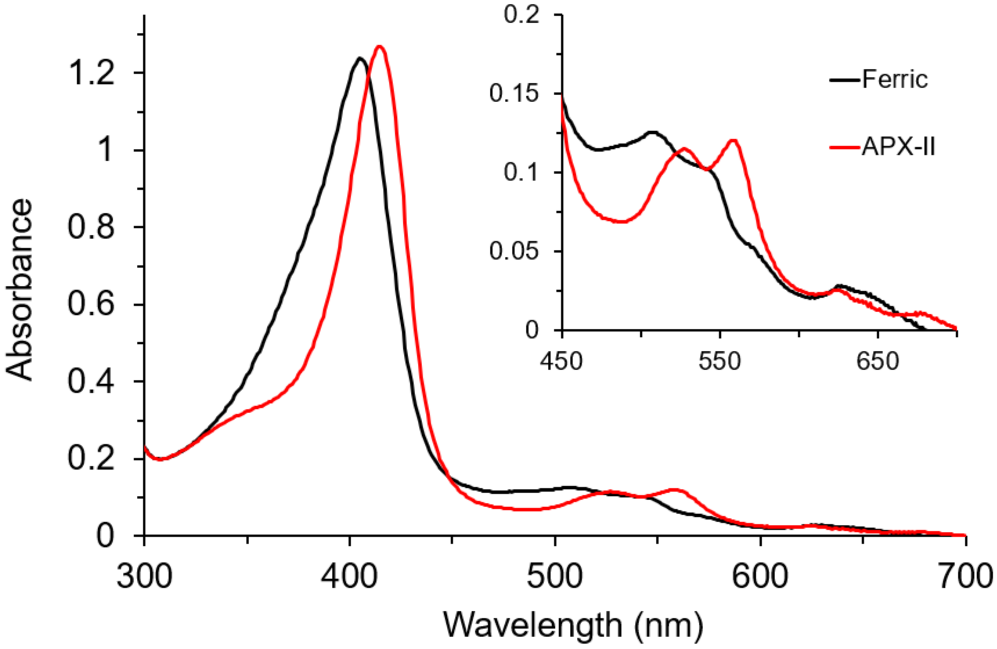

**Figure 2.1**: UV/Visible spectra of ferric APX (black) and APX-II (red) in 50 mM potassium phosphate, pH 7. Ferric APX displays a Soret maximum at 405 nm and Q bands at 509 and 544 nm. APX-II has a Soret maximum at 418 nm and Q bands at 528 and 559 nm.

Notably, the term ES-like intermediate indicates that the protein intermediate remains as a whole two oxidizing equivalents above the ferric resting state, but one of the oxidizing equivalents of Compound I has moved from the heme-cofactor, off of the porphyrin and on to an oxidizable residue within the protein framework.[6,41] The electronic coupling between the iron(IV) center and the protein radical in these ES-like intermediates is typically nonexistent or very weak.[6,23,41–44] In CcP-ES, the exchange coupling is 1-2 orders of magnitude weaker than it is in horseradish peroxidase Compound I.[41] As a result of these very weak couplings, the chemistry and spectroscopic signatures of the iron(IV) centers in these ES-like systems are typically indistinguishable from authentic Compound II species. It is standard to refer to these Compound

ES-like species as Compound II intermediates when the focus of discussion is solely around the heme cofactor. [6,27]

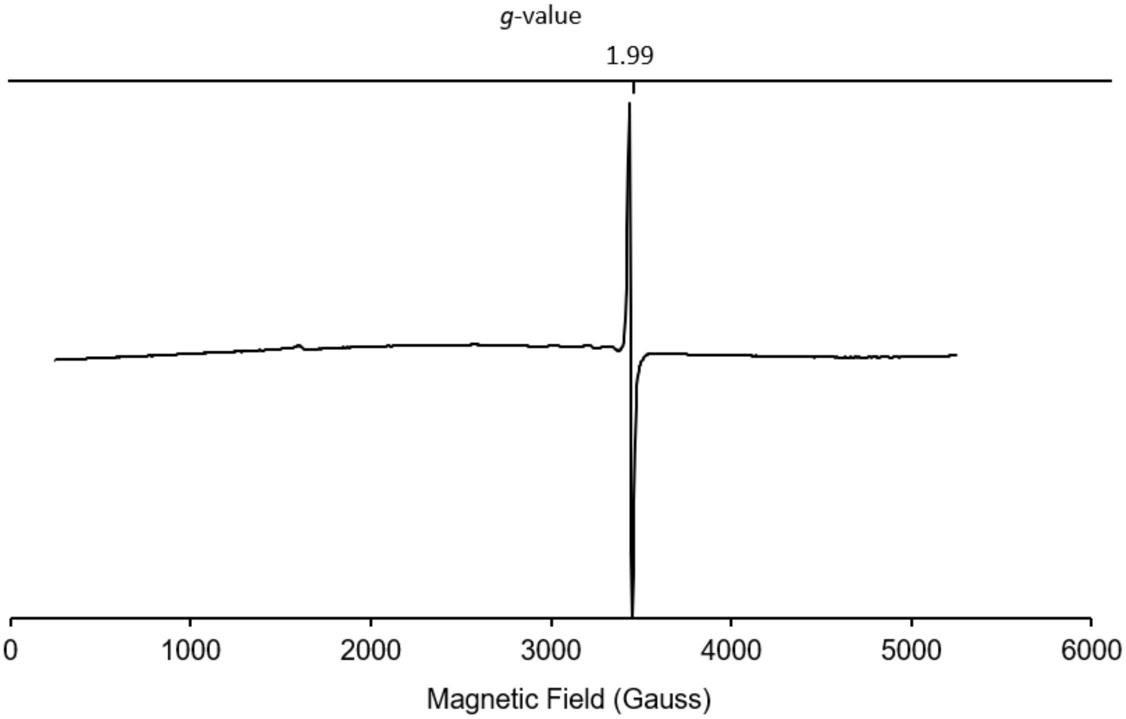

**Figure 2.2**: X-band EPR spectrum (10 K, 2 mW) of APX-II formed by reacting ferric enzyme with 5 equivalents of meta-chloroperbenzoic acid.  This was the same sample examined through XAS and Mössbauer.

We scaled up our preparation of APX-II for spectroscopic measurements using insights gained from stopped-flow experiments. APX-I has a $t_{1/2}$ = 2.55 seconds, converting to APX-II which persists on the scale of 100s of seconds. APX-II samples (~3 mM, ~90% yield) for Mössbauer and X-ray absorption spectroscopies were prepared by hand mixing ferric enzyme with 5 equivalents of *m*-CPBA, and aging the reaction mixture for was aged for five seconds to allow for maximum APX-II formation while mixing with a micropipette prior to rapidly freezequenching the reaction by spraying into liquid ethane (90 K). The liquid ethane was subsequently removed at -80 °C, and the sample was then packed into Mössbauer and XAS sample holders at 77 K.

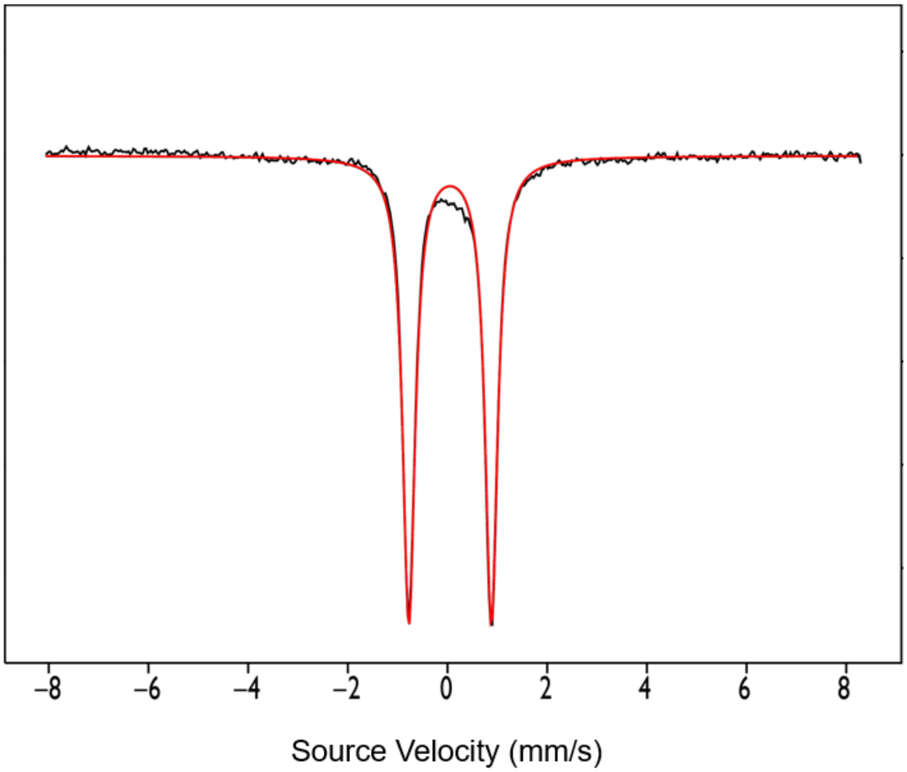

**Figure 2.3**: Mössbauer spectrum (4.2 K, 50 mT) of APX-II EXAFS sample (50 mM potassium phosphate, pH 7). APX-II was generated in ~90% yield. Raw data are shown in black. The fit is shown in red. Parameters obtained from fitting are $\Delta E_q$ = 1.65 mm/s and δ = 0.03 mm/s.

We employed Mössbauer spectroscopy as our initial method of characterization and as our test for sample purity. Mössbauer spectroscopy is an excellent tool for determining the oxidation state and the local bonding environment of the iron atom at the center of the heme cofactor. The isomer shift, δ, provides insight into the oxidation state, while the quadrupole splitting, $\Delta E_q$, can be used to track the protonation state of the ferryl oxygen. It has been shown that $\Delta E_q$ increases quite significantly upon ferryl protonation. In P450-II, for example, $\Delta E_q$ increases from 1.30 to 2.02 mm/s when the ferryl oxygen is protonated, and similar results were observed for the thiolate-ligated chloroperoxidase Compound II.[6,45] Importantly, the sensitivity of this technique lies in how multiple species of iron will overlay, yet can be separated from each from their different features.

Figure 2.3 shows the Mössbauer spectrum of APX-II (pH 7, 4.2 K). APX-II consists of a single quadrupole doubled with an isomer shift of $\delta = 0.03$ mm/s and a quadrupole splitting of $\Delta E_q = 1.65$ mm/s. These values are typical of those found for histidine-ligated iron(IV) oxo porphyrin species.[24] Myoglobin Compound II (Mb-II) has values of $\delta = 0.07$ mm/s and a quadrupole splitting of $\Delta E_q = 1.58$ mm/s at pH 3.9, while horseradish peroxidase Compound II (HRP-II) has values of $\delta = 0.03$ mm/s and $\Delta E_q = 161$ mm/s at pH 6.9.[26,46] X-ray absorption and resonance Raman measurements have additionally verified that Mb-II and HRP-II are authentic iron(IV) oxo species.[25,26,46] The similarity between the Mössbauer parameters of APX-II and those found for Mb-II and HRP-II suggests that APX-II is also an iron(IV) oxo species at pH 7.

Figure 2.4 shows the ferric spectrum for APX at 4 K. It is radically different from Figure 2.3 in the main text describing APX-II, and there is clearly no presence of ferric enzyme in Figure 2.3. The spectrum reflects a mixture of high- and low-spin ferric heme, at $S = 5/2$ and $1/2$, respectively.

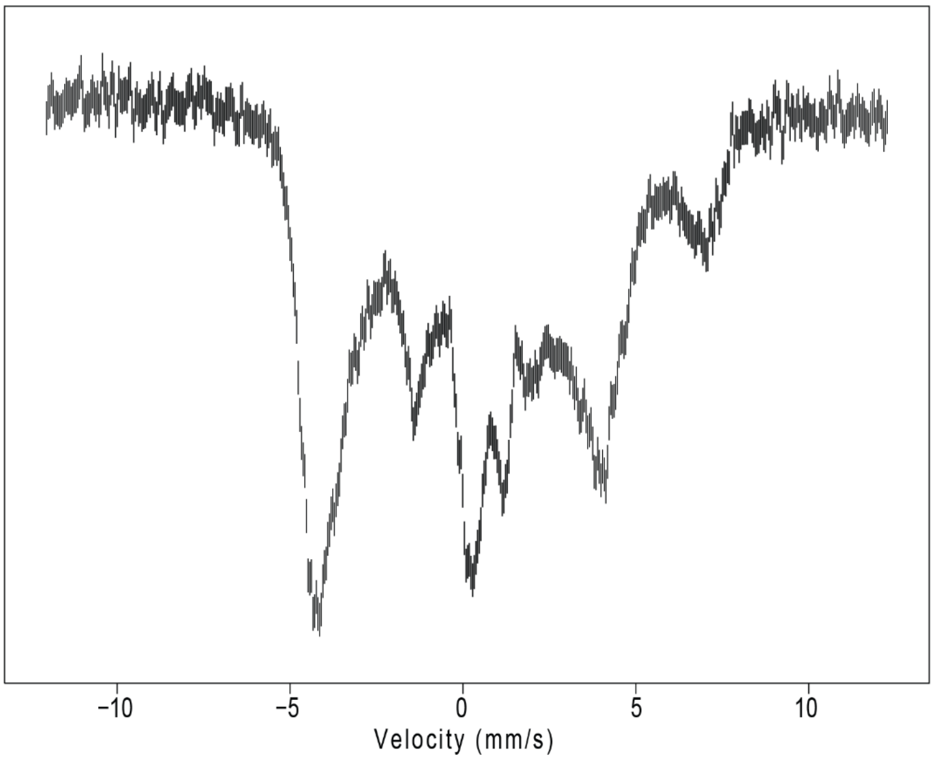

**Figure 2.4**: Mössbauer spectrum (4.2 K, 50 mT) of 3 mM ferric APX in 50 mM potassium phosphate, pH 7.

We were also concerned about the presence of APX-I in our APX-II samples. Figure 2.5 shows the UV/Visible absorption spectrum for APX-I. This species reacts to form APX-II on the scale of seconds at the 10 µM level. In order to establish that no APX-I was present in our scaled-up APX-II samples, we scaled up this reaction to the same 3 mM concentration for EPR and Mössbauer characterization.

Figure 2.6 show the EPR spectrum of APX-I. Spectra of APX-I were obtained through a variable temperature experiment, through which it was determined that the signal present at 3.4 K but not at 10 K best resembles literature data for Compound I.[47,48] Features at 3.42 and 1.99 are similar to APX-I in pea that was assigned to a porphyrin π-cation radical.[48] The 5.85 and 5.05

features come from residual ferric APX in the sample that do produce a single difference between 10 and 3.4 K, although in the following Mössbauer spectrum (Figure 2.7), it will be clear that very little ferric APX is present.

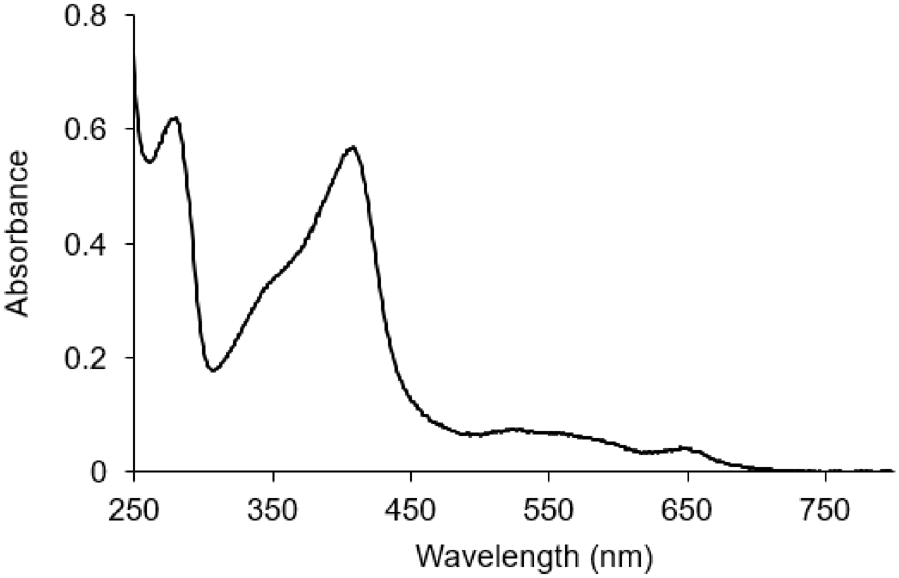

**Figure 2.5**: UV/Visible spectra of APX-I (275 ms), produced after the addition of 5 equivalents *m*-CPBA to 10 mM ferric APX in 50 mM potassium phosphate buffer, pH 7. Absorption features of APX-I are: 409 Soret, 530, 573sh, and 630 nm.

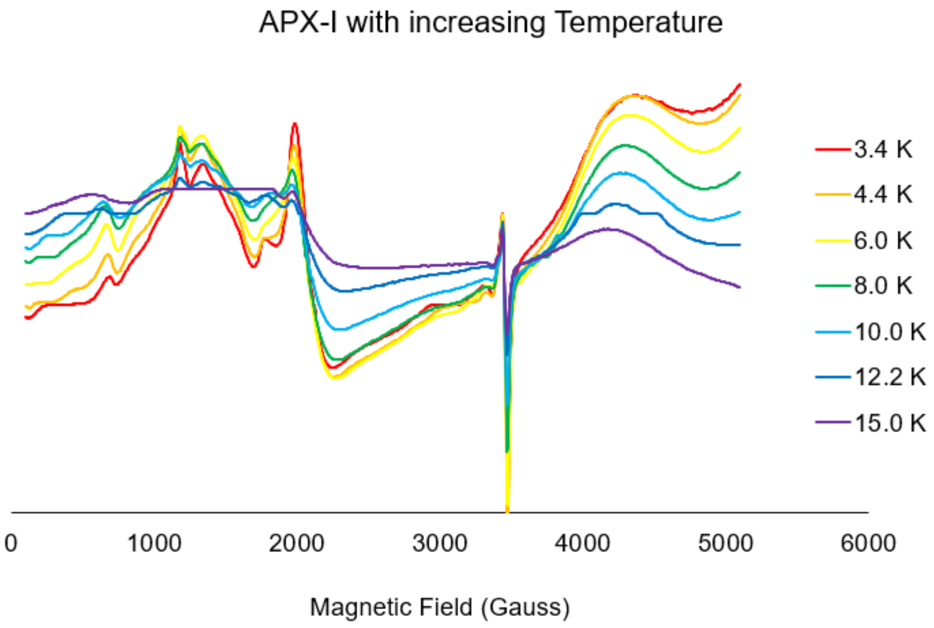

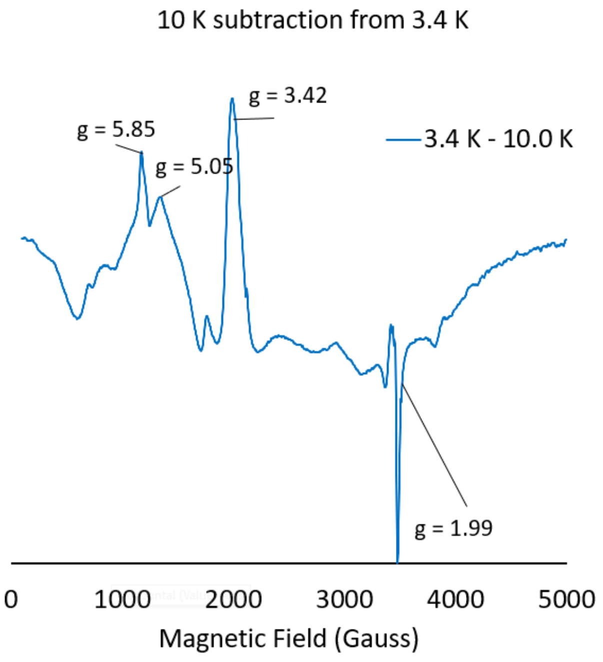

**Figure 2.6:** (Top): EPR spectra of APX-I were obtained through a variable temperature experiment, through which it was determined that the signal present at 3.4 K but not at 10 K best resembles literature data for Compound I species in other histidine-ligated heme enzymes. The spectra here are of the full set of temperatures. (Bottom): Difference spectrum between 10 K and 3.4 K data. The EPR difference spectrum resolves features at 3.42 and 1.99, along with 5.05 and 5.85. Features at 3.42 and 1.99 are similar to APX-I in pea that was assigned to a porphyrin π-cation radical. The 5.85 and 5.05 features come from residual ferric APX in the sample.

Figure 2.7 shows Mössbauer spectrum of APX-I revealing a narrower $\Delta E_q$ = of 1.343 mm/s and $\delta = 0.06$ mm/s at 77 K. It would be easily discernable in the spectrum of APX-II at 4.2 K in the Figure 2.3 spectrum if any APX-I was present.

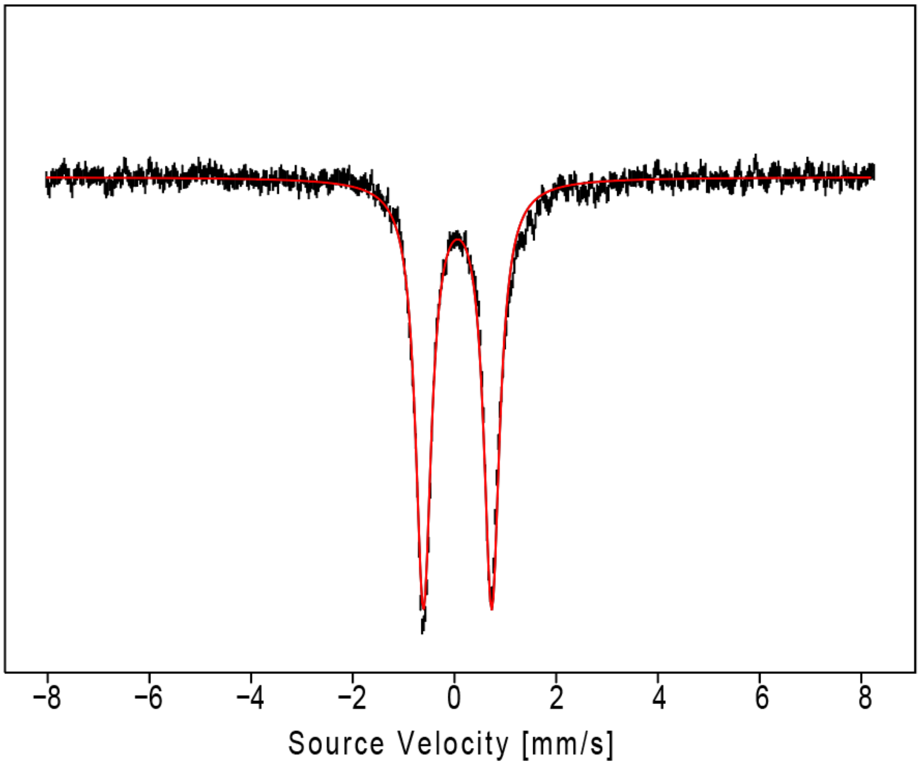

**Figure 2.7:** Mössbauer spectrum (77 K, 50 mT) of APX-I in 50 mM potassium phosphate, pH 7. This is the same sample as Figure 2.6. This best fits as a quadrupole doublet with a $\Delta E_q$ of 1.34 mm/s and an isomer shift of $\delta = 0.06$ mm/s, indicative of ferryl enzyme. Importantly, a $\Delta E_q$ of 1.34 mm/s is substantially smaller than 1.65 and a mixture of APX-I/APX-II would clearly show two sets of quadrupole doublets – a separation of 0.3 mm/s is well within the detection limits for this experiment. The previously shown Mössbauer spectrum of APX-II was taken at 4.2 K – at that temperature it is expected that APX-I would not be a quadrupole doublet as shown here to the right. APX-II's quadrupole doublet does not change between 4.2 and 77 K however, allowing examination of sample purity at liquid nitrogen temperatures. At 77 K, ferric APX collapses to a quadrupole doublet with a $\delta = 0.32$ mm/s and $\Delta E_q = 2.391$ that is not visibly present in this sample by Mössbauer spectroscopy (Figure 2.S1)

Our second approach to probe the protonation state of APX-II was through X-ray absorption spectroscopic techniques. Both the extended X-ray absorption fine structure (EXAFS) and the pre-edge regions contain information about the Fe-O bond distance, which is directly related to the ferryl protonation state. As iron(IV) oxo species possess a double bond between the iron and the oxygen atoms, the internuclear Fe-O distance is typically on the order of ~1.65 Å. This short Fe-O bond creates an asymmetric ligand field that increases the intensity of formally forbidden $Fe_{1s\text{-}\rightarrow 3d}$ pre-edge transitions through 4p mixing.[49] Protonation of the ferryl moiety reduces the Fe-O bond order, increasing the Fe-O bond length and diminishing the intensity of the pre-edge feature.

We investigated both the pre-edge and EXAFS regions for APX-II. All XAS samples were examined by Mössbauer spectroscopy prior to the XAS data collection, allowing us to confirm preparation of Compound II intermediate. This was done by performing a single reaction at a large enough volume to fill multiple sample holders. Additionally, measures were taken to minimize the effects of photoreduction during data collection by moving XAS samples in the X-ray beam such that unexposed portions of the sample were freshly examined for each scan. The effects of photoreduction were then monitored by comparing first and second scans of an individual location on the sample holder. Data sets used for final analyses were comprised of first scans only. Experiments were reproduced using two different preparations of APX-II. Complete *K*-edge spectra are in Figure 2.8.

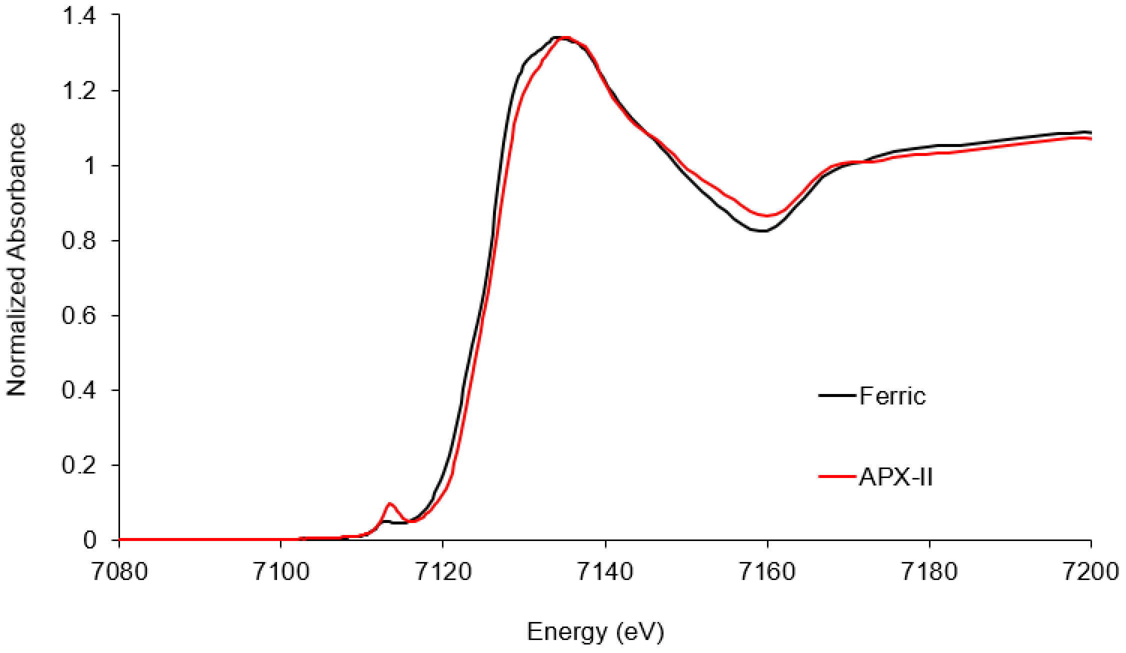

**Figure 2.8:** Comparison of *K*-edge X-ray absorption spectra for APX-II and ferric APX.

Figure 2.9 shows normalized pre-edge data for APX-II and for the oxo and hydroxide forms of myoglobin (Mb) and cytochrome P450. In the case of cytochrome P450, data for both the iron(IV) oxo and iron(IV) hydroxide forms are shown.[6] For Mb, data are presented for the iron(IV) oxo and iron(III) hydroxide forms.[26] Recall, Mb does not support an iron(IV) hydroxide state, but iron(III) hydroxide has a comparable Fe-O bond distance. P450-II has been shown to exist as an iron(IV) hydroxide species with $pK_a = 12$. The transition of P450-II through the iron(IV) hydroxide $pK_a$ has been tracked with UV/Visible, EXAFS, and Mössbauer spectroscopies.[6] At pH 9, the Fe-O distance in P450-II is 1.84 Å. As the pH increases and the iron(IV) hydroxide species deprotonates, the Fe-O distance shortens to 1.68 Å.

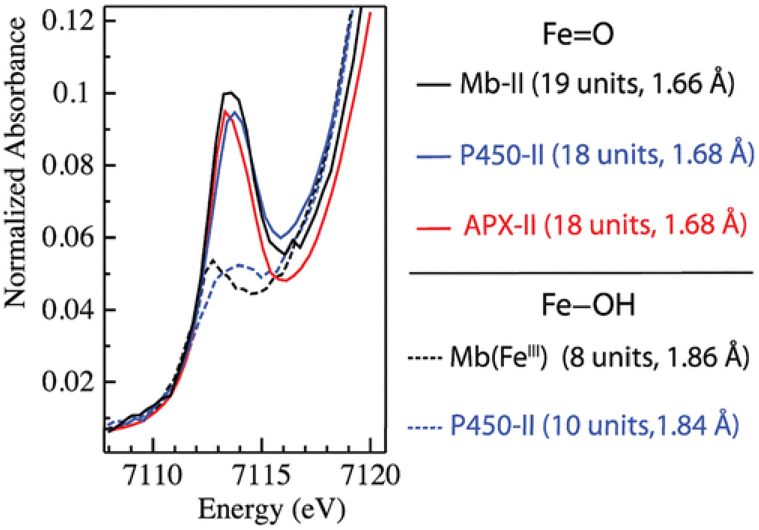

**Figure 2.9.** Pre-edge analysis. Oxo species (Mb-II, P450-II, and APX-II) are shown here with solid lines. Hydroxide species (ferric myoglobin and P450-II) are shown with dashed lines. Pre-edge intensities/areas and Fe–O bond distances are listed for each species.

The P450 data in Figure 2.9 show how the pre-edge intensity can be used as an indicator of the Fe-O distance and protonation state. Pre-edge data for P450-II above (blue line) and below blue dashed line) the iron(IV) hydroxide p$K_a$ are shown. The unprotonated form of P450-II has a prominent pre-edge feature that weakens significantly upon protonation of the ferryl moiety and lengthening of the Fe-O bond. Similar behavior can be seen with Mb. The Mb data are shown in black. Mb-II, which possesses a short Fe-O bond of 1.66 Å, has an intense pre-edge feature (lack line), while the ferric hydroxide form of Mb with an Fe-O distance of 1.86 Å has a much weaker pre-edge feature (black dashed line).[26] The Mb and P450 data suggest that the pre-edge intensity of APX-II can be used to assign the protonation state of the ferryl moiety. The data for APX-II show a pre-edge feature (red line) that is very similar to those obtained for the iron(IV) oxo forms of P450 and Mb and suggests the same ligand assignment.

Pre-edge data of APX-II are consistent with the assignment of an iron(IV) oxo species with a short Fe-O bond. In order to make a more precise evaluation of the bond distance, we collected and analyzed X-ray absorption data in the fine structure region. EXAFS allows for hundredths of an Å resolution fitting of the scattered photon. Figure 2.10 shows the raw and Fourier-transformed (FT) EXAFS data for APX-II, along with fits in blue. The FT data reflect *R*-space distance in Å, corresponding to scattering paths of the ejected 6.4 keV photon.

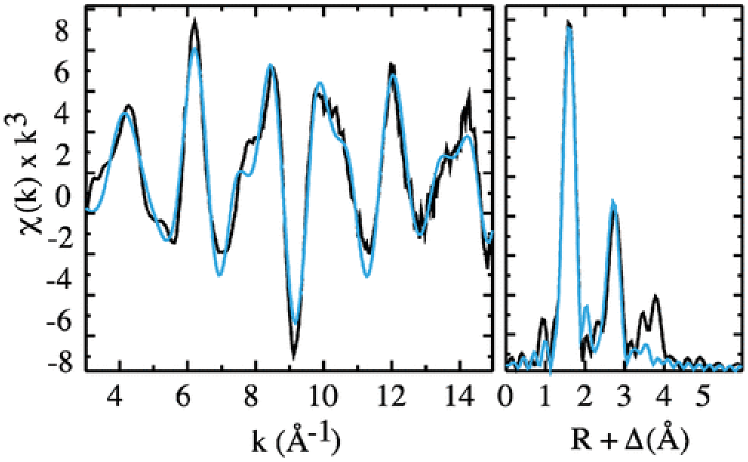

**Figure 2.10.** APX-II EXAFS data (left) and Fourier transform (right). Black lines show experimental data. Blue lines show the best fit to experimental data. Fitting parameters are shown in Table 2.1.

Table 2.1 shows the results of fitting the raw EXAFS data using the program EXAFSPAK and phases and amplitudes generated FEFF 8.x39.[50] The fits included the first- and second-shell atoms around the central Fe atom and one multiple scattering component around the heme macrocycle. The first shell was modeled with two components: one representing five nitrogen atoms (four from the porphyrin and one from the histidine ligand) and the other representing a single oxygen scatterer. The second shell consisted of the atoms from the porphyrin ligand - 8 α carbons, 4 meso carbons, and 16 Fe-Cα-N-Fe multiple scattering paths. Fitting of the APX-II EXAFS data raw yielded an Fe-O distance of 1.68 Å, which indicates that APX-II is an iron(IV) oxo species.  Fits that excluded the short Fe-O scattering path had significantly greater errors. Fitting with a longer Fe-O bond (1.96 Å being the distance indicative of Fe(II)-OH) also has greater error

**Table 2.1:** EXAFS Fitting Results for Raw and Fourier-Filtered APX-II Data[a]

| | Fe-N | | | Fe-O | | | | |
|---|---|---|---|---|---|---|---|---|
| | N | R | $\sigma^2$ | N | R | $\sigma^2$ | $E_0$ | error[b] |
| raw data | 5 | 1.99 | 0.002 | 1 | 1.68 | 0.004 | -15 | 0.277 |
| | 5 | 2.04 | 0.006 | 1 | 1.96 | -0.002 | -12 | 0.357 |
| | 5 | 1.99 | 0.002 | 0 | | | -17 | 0.365 |
| | 6 | 1.99 | 0.003 | 0 | | | -16 | 0.402 |
| Fourier-filtered data | 5 | 1.99 | 0.003 | 1 | 1.68 | 0.003 | -16 | 0.23 |
| | 5 | 1.99 | 0.002 | 0 | | | -18 | 1.01 |
| | 5 | 2.03 | 0.005 | 1 | 1.95 | -0.001 | -15 | 1.15 |
| | 6 | 1.99 | 0.003 | 0 | | | -18 | 1.32 |
| | 5 | 1.99 | 0.002 | 1 | 1.88 | 0.003 | -21 | 1.53 |

[a] Data were fit over the region $k$ = 3–15 Å$^{-1}$. Coordination number *N*, interatomic distance *R* (Å), mean square deviation in *R* (the Debye–Waller factor), $\sigma^2$ (Å$^2$), and the threshold energy shift $E_0$ (eV).

[b] The fit errors listed for the raw data come from the weighted *F* factor which is defined as $[\Sigma k^6(\chi_{\text{exptl}} - \chi_{\text{calcd}})^2/\Sigma k^6\, \chi^2_{\text{exptl}}]^{1/2}$. EXAFSPAK does not report a weighted *F* factor for fits of Fourier-filtered data. For fits of the Fourier-filtered data, the errors listed are the sum of the squares between the calculated and the Fourier-filtered data divided by 100. Best fits are shown in bold. Alternative fits with different coordination numbers are shown also. Coordination numbers, *N*, were constrained during the fits. Distance and Debye–Waller values shown in italic were constrained during the fit.

The highly symmetric nature of the porphyrin macrocycle leads to the shell structure observed in the FT EXAFS. Because all the shells shown in the FT contribute to the raw EXAFS data, it can be difficult to see by eye the need for a single scattering component in fits of the raw. In an effort to make the assignment of APX-II as an iron(IV) oxo species as clear as possible, we included fitting analysis for the EXAFS data obtained by Fourier filtering the first shell of the APX-II data.

The Fourier-filtered (FF) EXAFS can be seen in Figure 2.11. The FF EXAFS data are shown in black, fits are shown in blue, and the difference between the two is shaded/highlighted in red. To obtain the FF EXAFS a window was placed around the first shell of the *R*-space data, and all values outside this window were set to zero. The windowed *R*-space data was then back transformed to *k* space to yield the FF EXAFS, which contains only contributions from the first-shell scatters and accordingly looks much simplified. Fits of the first-shell FF EXAFS data with and without a short Fe–O scattering path clearly suggest that APX-II is an iron(IV) oxo species.

In the top panel of Figure 2.11, the first shell is modeled with only five nitrogen atoms, showing what is missing when a short scatterer is not included. There is significant error (shaded red) in the EXAFS fit. This difference is obvious in the *R*-space data. The middle panel shows the results when a short Fe–O scattering path is added to the first shell. This produces a fit good agreement with the EXAFS/FT data. The bottom panel shows an effort to model the Fe–O scattering path with a longer distance consistent with a hydroxide ligand, the 1.88 Å Fe-O distance reported in the Neutron crystal structure.[27] Fits with the longer Fe-O scattering path consistently optimized to either the shorter 1.68 Å oxo distance or to a distance that was not resolvable from the first-shell nitrogen atoms. To model a hydroxide ligand, it was necessary to restrain the Fe–O distance.

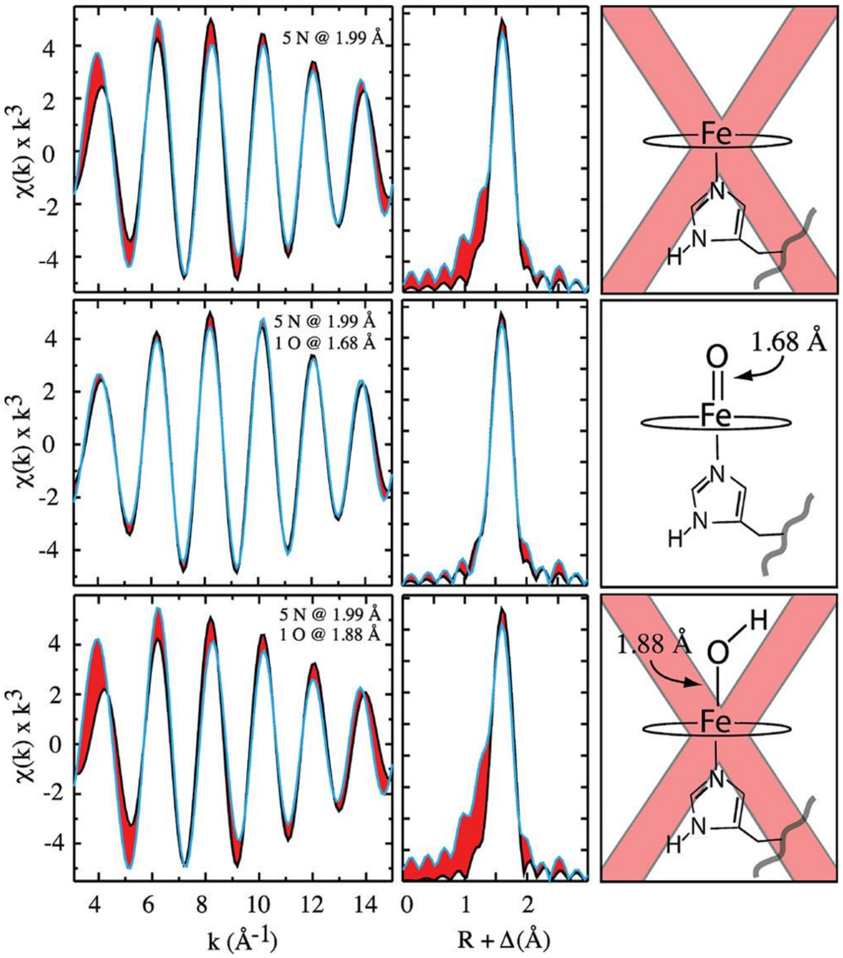

**Figure 2.11:** Analysis of the Fourier-filtered (FF) EXAFS data. FF data are shown in black, and best fits are in blue. The areas shaded in red highlight errors in the fit. (Top): Effort to model the data without an oxygenic ligand, leading to significant error in the fit. (Middle): Fit that includes a short 1.68 Å Fe–O scattering path: there is good agreement between the data and the fit. (Bottom): Effort to model the Fe–O scattering path with a longer distance consistent with a hydroxide ligand. It was not possible to obtain acceptable fits with a hydroxide scattering path. Longer Fe–O scattering paths optimized either to the shorter 1.68 Å oxo distance or to a distance that was not resolvable from the first-shell nitrogen atoms. To model a hydroxide ligand, it was necessary to restrain the Fe–O distance. In the fit shown in the bottom panel, the Fe–O distance was restrained to the value (1.88 Å) reported in the neutron diffraction study. Fitting parameters are listed in Table 2.1.

The Mössbauer and X-ray absorption data detailed above indicate that APX-II is an iron(IV) oxo species at pH 7. Using UV/Visible spectroscopy, we determined that the ferryl oxygen remains unprotonated down to at least pH 5.5, indicating that the p$K_a$ of APX-II is ≤4.5 (Figure 2.12). There is no change in the Soret band observed when pH is lowered. As protonation of the ferryl oxygen reduces the Fe–O bond order, Fe-O bond length is increased, which in turn affects the proximal ligation and the UV/Visible spectrum. In P450-II, this has been shown to result in a significant change in the Soret spectrum: $\lambda_{max}$ shifts from 437 to 426 nm.[6] Protonation of the ferryl oxygen also results in considerable changes in the Q-band region.[6] Using stopped-flow UV/Visible spectroscopy, we prepared APX-II at pH 7 by mixing ferric enzyme with *m*-CPBA and with a second mix jumped the intermediate to pH 5.5. The spectrum of APX-II obtained at pH 5.5 and 7 are essentially identical with no change in the Soret maximum or Q-band region. This indicates no change in protonation state. Assuming that the spectrum of a 90:10 oxo/hydroxide distribution would be distinguishable from that of the iron(IV) oxo species, we can place an upper limit (≤4.5) on the p$K_a$ of APX-II.

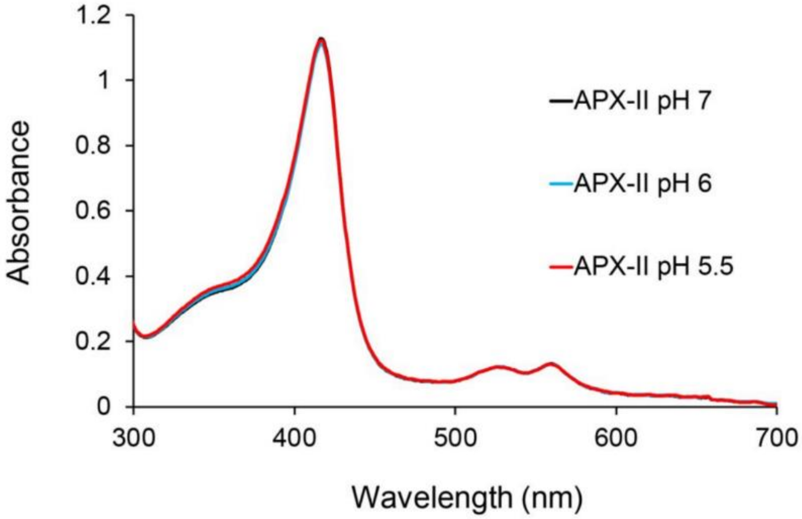

**Figure 2.12:** Comparison of UV/Visible absorption spectra for APX-II at pH 7 (black), pH 6 (blue) and pH 5.5 (red). Samples were prepared in a double-mix stopped-flow experiment. Ferric APX (12.5 mM potassium phosphate, pH 7) was first mixed with 5 equivalents of m-CPBA. After maximum formation, APX-II was mixed with a strongly buffered solution, either 400 mM sodium citrate (pH 5.5 and 6) or 400 mM potassium phosphate (pH 7). Solutions were mixed in a 1:1:2 mixing ratio, yielding the final pH listed above. These results are similar to those reported previously.

## Conclusion:

We utilized Mössbauer and XAS spectroscopies to examine the protonation state of APX-II. While both techniques cannot observe protons directly, it does allow us to determine the composition and oxidation state of the sample and provides a structural metric through the Fe–O bond distance.

Our results indicate that APX-II is not protonated. The Mössbauer parameters, Fe K-edge pre-edge intensity, and Fe–O distance obtained from our measurements indicate that APX-II is best described as an iron(IV) oxo species at pH 7. These results coupled with pH jump stopped-flow UV/Visible spectroscopic measurements set an upper limit ($\mathrm{p}K_a \leq 4.5$) on the APX-II $\mathrm{p}K_a$. Consistent with other histidine-ligated peroxidases, APX possesses a Compound II species with an acidic $\mathrm{p}K_a$, in contrast to the much more basic P450-II ($\mathrm{p}K_a \approx 12.0$).

**Supplementary Data:**

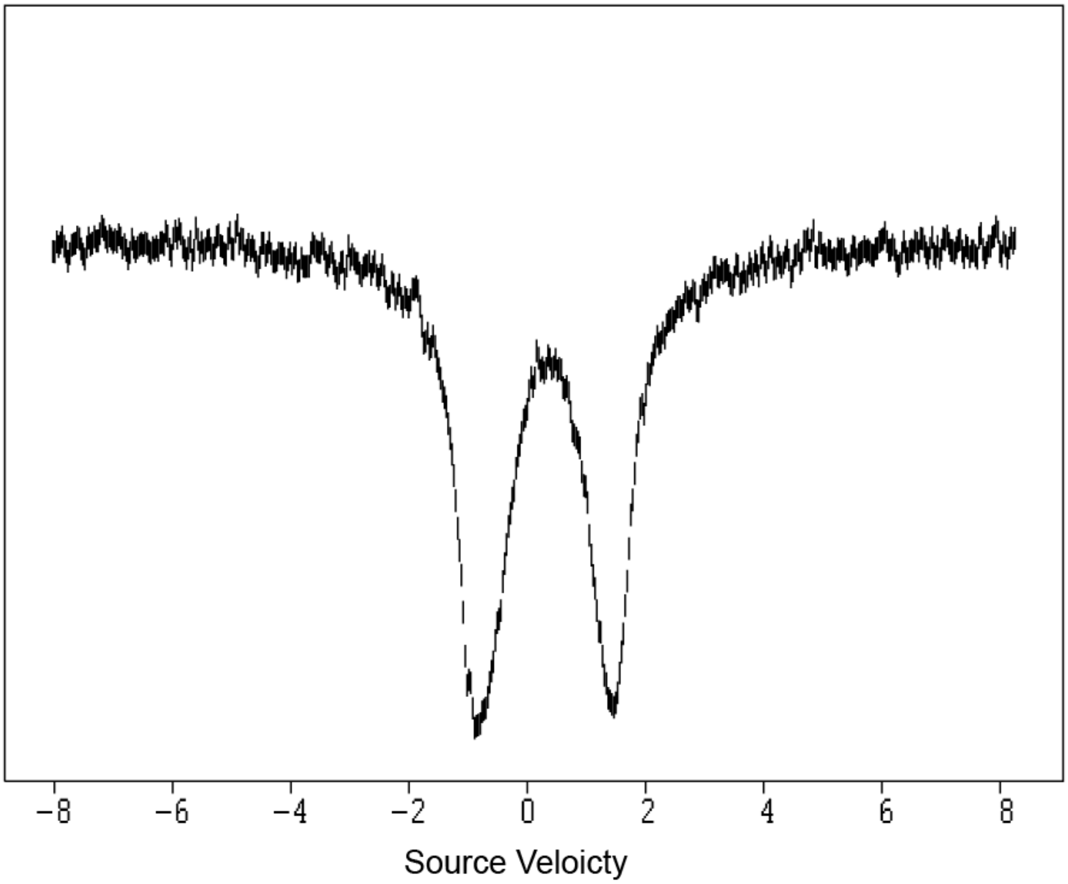

**Figure 2.S1:** Mössbauer spectrum of ferric APX in 50 mM potassium phosphate, pH 7. We note this is the same sample as Figure 2.4. (77 K, 50 mT) This best fits as a quadrupole doublet with a $\Delta E_q$ of 2.391 mm/s and an isomer shift of $\delta = 0.32$ mm/s.

**References:**

1. De Montellano, P. R. O. *Cytochrome P450: Structure, mechanism, and biochemistry: Third edition*. (Springer US, 2005). doi:10.1007/b139087.

2. van Rantwijk, F. & Sheldon, R. A. Selective oxygen transfer catalysed by heme peroxidases: synthetic and mechanistic aspects. *Curr. Opin. Biotechnol.* **11**, 554–564 (2000).

3. Green, M. T. C–H bond activation in heme proteins: the role of thiolate ligation in cytochrome P450. *Current Opinion in Chemical Biology* **13**, 84–88 (2009).

4. Peter, S. *et al.* Selective hydroxylation of alkanes by an extracellular fungal peroxygenase. *FEBS J.* **278**, 3667–3675 (2011).

5. Green, M. T., Dawson, J. H. & Gray, H. B. Oxoiron(IV) in Chloroperoxidase Compound II Is Basic: Implications for P450 Chemistry. *Science.* **304**, 1653–1656 (2004).

6. Yosca, T. H. *et al.* Iron(IV)hydroxide pKa and the Role of Thiolate Ligation in C-H Bond Activation by Cytochrome P450. *Science* **342**, 825-829 (2013).

7. Krest, C. M. *et al.* Significantly shorter Fe–S bond in cytochrome P450-I is consistent with greater reactivity relative to chloroperoxidase. *Nat. Chem.* **7**, 696–702 (2015).

8. Yosca, T. H., Ledray, A. P., Ngo, J. & Green, M. T. A new look at the role of thiolate ligation in cytochrome P450. *J. Biol. Inorg. Chem.* **22**, 209–220 (2017).

9. Behan, R. K., Hoffart, L. M., Stone, K. L., Krebs, C., & Green, M. T. Evidence for Basic Ferryls in Cytochromes P450. *J. Am. Chem. Soc.* **128**, 11471-11474 (2006).

10. Wang, X., Ullrich, R., Hofrichter, M. & Groves, J. T. Heme-thiolate ferryl of aromatic peroxygenase is basic and reactive. *Proc. Natl. Acad. Sci. U. S. A.* **112**, 3686–91 (2015).

11. Stone, K. L., Behan, R. K. & Green, M. T. Resonance Raman Spectroscopy of Chloroperoxidase Compound II Provides Direct Evidence for the Existence of an Iron(IV)-hydroxide. *Proc. Natl. Acad. Sci. U. S. A.* **103**, 12307–12310 (2006).

12. Sacramento, J. J. D. & Goldberg, D. P. Factors Affecting Hydrogen Atom Transfer Reactivity of Metal-Oxo Porphyrinoid Complexes. *Acc. Chem. Res.* **51**, 2641–2652 (2018).

13. Prokop, K. A., de Visser, S. P. & Goldberg, D. P. Unprecedented Rate Enhancements of Hydrogen-Atom Transfer to a Manganese(V)-Oxo Corrolazine Complex. *Angew. Chemie Int. Ed.* **49**, 5091–5095 (2010).

14. Gardner, K. A. & Mayer, J. M. Understanding C-H bond oxidations: H. and H- transfer in the oxidation of toluene by permanganate. *Science.* **269**, 1849–1851 (1995).

15. Green, M. T. Role of the axial ligand in determining the spin state of resting cytochrome P450 [7]. *J. Am. Chem. Soc.* **120**, 10772–10773 (1998).

16. Parsell, T. H., Yang, M. Y. & Borovlk, A. S. C-H bond cleavage with reductants: re-investigating the reactivity ofmonomeric Mn III/IV - Oxo complexes and the role of oxo ligandbasicity. *J. Am. Chem. Soc.* **131**, 2762–2763 (2009).

17. Donoghue, P. J. *et al.* Rapid C-H bond activation by a monocopper(III)-hydroxide complex. *J. Am. Chem. Soc.* **133**, 17602–17605 (2011).

18. Nieto, I., Ding, F., Bontchev, R. P., Wang, H. & Smith, J. M. Thermodynamics of

hydrogen atom transfer to a high-valent iron imido complex. *J. Am. Chem. Soc.* **130**, 2716–2717 (2008).

19. Sastri, C. V. *et al.* Axial ligand tuning of a nonheme iron(IV)-oxo unit for hydrogen atom abstraction. *Proc. Natl. Acad. Sci. U. S. A.* **104**, 19181–19186 (2007).

20. Bím, D., Maldonado-Domínguez, M., Rulísek, L. & Srnec, M. Beyond the classical thermodynamic contributions to hydrogen atom abstraction reactivity. *Proc. Natl. Acad. Sci. U. S. A.* **115**, E10287–E10294 (2018).

21. Xue, G., De Hont, R., Münck, E. & Que, L. Million-fold activation of the [Fe2 (μ-O)2 ] diamond core for C-H bond cleavage. *Nat. Chem.* **2**, 400–405 (2010).

22. Darcy, J. W., Koronkiewicz, B., Parada, G. A. & Mayer, J. M. A Continuum of Proton-Coupled Electron Transfer Reactivity. *Acc. Chem. Res.* **51**, 2391–2399 (2018).

23. Dunford, H. B. & Dunford, H. B. *Peroxidases and catalases : biochemistry, biophysics, biotechnology, and physiology*. (John Wiley & Sons, 2010).

24. Behan, R. K. & Green, M. T. On the status of ferryl protonation. *J. Inorg. Biochem.* **100**, 448–459 (2006).

25. Sitter, A. J., Reczek, C. M. & Terner, J. Heme-linked Ionization of Horseradish Peroxidase Compound II Monitored by the Resonance Raman Fe(IV)=O stretching vibration. *J. Biol. Chem.* **260**, 7515–22 (1985).

26. Yosca, T. H. *et al.* Setting an Upper Limit on the Myoglobin Iron(IV)Hydroxide p K. *Jacs* **136**, 9124–9131 (2014).

27. Kwon, H. *et al.* Direct visualization of a Fe(IV)-OH intermediate in a heme enzyme. *Nat. Commun.* **7**, 13445 (2016).

28. Green, M. T. Application of Badger's rule to heme and non-heme iron-oxygen bonds: An examination of ferryl protonation states. *J. Am. Chem. Soc.* **128**, 1902–1906 (2006).

29. Nilsson, K., Hersleth, H. P., Rod, T. H., Andersson, K. K. & Ryde, U. The Protonation Status of Compound II in Myoglobin, Studied by a Combination of Experimental Data and Quantum Chemical Calculations: Quantum Refinement. *Biophys. J.* **87**, 3437–3447 (2004).

30. Berglund, G. I. *et al.* The catalytic pathway of horseradish peroxidase at high resolution. *Nature* **417**, 463–468 (2002).

31. Hersleth, H. P., Dalhus, B., Görbitz, C. H. & Andersson, K. K. An Iron Hydroxide Moiety in the 1.35 Å Resolution Structure of Hydrogen Peroxide Derived Myoglobin Compound II at pH 5.2. *J. Biol. Inorg. Chem.* **7**, 299–304 (2002).

32. Bonagura, C. A. *et al.* High-resolution crystal structures and spectroscopy of native and Compound I cytochrome c peroxidase. *Biochemistry* **42**, 5600–5608 (2003).

33. Kwon, H., Langan, P. S., Coates, L., Raven, E. L. & Moody, P. C. E. The rise of neutron cryo-crystallography. *Acta Crystallogr. Sect. D Struct. Biol.* **74**, 792–799 (2018).

34. Meharenna, Y. T., Doukov, T., Li, H., Soltis, S. M. & Poulos, T. L. Crystallographic and Single-Crystal Spectral Analysis of the Peroxidase Ferryl Intermediate. *Biochemistry* **49**, 2984–2986 (2010).

35. Chreifi, G. *et al.* Crystal structure of the pristine peroxidase ferryl center and its relevance

to proton-coupled electron transfer. *Proc. Natl. Acad. Sci. U. S. A.* **113**, 1226–31 (2016).

36. Moody, P. C. E. & Raven, E. L. The Nature and Reactivity of Ferryl Heme in Compounds i and II. *Acc. Chem. Res.* **51**, 427–435 (2018).

37. Gumiero, A., Metcalfe, C. L., Pearson, A. R., Raven, E. L. & Moody, P. C. E. Nature of the Ferryl Heme in Compounds I and II. *J. Biol. Chem.* **286**, 1260–8 (2011).

38. O'Dell, W. B., Bodenheimer, A. M. & Meilleur, F. Neutron protein crystallography: A complementary tool for locating hydrogens in proteins. *Arch. Biochem. Biophys.* **602**, 48–60 (2016).

39. Mittler, R. & Zilinskas, B. A. Purification and characterization of pea cytosolic ascorbate peroxidase. *Plant Physiol.* **97**, 962–8 (1991).

40. Lad, L., Mewies, M. & Raven, E. L. Substrate binding and catalytic mechanism in ascorbate peroxidase: Evidence for two ascorbate binding sites. *Biochemistry* **41**, 13774–13781 (2002).

41. Houseman, A. L. P., Doan, P. E., Goodin, D. B. & Hoffman, B. M. Comprehensive Explanation of the Anomalous EPR Spectra of Wild-Type and Mutant Cytochrome c Peroxidase Compound ES. *Biochemistry* **32**, 4430–4443 (1993).

42. Ho PS, Hoffman BM, Kang CH & Margoliash E. Control of the Transfer of Oxidizing Equivalents between Heme Iron and Free Radical Site in Yeast Cytochrome c Peroxidase*. *J Biol Chem.* **258**, 4356–4363 (1983).

43. Schünemann, V. *et al.* Mössbauer- and EPR-Snapshots of an enzymatic reaction: The cytochrome P450 reaction cycle. *Hyperfine Interact.* **156**–**157**, 247–256 (2004).

44. Coulson, A. F., Erman, J. E. & Yonetani, T. Studies on Cytochrome c Peroxidase. XVII. Stoichiometry and Mechanism of the Reaction of Compound ES with donors. *J. Biol. Chem.* **246**, 917–924 (1971).

45. Stone, K. L., Hoffart, L. M., Behan, R. K., Krebs, C. & Green, M. T. Evidence for Two Ferryl Species in Chloroperoxidase Compound II. *J. Am. Chem. Soc.* **128**, 6147–6153 (2006).

46. Penner-Hahn, J. E. *et al.* Structural Characterization of Horseradish Peroxidase Using EXAFS Spectroscopy. Evidence for Fe = O Ligation in Compounds I and II. *J. Am. Chem. Soc.* **108**, 7819–7825 (1986).

47. Hiner, A. N. P. *et al.* Detection of a tryptophan radical in the reaction of ascorbate peroxidase with hydrogen peroxide. *Eur. J. Biochem.* **268**, 3091–3098 (2001).

48. Patterson, W. R., Poulos, T. L. & Goodin, D. B. Identification of a Porphyrin π Cation Radical in Ascorbate Peroxidase Compound I. *Biochemistry* **34**, 4342–4345 (1995).

49. Shulman, G. R., Yafet, Y., Eisenberger, P. & Blumberg, W. E. Observations and Interpretation of X-ray Absorption Edges in Iron Compounds and Proteins. *Proc. Natl. Acad. Sci. U. S. A.* **73**, 1384–1388 (1976).

50. Ankudinov, A. & Ravel, B. Real-Space Multiple-Scattering Calculation and Interpretation of X-ray-Absorption Near-Edge Structure. *Phys. Rev. B - Condens. Matter Mater. Phys.* **58**, 7565–7576 (1998).

# Chapter III: The Ferric-Hydroxide Form of Ascorbate Peroxidase

## Introduction: Photoreduction of ferryl intermediates:

Central to the debate around ligand assignment in high valent heme intermediates is the issue of only using structural data for these assignments. The difficulty of solely using X-ray diffraction data to make a protonation state assignment comes from the simple fact that hydrogen atoms have only one electron, making them very hard to observe with X-ray scattering because of the lack of electron density.[1] Instead, in X-ray crystallography ferryl protonation must be indirectly observed through examining the Fe-O bond length, as the Fe-O bond length increases upon protonation of the oxygen coinciding with a change in the Fe-O bond order. To make the hundredths of an Ångstrom determinations necessary for this indirect protonation state assignment, one needs high quality electron density maps at high resolution. Very high resolution X-ray crystal structures from the early 2000s of high valent heme iron enzymes were praised as the most accurate description of these intermediates, but the Fe-O bond distances that were obtained were longer than expected and disagreed with spectroscopic assignment of oxo ligands.[2–5] There were reports of long Fe-O bonds which researchers concluded was a sign of an Fe(IV)-OH species.

It was soon realized that these experiments did not reflect genuine ferryl intermediates. An application of Badger's rule, an empirical formula linking stretching frequency to interatomic bond distances, had demonstrated that it is specifically the X-ray crystallography measurements that do not fit in with the trend of heme and non-heme iron-oxygen distances (if both the ferryl oxidation state and long Fe-O bonds were both true).[6] Badger's rule was first parameterized upon a set of structures and density functional theory to calculate $r_e$ and $\nu_e$ for Fe-O bonds across a series of heme and non-heme iron complexes with different axial ligands, oxidation states, oxygen protonation states, and spin states, as a generalization across Fe-O bonds. By comparing bond distances from reported Fe(IV)-OH species that used structural methods to the complete series of calculated Fe-O bonds, it was clear that the Fe-O bonds from the structures were longer than would be expected for a genuine Fe(IV)-OH species and do not fit the linear trend for Fe-O bonds. This was not the case for the spectroscopic measurements for the same systems, which showed short Fe-O bonds consistent with iron(IV) oxos.

An immediate understanding of what was happening was not clear, but a quantum refinement study of earlier gathered myoglobin Compound II data concluded that the electron density maps equally fit models for Fe(III)-OH and Fe(IV)-OH.[7] According to the parameterized Badger's rule for Fe-O bonds, the distance  from the myoglobin structure clearly represented a Fe(III)-OH species. A strong case for photoreduction of the crystal to the ferric state was developing.

To focus upon a single system: In 2003, Bonagura et al published a report of the 1.2 Å high-resolution crystal structure and spectroscopy of native cytochrome C peroxidase Compound ES (CcP-ES).[4] In this study, the authors established that the X-ray dosing the CcP-ES crystal diminished the signal of the protein radical in CcP-ES and cited no sign of ferric enzyme accumulating in the EPR spectrum, yet the X-ray crystal structure yields a long Fe-O bond of 1.87 Å. A follow-up study on a mutant of CcP that formed better-diffracting crystals revealed that the Fe-O bond was lengthening as a function of X-ray dosage during an X-ray crystallography experiment, and by producing merged data sets of multiple crystal structures of limited dosages, it was possible to yield short Fe-O distances for CcP, pointing to a linear trend of 0.2543 A per megagray (MGy) and a proposed genuine Fe-O bond distance of 1.72 Å.[8]

This experiment was successful because the authors were able to use a microspectrophotometer to observe the Q-bands for characteristic signs of oxidation state changes, establishing dosage limits before the CcP-ES signatures went away. Effectively, this allowed the oxidation state of the crystal to be observed. Finally, in 2016, a Free Electron Laser study by the same authors revealed in a single pristine crystal a short Fe-O bond of 1.7 Å.[9] For CcP, the photoreduction problem could be circumvented by this multi-crystal approach, and the free electron laser method worked to show a structure of a pristine Fe(IV).

The multi-crystal approach utilized in the 2016 report by Kwon et al. to complement the neutron crystal structure is an application of the same methodology that had been used five years prior.[10,11] The 2011 paper, *Nature of the Ferryl Heme,* investigated both CcP and ascorbate peroxidase (APX) through a multi-crystal approach.[11] In both systems, the ferryl intermediate was made by soaking with oxidant to form CcP-ES and APX-II. Crystals were frozen after a color change corresponding to intermediate formation, and these were then examined through an on-line spectrophotometer at the European Synchrotron Radiation Facility (ESRF) to determine the X-ray dosage limits before signs of forming ferric or ferrous forms of CcP or APX. With these limits then established, a multi-crystal X-ray crystallography set of data can be collected that respects these limits and can be merged to form the full X-ray crystal structure. In CcP, this method yielded a short 1.63 Å Fe-O bond distance.[11] The authors report 1.84 Å Fe-O distance for APX-II.[11] We stress that APX-II and CcP-ES should be electronically the same.

Importantly, the 2016 paper on APX-II uses a co-refinement of X-ray and neutron data to form the final structure.[10] This uses a neutron Fo-Fc difference map data to look for the density for an -OH ligand, then X-ray data to make the finer atom refinements of the structure once the ligand model has been placed – ergo, an -OH ligand, and 1.88 Å away. The assumption here is that the X-ray structure really reflects a ferryl intermediate. The authors in 2011 report the dosage limits of 0.028 MGy for the APX-II crystals before observing signs of photoreduction. Yet only the UV/Visible spectrum for Fe(III)-OH APX was not known, while the UV/Visible features of 5-coordinate Fe(II) APX were known and avoided. How, then, were the authors to avoid signs of APX Fe(III)-OH? In the last segment of the results and discussion section of this chapter, we discuss the crystal UV/Visible absorption spectra and identifying heme species by these features.

The cryotrapped photoreduced species from CcP-ES appears to have the UV/Visible features of ferric CcP.[8] The earlier high-resolution X-ray crystal structure of CcP-ES in which photoreduction *definitely* did occur showed a long 1.87 Å which according to the parameterized Badger's rule is consistent with ferric iron.[4] Reducing from an Fe(IV)=O state would leave a negative charge on the oxygen atom that would protonate with the solvent, producing an Fe(III)-OH species. We believe this stands to reason as a good candidate for what the X-ray crystal structures for APX-II reported in 2011 and 2016.[10,11]

For this reason, it is important to understand the Fe(III)-OH form of APX as a standard to better understand reports of protonated ferryls in histidine-ligated heme enzymes. While we cannot say definitively how the deuterated crystal that produced the neutron crystal structure was handled, we can explain how the results are consistent with a photoreduced species. What follows is our report of the Fe(III)-OH form of APX, and our highly speculative reinterpretation of published data in this new light.

## Experimental Methods:

### Expression and Purification of ascorbate peroxidase:

Ascorbate peroxidase was cloned, expressed, and purified as described in the previous chapter.

### UV/Visible spectroscopy:

Ferric APX (20 µM) in 10 mM sodium bicarbonate buffer pH 10 was pH-jumped 1:1 with a strong 200 mM sodium bicarbonate / 200 mM potassium bicarbonate pH 12 buffer. Spectra were obtained at t = 0 and t = 1 s. Ferric-OH CcP was prepared similarly for UV/Visible spectroscopy, at t = 25 ms, starting instead with a 10 mM sodium bicarbonate buffer at pH 5.8.

### Preparation of Samples:

Freeze-quenched APX was prepared by putting ferric APX in a weak 10 mM pH 10 sodium bicarbonate buffer and pH jumping that with a pH 12 200 mM sodium bicarbonate / 200 mM potassium phosphate buffer in a rapid 1:1 mix, aged just 3 ms before spraying into liquid ethane.

### Electron Paramagnetic Resonance:

Experiments were performed at 10 K with 2 mM power using Bruker EMX EPR spectrometer operating in X-band (9-10 GHz) with an Oxford ESR900 helium cryostat.

### Mössbauer spectroscopy:

Data were collected using a spectrometer from WEB research in constant acceleration mode using transmission geometry and a 50 mT magnetic field applied parallel to the γ-beam. Spectra were recorded at 4.2 K using a Janis SVT400 cryostat. Isomer shifts were calibrated using the centroid of the spectrum of a foil of α-Fe at room temperature. Data analyses were performed using the program WMOSS from WEB research.

### X-ray Absorption Spectroscopy (XAS):

XAS data were collected in fluorescence mode at 10 K with a 30-element germanium detector (SSRL, BL7-3) using a Si(220) Phi = 0° double monochromator with a 9.5 keV cutoff for harmonic rejection. Mounted samples were moved in the beam after each scan to an unexposed region of the sample to minimize the effect of photoreduction. Twenty-two first scans were included in the Ferric-OH APX EXAFS data set. Fitting of EXAFS and pre-edge data were performed using EXAFSPAK.

### Spectra Digitizing:

Engauge Digitizer for Windows[12] was used to recover data points from graphs by placing individual points along an imported image of published data. Raw data were replicated by individually selecting data points by mouse over an established coordinate system that matches the X/Y axes.

## Results and Discussion:

The UV/Visible spectrum of APX$^{III}$-OH was difficult to obtain because of the pH limits of stability for ascorbate peroxidase. This was circumvented by using rapid-mixing techniques and capturing the spectrum of the species before it decayed. This was performed by buffer-jumping: APX at 20 μM was brought into a weak 10 mM sodium bicarbonate buffer at pH 10 and rapidly mixed 1:1 with a strong 200 mM sodium bicarbonate / 200 mM potassium bicarbonate buffer at pH 12, resulting in a final solution pH of 12 and a brief spectrum of ascorbate peroxidase Fe(III)-OH, shown in Figure 3.1. Ferric-OH, APX displays a Soret band at 414 nm and Q-bands at 540 and 577 nm. This is consistent with the 540 and 570 Q-bands that have been reported for horseradish peroxidase Fe(III)-OH.[13]

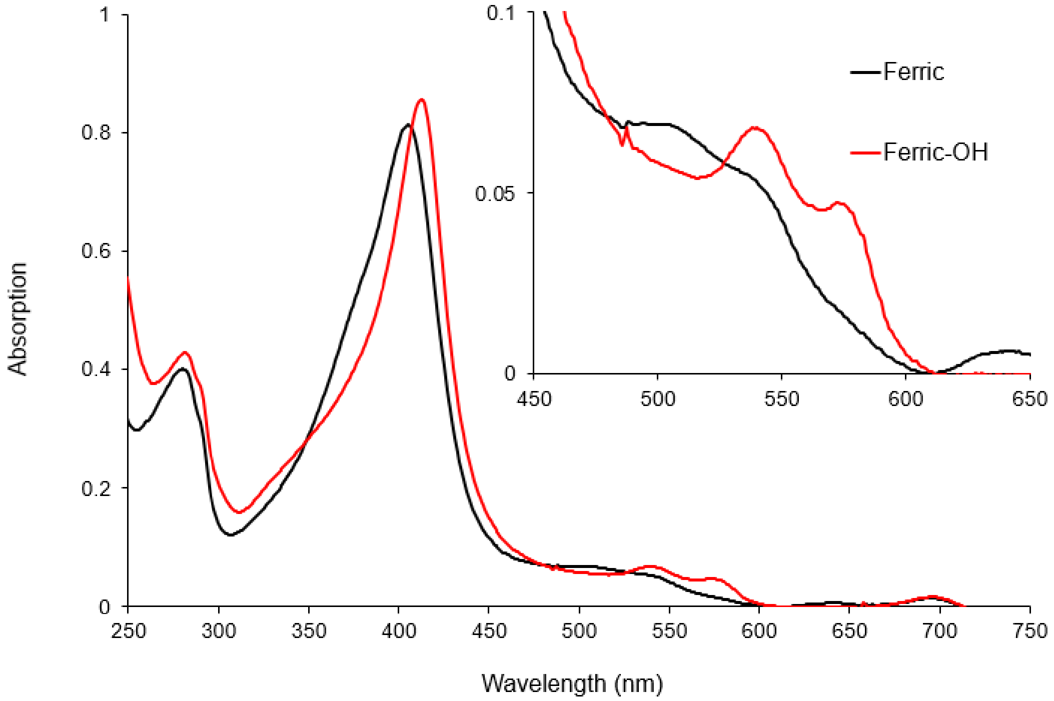

**Figure 3.1**: Stopped-flow UV/visible spectra at t=0 (black) and t=1 s (red) at 4 °C. APX Fe(III)-OH is not stable at pH 12 and the Soret rapidly bleaches as protein aggregates form and the solution becomes turbid. Fe(III)-OH APX can be stabilized by rapidly freezing. It is stable at -80°C.

For the purposes of scaling up the reaction for a battery of spectroscopic experiments at higher concentrations, electron paramagnetic resonance was chosen as the initial screening technique. This is because of the fast time it takes to produce an EPR spectrum relative to Mössbauer, and because low- and high-spin states of ferric heme enzymes have been extensively characterized and are easily discernible from each other. Producing a Fe(III)-OH species forms a low spin Fe(III), in which the single unpaired electron produces a characteristic rhombic splitting pattern.

Freeze-quenched APX was prepared by putting ferric APX at 6 mM in a weak 10 mM pH 10 sodium bicarbonate buffer and pH jumping that up to 12 with a pH 12 200 mM sodium bicarbonate / 200 mM potassium phosphate buffer in a rapid 1:1 mix and aged for 3 ms before spraying into liquid ethane. Figure 3.2 shows EPR spectra of this reaction. EPR spectra demonstrate that it is a low spin ferric heme system, with g values of 2.55, 2.2 and 1.78 consistent with a rhombic environment. The signal at 1.98 is from remaining ferric protein in the sample. Figure 3.3 shows the spectrum of ferric APX as a mixture of high- and low-spin states at 10 K, and predominantly high-spin.

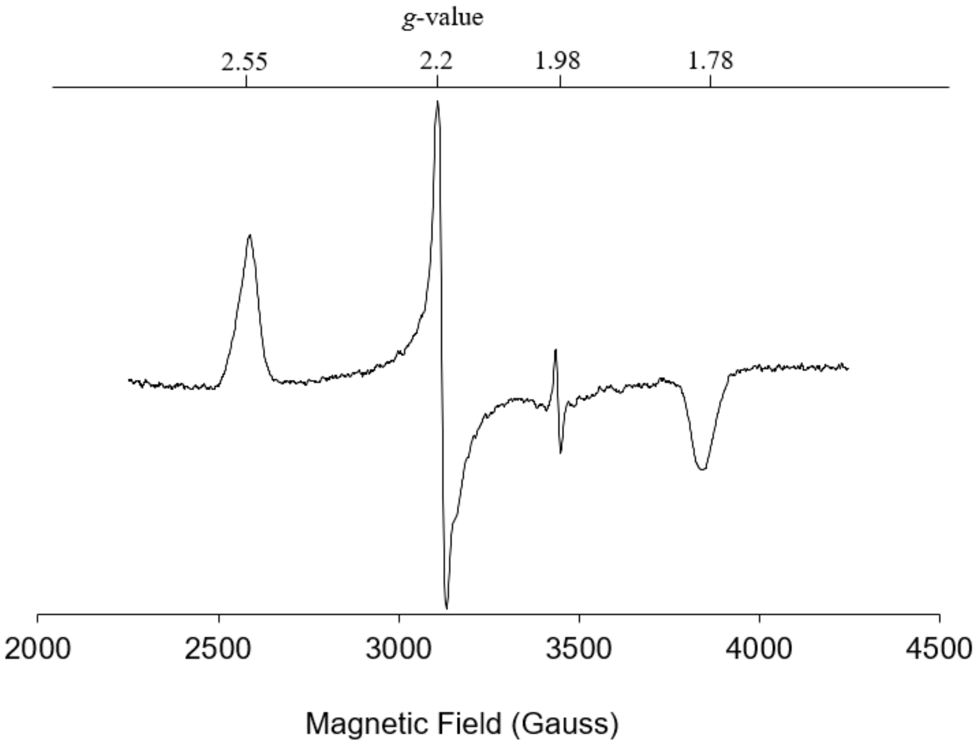

**Figure 3.2**: Electron Paramagnetic Resonance spectrum of Fe(III)-OH APX at 10 K. G-values 2.55, 2.2, and 1.78 are consistent for a low-spin ferric heme in a rhombic environment. Signal at 1.98 is from remaining ferric enzyme. Microwave power : 2 mW, modulation amplitude: 10.0 G.

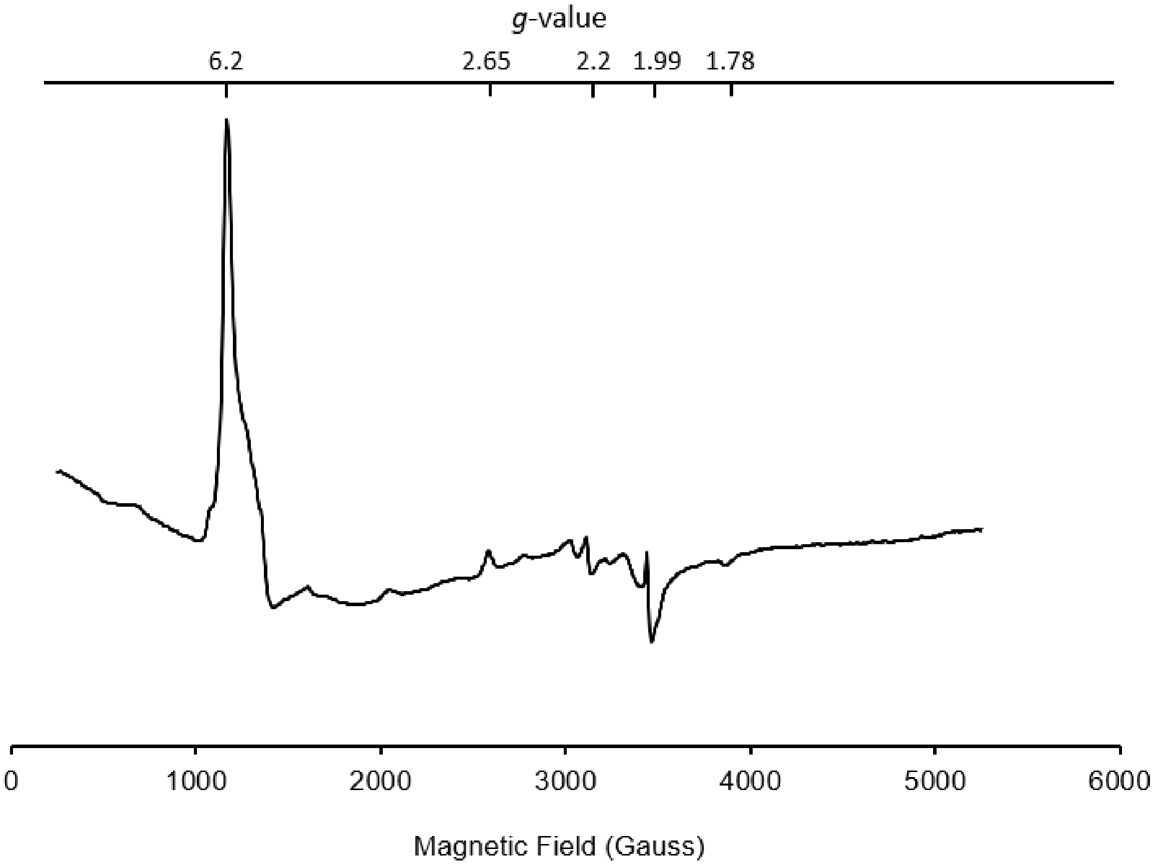

**Figure 3.3**: EPR spectrum of ferric APX at 10 K. It is mostly high-spin, S = 5/2. Microwave power: 2 mW, modulation amplitude: 10.0 G.

Figure 3.4 shows the same sample reaction examined through Mössbauer spectroscopy. Fitting was performed using g-values through EPR of the same reaction (Figure 3.2), yielding fitting parameters: $\Delta E_Q = -2.674$, $\delta = 0.228$. The magnetic hyperfine tensor for the fit is [33.1168, -7.4809, 43.3794 T]. Fitting assumed a single unpaired electron model in an orthorhombic symmetry. We would like to note that it bears a striking resemblance to the iron(III) hydroxide form of myoglobin.[14]

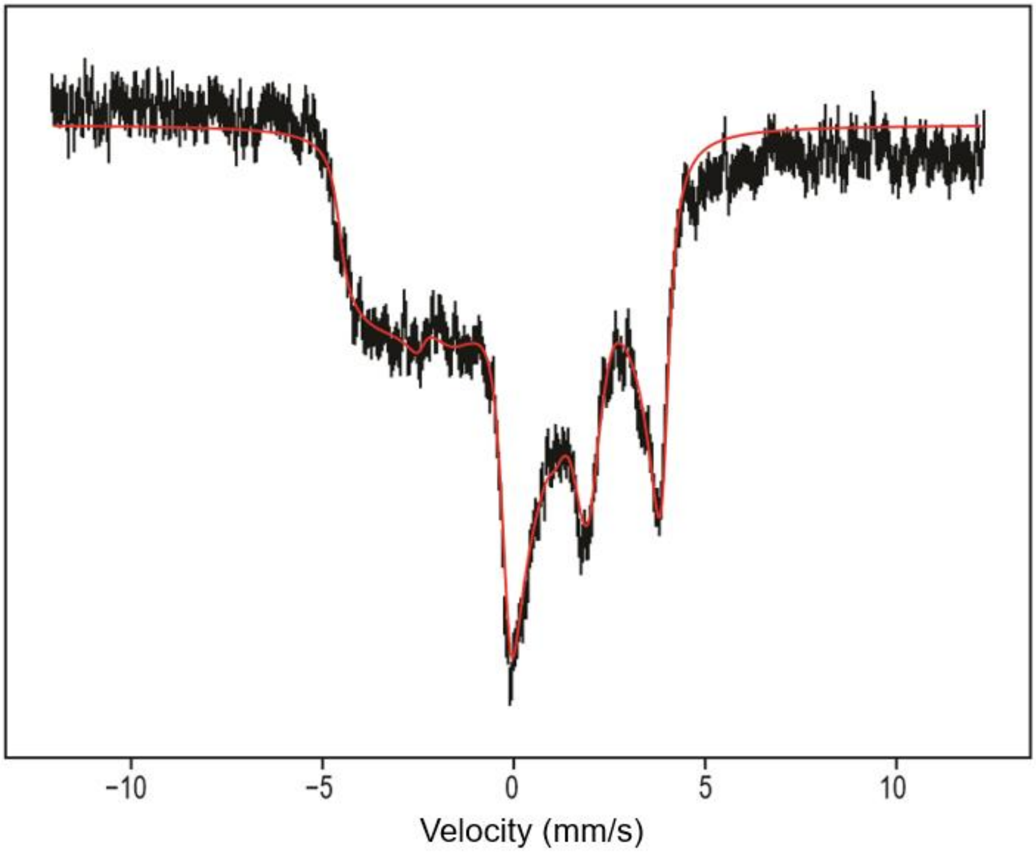

**Figure 3.4**: Mössbauer spectrum of Fe(III)-OH of APX. This is the same reaction as Figure 3.2, 3.5, and 3.6. Raw data are shown in black, and the fit is shown in red.

Figure 3.5 shows the raw and Fourier-transformed (FT) EXAFS data for the ferric-hydroxide form of APX. Fitting of the data is presented in red, and raw data are in black. The spectrum is comprised of 39 first scans. The first shell was modeled with two different components; the oxygen ligand was a separate component from the five nitrogen ligands (one from the proximal ligand and four from the porphyrin) and allowed to vary its length independently from the Fe-N bonds. The second shell describes the heme macrocycle's 8 α carbons, 4 meso carbons, and 16 Fe-Cα-N multiple scattering paths. Fitting was performed with the program EXAFSPAK using phases and amplitudes generated using FEFF 8.x39.[15]

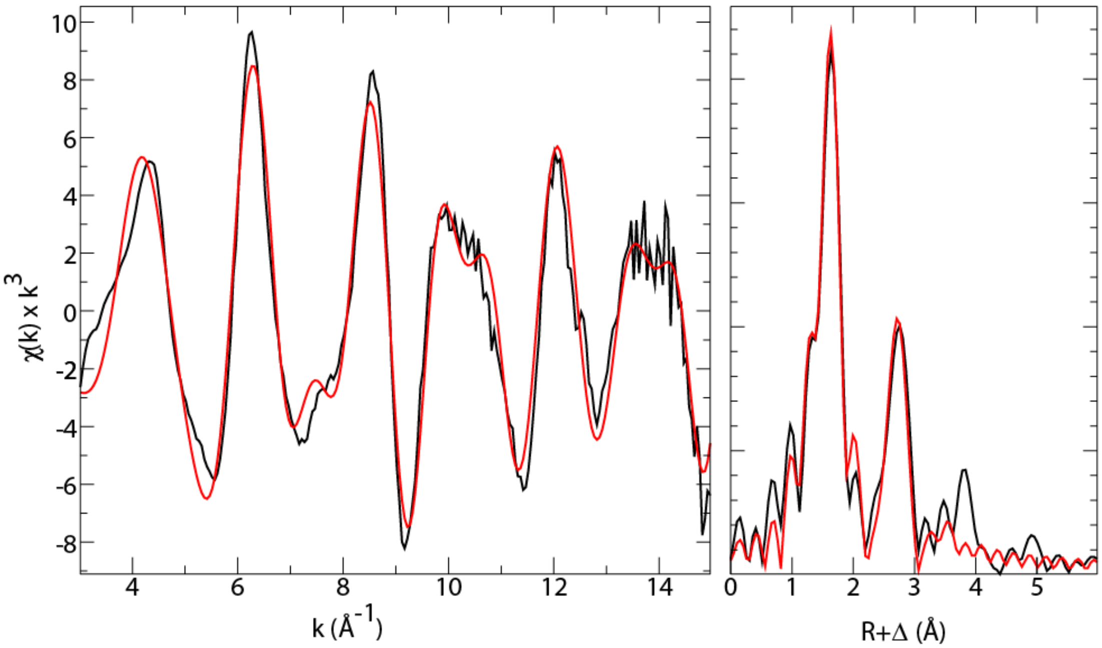

**Figure 3.5**: EXAFS of the Fe(III)-OH species (left) and Fourier transform (right). Black lines show experimental data. Red lines show fitting results. Shown are the data for the 5 Fe-N 1 Fe-O, 4,3 model of Table 3.1.

The EXAFS data in Figure 3.5 were produced using a spline of order 4 with 3 ranges. The EXAFS data shown for APX-II in the prior chapter uses a spline or order 4 with 4 ranges, which we will call here a 4,4 spline. A 4,4 spline is typical for what we use when processing XAS data for heme proteins. In fitting the EXAFS data, we observed that  a 4,3 spline was required to fit a Ferric-OH. What follows next is our discussion on why the 4,3 model is applicable here, and how the data suggest a hydroxide ligand assignment. Comparison between the splines in the X-ray absorption spectrum in the EXAFS region is in supplemental Figure 3.1.

Figure 3.6 shows a comparison of the EXAFS data for Ferric-OH APX and ferric 5-coordinate (resting state) APX, between the 4,3 and 4,4 splines. In both cases, there is only a minor difference between the Ferric-OH and ferric 5-coordinate spectra. There is a pronounced difference between the spectra with the 4,3 spline in the $k$ = 13-15 region, compared to the 4,4 spline. When the data are fit, however, the influence of these subtle changes are clear: Table 3.1 shows fitting results for multiple models between the two splines.

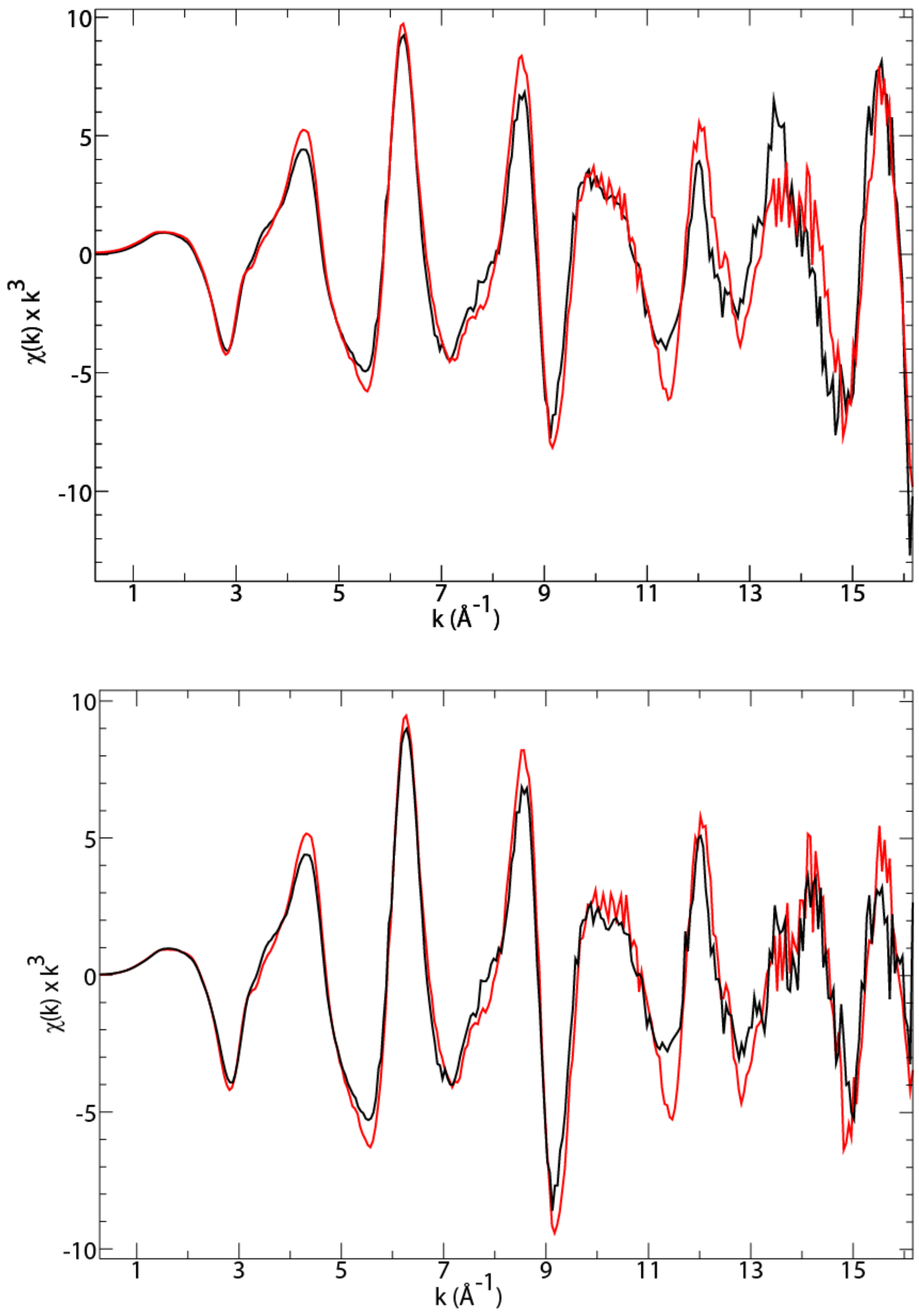

**Figure 3.6**: Comparing Fe(III)-OH APX to ferric 5-coordinate APX with 4,4 and 4,3 splines. (Top): 4,3 spline. (Bottom): 4,4 spline. Fe(III)-OH APX is in red, ferric 5-coordinate APX is in black.

**Table 3.1:** EXAFS Fitting Results for Raw APX Fe(III)-OH and Ferric 5-coordinate Data[a]

| | Fe-N | | | Fe-O | | | Fe-$C_\alpha$ | | | Fe-N- $C_\alpha$ | | | Fe-$C_{meso}$ | | | | |
|---|---|---|---|---|---|---|---|---|---|---|---|---|---|---|---|---|---|
| | N | R | $\sigma^2$ | N | R | $\sigma^2$ | N | R | $\sigma^2$ | N | R | $\sigma^2$ | N | R | $\sigma^2$ | $E_0$ | error[b] |
| pH 12 | 6 | 1.98 | 0.002 | | | | 8 | 3.04 | 0.009 | 16 | 3.13 | 0.001 | 4 | 3.40 | 0.001 | -13 | 0.253 |
| 4,4 spline | 5 | 1.98 | 0.002 | | | | 8 | 3.04 | 0.001 | 16 | 3.15 | 0.002 | 4 | 4.31 | 0.001 | -13 | 0.257 |
| | N | R | $\sigma^2$ | N | R | $\sigma^2$ | N | R | $\sigma^2$ | N | R | $\sigma^2$ | N | R | $\sigma^2$ | $E_0$ | error[b] |
| pH 12 | 5 | 1.99 | 0.001 | 1 | 1.86 | 0.001 | 8 | 3.03 | 0.001 | 16 | 3.16 | 0.002 | 4 | 3.43. | 0.002 | -15 | 0.260 |
| 4,3 spline | 5 | 1.98 | 0.001 | | | | 8 | 3.03 | 0.001 | 16 | 3.15 | 0.002 | 4 | 3.40 | 0.001 | -15 | 0.289 |
| | 6 | 1.98 | 0.002 | | | | 8 | 3.03 | 0.001 | 16 | 3.14 | 0.002 | 4 | 3.40 | 0.002 | -15 | 0.290 |
| | N | R | $\sigma^2$ | N | R | $\sigma^2$ | N | R | $\sigma^2$ | N | R | $\sigma^2$ | N | R | $\sigma^2$ | $E_0$ | error[b] |
| pH 7 | 5 | 2.01 | 0.002 | | | | 8 | 3.06 | 0.002 | 16 | 3.14 | 0.003 | 4 | 3.43 | 0.001 | -10 | 0.411 |
| 4,3 spline | 6 | 2.01 | 0.002 | | | | 8 | 3.05 | 0.001 | 16 | 3.07 | 0.002 | 4 | 3.43 | 0.002 | -10 | 0.428 |

[a] Data were fit over the region $k = 3–15$ Å$^{-1}$. Coordination number *N*, interatomic distance *R* (Å), mean square deviation in *R* (the Debye–Waller factor), $\sigma^2$ (Å$^2$), and the threshold energy shift $E_0$ (eV).

[b] The fit errors listed for the raw data come from the weighted *F* factor which is defined as $[\Sigma k^6(\chi_{exptl} - \chi_{calcd})^2/\Sigma k^6 \chi^2_{exptl}]^{1/2}$.

Using the 4,4 spline with the Fe(III)-OH data presents a fitting challenge, where a modeled in (starting) 1.88 Å Fe-O bond would lengthen to ~ 2 Å, indistinguishable from the Fe-N components and the 6 Fe-N model. The 4,4 splined data fit best with 6 elements to the primary coordination sphere, all 1.98 Å away, and decreasing this to 5 Fe-N bonds results in a larger fitting error. The 4,3 splined data however can distinguish a 1.86 Å Fe-O bond from the Fe-N bonds, and this model has the lowest error compared to alternative models. Comparing this to resting state 5-

coordinate ferric enzyme (pH 7), where attempts to model in an Fe-O bond result in this bond lengthening – but here, 5 Fe-N bonds produces the lowest error, consistent with 5-coordinate ferric heme. With the 4,3 spline, Fe(III)-OH APX fits a 1.86 Å Fe-O bond, which cannot be modeled onto the resting state ferric data. This 1.86 Å Fe-O distance is only 0.02 Å away from the 1.88 Å reported by the joint X-ray/neutron crystallography report.[10]

The resolution limits for EXAFS data analysis are influenced by the range in *k*-space used for the FT via the Rayleigh criterion. Over the 3-15 range, the resolution limit in *R*-space is $\pi / (2\Delta k)$, or 0.13 Å. Specifically, resolution in this context means the ability to distinguish two bonds from each other. The 1.86 Å Fe-O bond is 0.13 Å away from the 1.99 Å Fe-N bonds. The Rayleigh criterion establishes the minimum parameters at which two features can be distinguished, here the precision of distinguishing similar bonds. Sitting at the 0.13 Å limit means the 1.86 Å Fe-O bond *can* be distinguished from the longer Fe-N bonds.

Re-examination of published data:

For the second half of this chapter, we will be focusing our discussion on the published data discussed earlier. Figure 3.7 is a reproduction of the data from the 2011 paper, *Nature of the Ferryl Heme in Compounds I and II*.[11] This figure details the X-ray crystal's Q-bands on the on-line UV/Visible spectrophotometer, showing the crystal before the X-ray dose (solid line) and after 0.3 MGy X-ray dose (dotted line). The authors argue that at 0.3 MGy, it is clear that APX has reduced to the ferrous state – this is easy to tell from the appearance of features at 555 and 583 nm, which are consistent with ferrous APX. We would like to draw the reader's attention to the black labels in Figure 3.7, corresponding to the UV/Visible Q-band maxima observed in Figure

3.1 for APX(III)-OH. We believe there are traces of the ferric-OH spectrum in both of the spectra shown. In the X-ray dosed spectrum, it makes sense that ferric-OH APX would be trapped and mixed with some ferrous-OH APX as APX-II is reduced from Fe(IV) → Fe(III) → Fe(II). However, the origin for the features in the before X-ray UV/Visible spectrum are mysterious. The authors report limiting X-ray exposure on the individual crystals in the multi-crystal APX-II experiment to 0.028 MGy (less than one tenth of the ferrous crystal spectrum shown in Figure 3.7), but they do not provide any experimental evidence of what that small X-ray dosage does to the ferryl crystal. If APX-II was more sensitive to photoreduction, this approach would not necessarily circumvent the problem as intended.

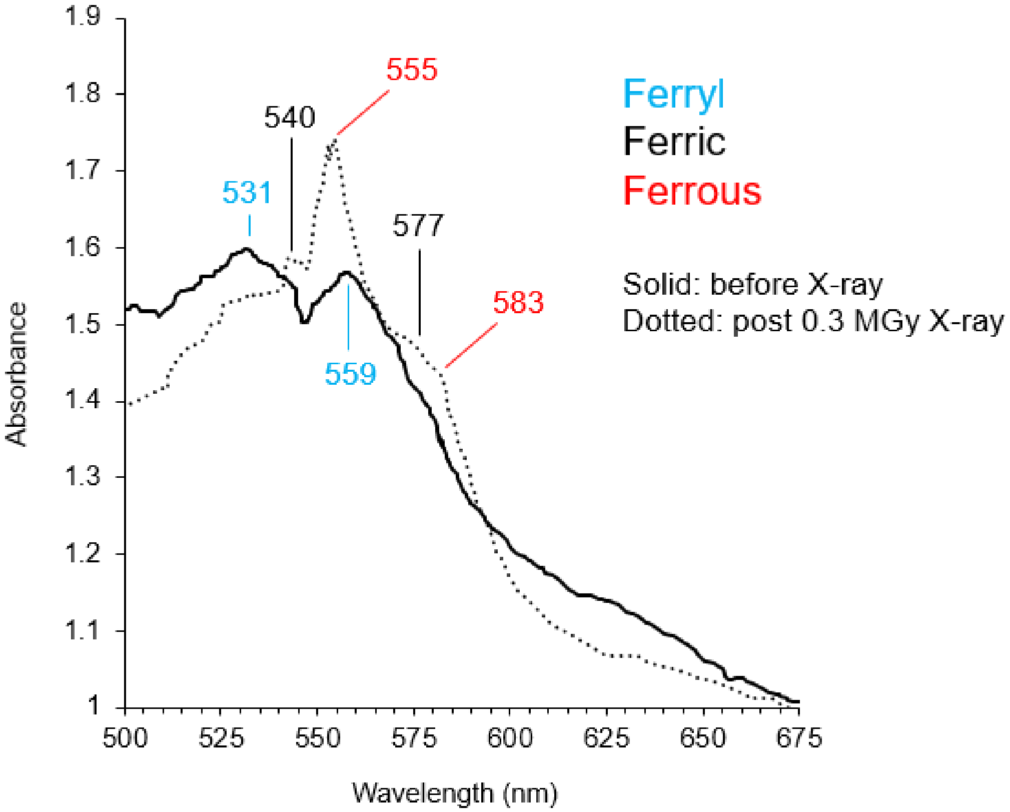

**Figure 3.7**: A reproduction of Figure 2B from *Nature of the Ferryl Heme in Compounds I and II* (2011). The figure describes UV/Visible data from an on-line spectrophotometer, displaying the Q-bands of APX crystals. The solid line is the spectrum of a single crystal before X-ray exposure, and the dotted line is after a 0.3 MGy X-ray dose. Labels for ferryl and ferrous APX come from the referenced publication. The features labeled for ferric APX (in black) are from this text.

Figure 3.8 shows the solid-line spectrum of the unexposed (0 MGy) APX-II crystal shown in Figure 3.7 compared to a simulated UV/Visible spectrum made from the solution spectra of Ferric-OH APX and APX-II. In order to match the Q-band maxima reported in the 2011 publication for APX-II (531 and 559 nm), it was necessary to include 47% Ferric-OH contribution in the simulation. We suggest that this provides evidence that the crystal, even without any exposure to the X-ray beam, was not a pure crystal of APX-II. The crystal displayed Q-band traces indicating that it is approximately 47% Ferric-OH.

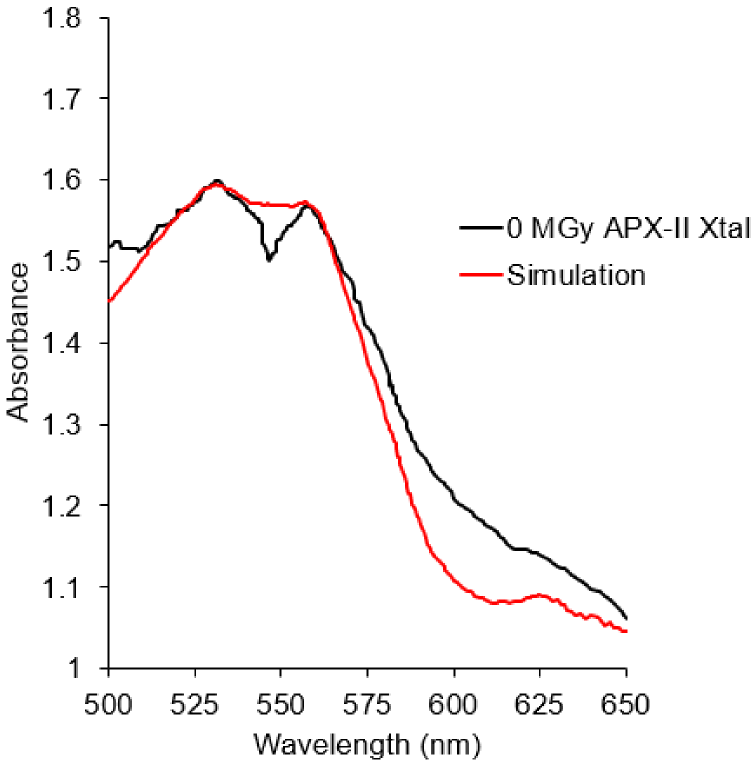

**Figure 3.8**: Reproduction of Figure 2B from *Nature of the Ferryl Heme in Compounds I and II* (2011). Black line is the spectrum of a single crystal before X-ray exposure. The red line is a simulated UV/Visible spectrum made from the solution spectra of APX-II and Ferric-OH reported earlier in this text. Spectra were multiplied and added to each other to produce the simulation, then shifted to match the baseline from the 2011 report.

Figure 3.9 shows a similar analysis upon the second component of Figure 3.7, the 0.3 MGy dosed spectrum. It is reported that APX reduces to ferrous after this much X-ray exposure – however, this should reduce to a 6-coordiante low-spin ferrous system, an Fe(II)-OH. The simulation we show in Figure 3.9 is simply a multiplication of the 5-coordinate ferrous spectrum of APX simulation. The data support this is the sole origin of the 555 nm absorbance peak shown in Figure 3.7.

It is difficult to understand why it would be 5-coordinate ferrous showing up in the X-ray crystal. We propose one possibility is localized heating causing some annealing of the crystal and the 6-coordinate ferrous-OH form of APX losing the distal ligand as it protonates from solvent and moves to 2.3 A, becoming the water molecule reported in the crystal structure, but this 5-coordinate species should not be present without problems in the crystallography experiment. Alternatively, it is not unreasonable to speculate some annealing of the crystal during sample handling, and possible loss of the 6th coordinating ligand as a water molecule along with warming.

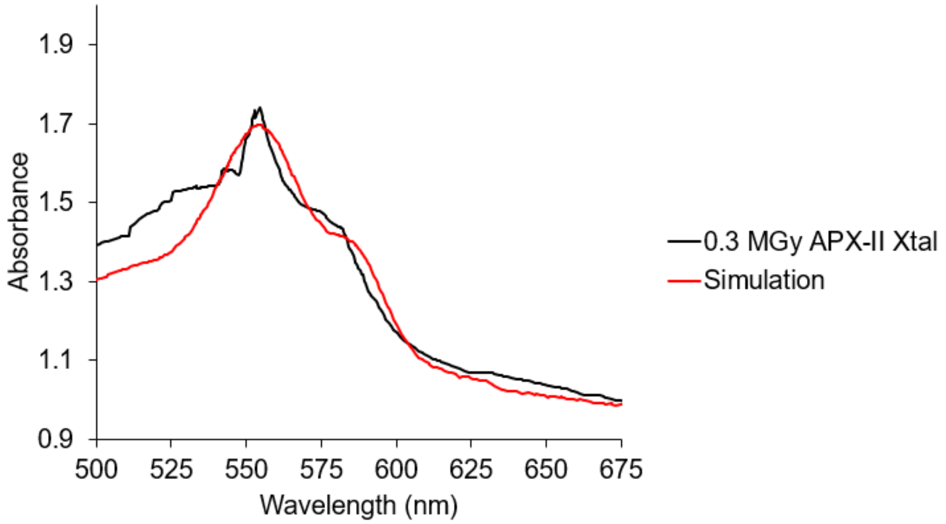

**Figure 3.9**: Reproduction of Figure 2B from *Nature of the Ferryl Heme in Compounds I and II* (2011). Black line is the spectrum of a single crystal after 0.3 MGy X-ray exposure. The red line is a simulated UV/Visible spectrum made from the solution spectra of only 5-coordinade ferrous APX. The spectrum was multiplied to scale and shifted to match the baseline from the 2011 report.

We would like to take a moment to discuss the comparison between crystal UV/Visible spectra and solution spectra: There is definitely a large background component from high protein concentrations within the crystal itself leading to a very intense absorbance, but there are also relative intensity differences in the absorption features dependent upon crystal orientation.[16] For a detailed comparison between solution and crystal spectra of the same heme system, we suggest the book *Iron Porphyrins, Part I*.[16] While the intensity of the electronic transitions change, the energy of the transitions themselves do not significantly change and comparison with solution UV/Visible absorption spectra are appropriate. To Illustrate this point, and because of the relevant photoreduction phenomena, we would like to demonstrate the simulation of pristine and X-ray reduced CcP-ES crystal UV/Visible absorption spectra in Figures 3.10 and 3.11. The X-ray crystallography data come from Meharenna et al.[8] Simulations utilize solution spectra of CcP that are presented together in Figure 3.S3.

In Figure 3.10, the pristine crystal displays UV/Visible features consistent with CcP-ES (531, 560, 630 nm). Unlike APX (as reported in 2011 and 2016), the Q-bands indicate this crystal is a single ferryl intermediate. The simulation shows only CcP-ES data (528, 560 nm), consistent with a single species in the crystal.

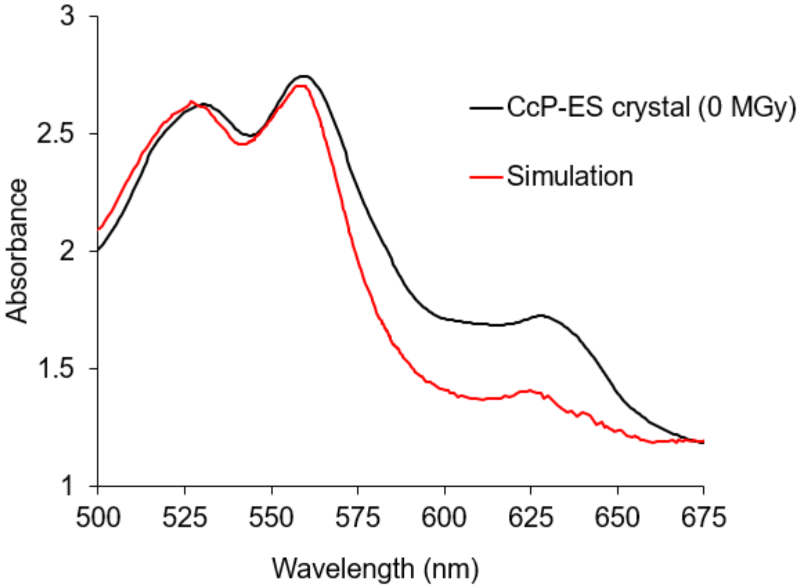

**Figure 3.10**: Reproduction of Figure 2B from *Crystallographic and Single Crystal Spectral Analysis of the Peroxidase Ferryl Intermediate* (2010). Black line is the spectrum of a single crystal without X-ray exposure. The red line is a simulated UV/Visible spectrum made from the solution spectra of only APX-II. The spectrum for CcP-ES display three features consistent with the spectrum of compound II in APX, an Fe(IV)=O system. The crystal as reported was pristine and contained no sign of Fe(III). The spectrum was multiplied to scale and shifted to match the baseline from the 2010 report.

Because of its similarity to APX, we thought to apply our pH-jumping methods to generate a Ferric-OH state in CcP. Figure 3.11 shows the stopped-flow reaction of 20 µM ferric CcP in a 10 mM sodium bicarbonate buffer at pH 5.8 was mixed 1:1 with a 200 mM sodium bicarbonate / 200 mM potassium bicarbonate buffer at pH 12. The Soret quickly bleaches in this reaction, however at 25 ms the UV/Visible spectrum changes with a Soret shift to 418.4 nm and Q-bands at 545.7 and 580.1 nm. Compare to APX, with 414, 540, and 577 nm features. Importantly, the Q-band features display the same pattern of the larger β-band and smaller α-band.

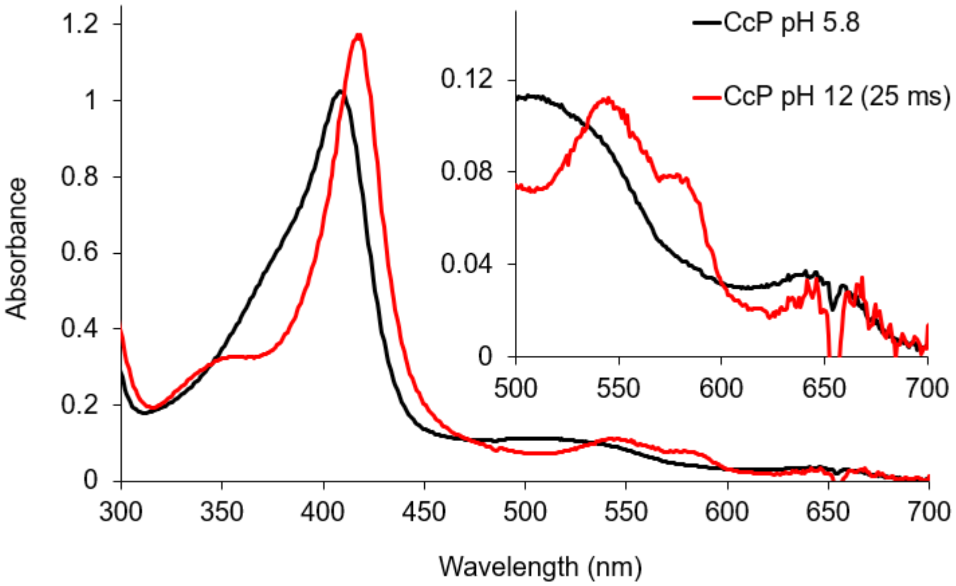

**Figure 3.11**: Stopped-flow UV/Visible spectra at t=0 (black) and t=25 ms (red) at 4 °C. CcP Fe(III)-OH is not stable at pH 12 and the Soret rapidly bleaches as protein aggregates form and the solution becomes turbid.

In Figure 3.12, we show a mixture of 53% Ferrous CcP, 29% Ferric 5-coordinate, and 15% Ferric-OH in the simulation compared to the reduced CcP-ES crystal. This simulation suggests the major component of the crystal after X-ray exposure was Ferrous, but that the crystal became a mixture and Fe(III) was still present, including a cryotrapped Ferric-OH.

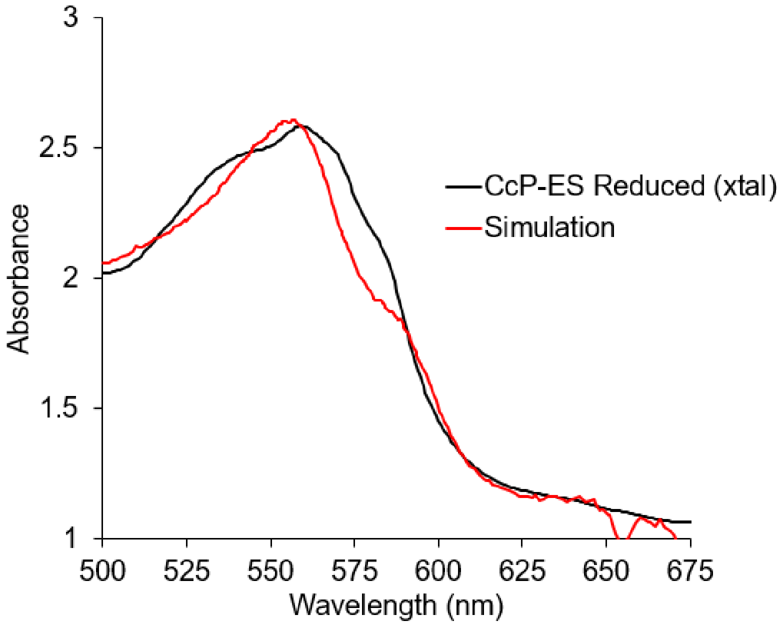

**Figure 3.12**: Reproduction of Figure 2B from *Crystallographic and Single Crystal Spectral Analysis of the Peroxidase Ferryl Intermediate* (2010). Black line is the spectrum of a single crystal after X-ray exposure. The red line is a simulated UV/Visible spectrum made from a combination of solution spectra of ferrous, ferric-hydroxide and ferric 5-coordinate CcP. Component spectra were multiplied to scale, and this was shifted to match the baseline from the 2010 report.

The use of solution UV/Visible spectra to understand crystal spectra have been demonstrated above. The data suggest, as shown by Figure 3.8, that the UV/Visible spectrum of unexposed-to-X-ray *already* shows signs of containing the reduced Fe(III)-OH species. This initial misassignment of the Fe-O bond length as 1.86 Å, and the authors' misinterpretation of their control experiments is the origin of the incorrect argument in Kwon et al (2016).[10,11] The multi-crystal X-ray crystallography method never worked for APX as the crystals were becoming reduced between 0 – 0.028 MGy, (0.028 MGy being the dosage estimated per individual crystal of APX). Limiting to 0.028 MGy was *certainly* lower than the 0.3 MGy required to produce the 5-coordinate ferrous spectrum – but our simulations suggest this was still enough to photoreduce the sample. This misassignment and faith in this technique led to the repeat and technical expansion five years later, culminating in a *Nature* paper, and contributing heavily to more recent publications such as *The Rise of Neutron Cryo-Crystallography.*[17]

Our UV/Visible spectrum of Fe(III)-OH CcP needs verification by EPR to confirm that it is a low-spin ferric heme system. Understanding this species is important in fully interpreting the structural data of reduced ferryl CcP, and it is important in how we continue to study APX and how heme peroxidases function. A more recent publication by Kwon et al. in 2021 using an X-ray free electron laser reports a 1.76 Å Fe-O distance in CcP Compound II (CcP-II), which is a form of CcP-ES where the tryptophan radical has been reduced, yielding a Fe(IV) center.[18] As CcP-ES and CcP-II are indistinguishable by their UV/Visible spectra, the Fe-O bond should not lengthen as CcP-ES is reduced to CcP-II. Understanding the Fe(III)-OH form of CcP may help understand the various disagreements in data around ferryl hemes sample reduction – we note the 1.76 Å Fe-O distance is too long to be an oxo, the authors assign it as unprotonated, but it is too short to be a Fe(III)-OH species. As microspectrophotometry data were not reported, it is impossible to know what was in the crystals that were examined before or after the experiment. The 1.76 Å Fe-O distance may best reflect a mixture of states.

**Conclusion:**

Indisputably, the neutron crystal structure from 2016 displays a density for an -OH ligand that is too close to be a disordered aquo ligand. The Fe-O bond distance at 1.88 Å is indicative of a Fe(III)-OH species, contrary to their assignment. We have characterized the Fe(III)-OH form of APX, showing it is a low-spin ferric system with a Fe-O distance of 1.86 Å.

With closer attention to the control experiments from the 2011 report, we can observe signs of the Fe(III)-OH form of APX in the spectra. It stands to reason that the ferryl X-ray crystal structure of APX-II was reduced. The presence of the 540 nm shoulder in the un-reduced crystal could be coincidental, or it could be a hint to an additional problem of photoreduction beginning to occur. Without kinetic data on how the crystal UV/Visible data change with X-ray dosage and how that changes after immediate formation of the APX-II intermediate (if any ferric-OH is present at freezing vs. present at time of diffraction), we are at the limits of our speculation as to what happened to the deuterated crystal that was used to collect the neutron diffraction data.

**Supplementary Information:**

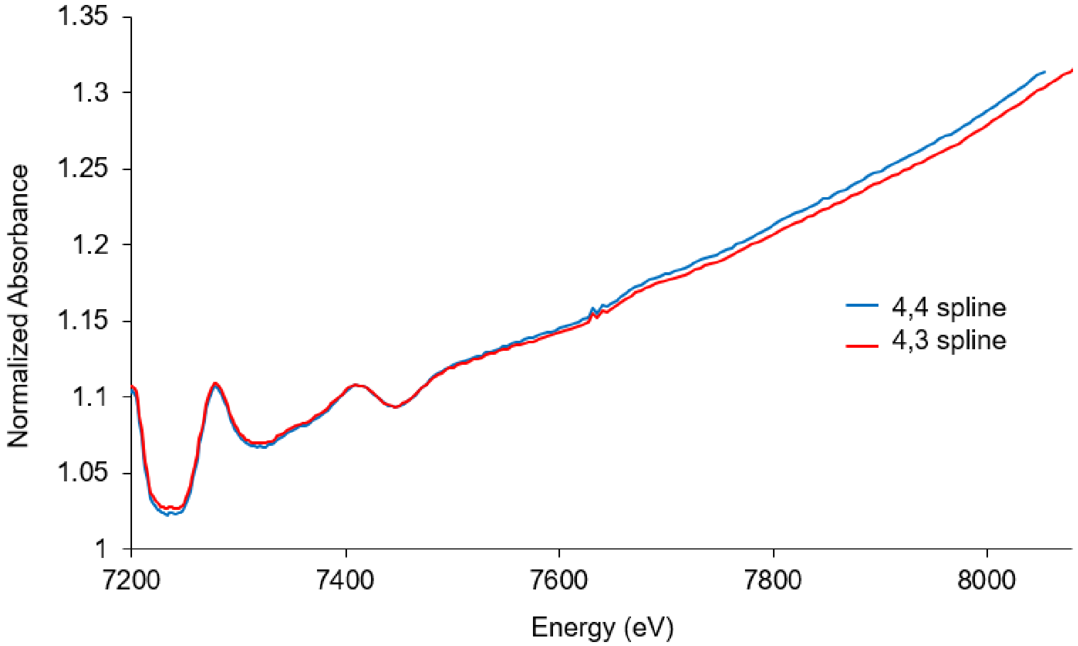

**Figure 3.S1**: EXAFS region of the X-ray absorption spectrum for Fe(III)-OH APX using 4,3 and 4,4 splines.

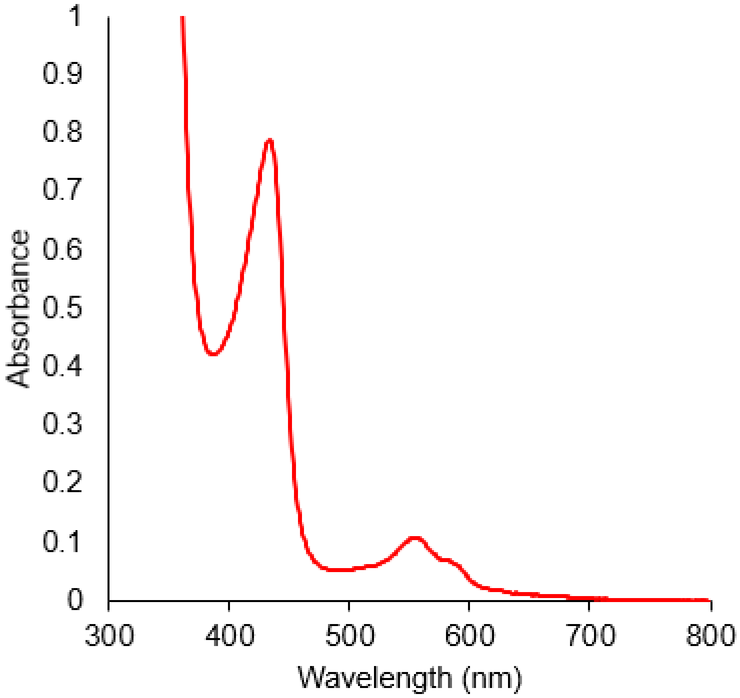

**Figure 3.S2**: UV/Visible spectrum of 5-coordinate ferrous APX. Spectrum was obtained after excess of sodium dithionite in anerobic buffer: Tris-HCl 50 mM, pH 7.

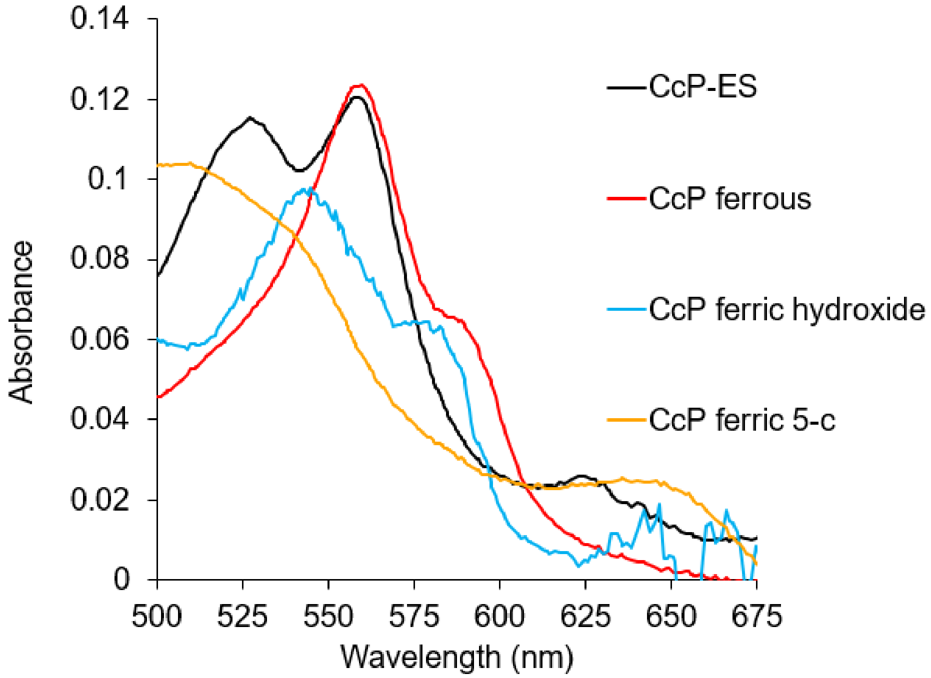

**Figure 3.S3**: UV/Visible spectra of CcP used for simulations in Figures 3.10 and 3.12. Ferric 5-coordinate CcP (resting state) is in 50 mM potassium phosphate pH 5.8. This was reacted with *m*-CPBA to form CcP-ES. Ferrous CcP was produced by the addition of excess sodium dithionite in anerobic buffer. Ferric-OH CcP (25 ms) was formed by rapid-mix pH jumping CcP from pH 5.8 pH 12.

**References:**

1. Woińska, M., Grabowsky, S., Dominiak, P. M., Woźniak, K. & Jayatilaka, D. Hydrogen atoms can be located accurately and precisely by x-ray crystallography. *Sci. Adv.* **2**, e1600192 (2016).

2. Berglund, G. I. *et al.* The catalytic pathway of horseradish peroxidase at high resolution. *Nature* **417**, 463–468 (2002).

3. Hersleth, H. P., Dalhus, B., Görbitz, C. H. & Andersson, K. K. An Iron Hydroxide Moiety in the 1.35 Å Resolution Structure of Hydrogen Peroxide Derived Myoglobin Compound II at pH 5.2. *J. Biol. Inorg. Chem.* **7**, 299–304 (2002).

4. Bonagura, C. A. *et al.* High-resolution crystal structures and spectroscopy of native and Compound I cytochrome c peroxidase. *Biochemistry* **42**, 5600–5608 (2003).

5. Hersleth, H.-P., Hsiao, Y.-W., Ryde, U., Görbitz, C. H. & Andersson, K. K. The Influence of X-Rays on the Structural Studies of Peroxide-Derived Myoglobin Intermediates. *Chem. Biodivers.* **5**, 2067–2089 (2008).

6. Green, M. T. Application of Badger's rule to heme and non-heme iron-oxygen bonds: An examination of ferryl protonation states. *J. Am. Chem. Soc.* **128**, 1902–1906 (2006).

7. Nilsson, K., Hersleth, H. P., Rod, T. H., Andersson, K. K. & Ryde, U. The Protonation Status of Compound II in Myoglobin, Studied by a Combination of Experimental Data and Quantum Chemical Calculations: Quantum Refinement. *Biophys. J.* **87**, 3437–3447 (2004).

8. Meharenna, Y. T., Doukov, T., Li, H., Soltis, S. M. & Poulos, T. L. Crystallographic and

Single-Crystal Spectral Analysis of the Peroxidase Ferryl Intermediate. *Biochemistry* **49**, 2984–2986 (2010).

9. Chreifi, G. *et al.* Crystal structure of the pristine peroxidase ferryl center and its relevance to proton-coupled electron transfer. *Proc. Natl. Acad. Sci. U. S. A.* **113**, 1226–31 (2016).

10. Kwon, H. *et al.* Direct visualization of a Fe(IV)-OH intermediate in a heme enzyme. *Nat. Commun.* **7**, 13445 (2016).

11. Gumiero, A., Metcalfe, C. L., Pearson, A. R., Raven, E. L. & Moody, P. C. E. Nature of the Ferryl Heme in Compounds I and II. *J. Biol. Chem.* **286**, 1260–8 (2011).

12. Mitchell, M., Muftakhidinov, B. & Winchen, T. Engauge Digitizer Software. Available at: http://markummitchell.github.io/engauge-digitizer/. (Accessed: 22nd April 2021)

13. Foote, N., Gadsby, P. M., Berry, M. J., Greenwood, C. & Thomson, A. J. The formation of ferric haem during low-temperature photolysis of horseradish peroxidase Compound I. *Biochem. J.* **246**, 659–668 (1987).

14. Yosca, T. H. *et al.* Setting an Upper Limit on the Myoglobin Iron(IV)Hydroxide pKa. *Jacs* **136**, 9124–9131 (2014).

15. Ankudinov, A. & Ravel, B. Real-space multiple-scattering calculation and interpretation of X-ray-absorption near-edge structure. *Phys. Rev. B - Condens. Matter Mater. Phys.* **58**, 7565–7576 (1998).

16. Lever, A. B. P. & Gray, H. B. *Iron Porphyrins, Part I.* (Addison-Wesley, 1982).

17. Kwon, H., Langan, P. S., Coates, L., Raven, E. L. & Moody, P. C. E. The rise of neutron

cryo-crystallography. *Acta Crystallogr. Sect. D Struct. Biol.* **74**, 792–799 (2018).

18. Kwon, H. *et al.* XFEL Crystal Structures of Peroxidase Compound II. *Angew. Chemie Int. Ed.* **60**, 14578–14585 (2021).

## Chapter IV: Vibrational Spectroscopy of Ascorbate Peroxidase Compound II

### Introduction: Vibrational spectroscopy and heme enzymes

The spectroscopic techniques utilized in the earlier chapters work together to establish that APX-II is an Fe(IV)-oxo species. We can state that an APX-II sample is a single ferryl species with a quadrupole splitting consistent with unprotonated iron-oxos, and that a short scattering atom at 1.68 Å is needed to accurately model the ejected photoelectron during an EXAFS experiment. Mössbauer probes the electronic environment around the Fe nucleus and shows the parameters around the nuclear spin perturbation (which we have demonstrated to be sensitive to protonation of the distal oxygen ligand) and EXAFS examines the scattered path of an ejected photon and fitting the scattering paths to models that describe the entire system, but these two methods do not directly observe the ligand or interatomic bonds themselves.

The data for APX-II are consistent with an unprotonated oxo, but it could be argued that there are other factors that contribute to the electronic structure and produce the narrow splitting in the Mössbauer spectrum for APX-II shown in Chapter II. Vibrational spectroscopy thus provides a separate avenue of investigation with definitive proof by isolating individual vibrational modes that can be attributed to specific sets of atoms. Isotopic labeling experiments allow for the specific bond of interest to be interrogated by observing predicted shifts. When taken together with other spectroscopic methods, vibrational techniques can bring light to decades-long questions in bioinorganic chemistry and enzymology.

The conventional vibrational spectroscopies are infrared absorption and Raman scattering. Infrared absorption spectra reflect the absorption of infrared photons into vibrational modes at particular resonant frequencies characteristic of functional groups. The experiment traditionally observes an absorption event that invokes a dipole moment in a vibrational mode. Raman scattering is an inelastic scattering process in which vibrational modes that change in polarizability are observed.

The Raman effect is the phenomenon of light changing frequency when it is scattered by polyatomic molecules. Raman spectroscopy is a method to examine the vibrational levels of a particular molecule, which is dependent on the structure, atomic composition, and symmetry.[1] The inelastically scattered photon loses energy to the molecule, corresponding to discrete vibrational states. The Raman effect is unfortunately a low probability process and generally produces a weak signal. If the incident wavelength is coupled to an electronic transition in the molecule, however, a portion of the Raman signal can be enhanced. This is called resonance Raman. This resonance effect offers selectivity by allowing particular chromophores within proteins to be targeted, revealing very specific interactions only around or involving the chromophore. All Raman spectroscopy examines vibrations that couple to a change in the polarizability of the molecule of interest. The polarizability changes can be induced by the absorption of a photon of sufficient energy, and results in an inelastically scattered photon. This is in contrast to infrared spectroscopy, where the interatomic bond polarizing photon is directly absorbed without emission.

In the field of heme enzymes, resonance Raman has been very effective due to the strong absorption bands of the heme macrocycle. The Raman scattering signal is normally weak because there is only a small likelihood of the inelastic scattering event occurring, but in the case of resonance Raman, the signals of certain Raman-active modes are enhanced by coupling them to electronic transitions of the heme. In these cases, an electronic excitation is coupled inelastically to molecular vibrations in which the fluoresced light contains red shifts in energy matching the energies of specific vibrational modes. This has allowed researchers to lase into electronic excitations in order to obtain detailed information about the heme heme-adjacent interatomic bonds.

If a single Fe-O bond can be identified through vibrational spectroscopy, one can determine its interatomic bond distance by treating the stretching frequency as if it is a harmonic oscillator between the two masses – an iron and an oxygen atom, or an iron and a hydroxide ion. The frequency of an Fe-(O/OH) stretching mode corresponds to the bond distance in Å, which indicates bond order. This analysis is done through application of Badger's rule, an empirical formula:

$$r_e = \frac{C_{ij}}{\nu_e^{2/3}} + d_{ij}$$

where $r_e$ is the equilibrium internuclear distance, $\nu_e$ is the vibrational frequency, and $C_{ij}$ and $d_{ij}$ are empirical constants determined for a pair of atoms by fitting a collection of $r_e$ and $\nu_e$. Badger's rule was first presented in his 1935 paper, *The Relation Between the Internuclear Distances and Force Constants of Molecules and Its Application to Polyatomic Molecules.* Here, Badger shows the linear relationship between $r_e$ and $\nu_e$ for diatomic molecules can be used for polyatomic molecules as well.[2]

Green in 2006 applied Badger's rule to heme in iron-oxygen bonds, using a library of 20 heme systems and density functional calculations.[3] This yielded the linear relationship below:

$$\mathrm{r_e} = 55.702 / \nu_\mathrm{e}^{2/3} + 1.003$$

This relationship is demonstrated in Figure 4.1. With $R^2 = 0.991$ for this model, it is reasonable to use this relationship to regularly change between Fe-O stretching frequency and interatomic

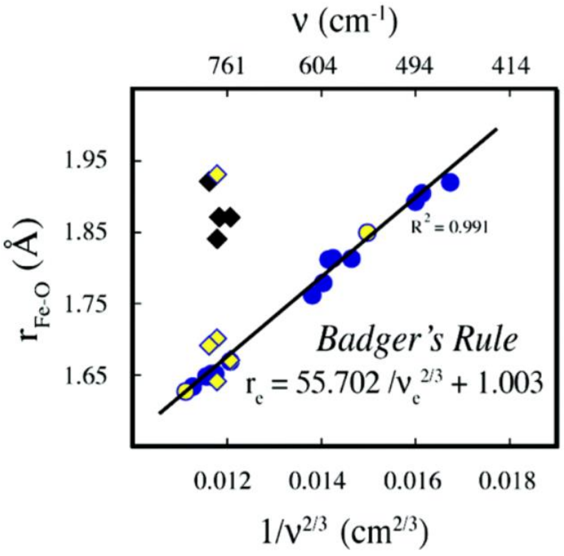

**Figure 4.1**: Fe−O bond length as a function of frequency (ν, cm$^{-1}$). Yellow and blue circles represent calculated bond distances and frequencies (scaled). Yellow circles are points that were used to evaluate the adequacy of the scaling parameter. Best-fit line to theoretical data is given by Badger's rule. Diamonds represent experimental data. Yellow diamonds are from resonance Raman and EXAFS experiments. Black diamonds are from resonance Raman and X-ray crystallography (Reproduced from Green, 2006)

distance, meaning structural information can be compared between vibrational techniques and the other methods such as crystallography and EXAFS. Figure 4.1 shows Fe-O bond length predicted by Badger's rule as a function of frequency. Fe-O bond distances of 1.6-1.7 Å, the expected distance for an Fe(IV)=O species, exists between 700-900 cm$^{-1}$. A Fe(IV)-OH species would have a slightly longer Fe-O bond at 1.75 – 1.80 Å, with a lower frequency Fe-O vibrational mode around 600 cm$^{-1}$. Even longer, Fe(III)-OH Fe-O distances range 1. 85 – 1.95 Å with lower frequency ~500 cm$^{-1}$ Fe-O stretching modes.

Analysis using Badger's rule in this way has been instrumental in understanding the photoreduction problem in the past that vastly complicated efforts to identify distal ligands in ferryl heme intermediates. Before returning to this, we would like to highlight two cases in which resonance Raman has provided essential information for distal ligand assignment in heme enzyme intermediates: horseradish peroxidase Compound II (HRP-II), and chloroperoxidase Compound II (CPO-II).

Horseradish peroxidase is a heme enzyme with a proximal histidine ligand. Horseradish peroxidase reacts with a wide range of substrates after first reacting with hydrogen peroxides to form Compound I (HRP-I) and HRP-II. X-ray absorption studies in the 1980's were at contention with each other: work by B. Chance and co-workers suggested a long Fe-O bond for HRP-II of 1.93 Å while similar experiments pointed to a shorter, approximately 1.6 Å Fe-O distance.[4,5]

Resonance Raman experiments from both Terner and Hashimoto pointed to a short Fe-O bond for HRP-II, identifying the Fe-O stretching vibration at 787 and 779 $cm^{-1}$, respectively.[6,7] These correspond to Fe-O distances of 1.65 and 1.66 Å through application of Badger's rule. The resonance Raman experiments both utilized isotopic substitution with $H_2{}^{18}O_2$ to produce HRP-II, demonstrating that the single feature attributed to the Fe-O stretching mode was sensitive to the predicted change in mass by 36 $cm^{-1}$. Shortly after, it was shown that the Fe-O stretching frequency in HRP-II is sensitive to pH, as the vibrational mode moves 12 $cm^{-1}$ between pH 5 and pH 9.[8] This provided a much more rich description of the Fe-O moiety and its environment than could be produced with XAS at the time – for HRP-II, the heme-linked ionization and change in hydrogen bonding environment made a shorter Fe-O bond more compelling, and the long 1.93 Å Fe-O bond reported earlier looked more like an outlier or reduced sample. Resonance Raman also can be used to determine the oxidation state of heme enzymes – the $\nu_4$ vibrational mode of porphyrin shifts upward with a raise in oxidation state, as it mostly involves $C_\alpha N$ stretching modes and reflects π-electron density of the porphyrin π* orbital. In the resonance Raman study of HRP-II, Hashimoto reported $\nu_4$ which was consistent with ferryl heme, lending an advantage to the argument of a short Fe-O bond.

Chloroperoxidase is an enzyme that exists as a hybrid between P450s and peroxidases – it is a thiolate-ligated heme enzyme capable of both peroxidase and P450-like activity, where the polar residues forming the distal pocket resemble the peroxide binding site.[9] EXAFS experiments pointed to a long Fe-O bond in CPO-II, suggesting that it was protonated.[10] Curiously, no resonance Raman measurement on CPO-II at the time could produce an Fe-O vibrational feature. While this finding supported the role of thiolate ligation in heme enzymes and a basic Compound II species, long Fe-O bonds were still being reported from other methods in systems with other proximal ligands. Resonance Raman experiments eventually demonstrated through isotopic substitution that the Fe-O vibrational mode for CPO-II exists at 565 $cm^{-1}$, corresponding to a longer 1.82 Å bond while avoiding sample photoreduction for direct evidence that CPO-II is a Fe(IV)-OH species.

Vibrational spectroscopy can be an extremely rich tool for understanding heme enzymes, but the techniques utilized have been generally restricted by experimental issues. The selection rules for observing only polarizability changes in resonance Raman does not obstruct ligand assignment in heme enzymes, but there is little predictability in what wavelengths will resonance-enhance the vibrational mode of interest. Resonance Raman affords an advantage of observing only the motions coupled to the electronic excitation of the heme macrocycle, thus removing many of the other vibrational modes that would contribute to the total Raman spectrum and producing a much cleaner spectrum than those in an entire protein. However, there do still remain a large number of features and feature coupling that will produce more a more complex spectrum. There is a photoreduction problem with these experiments where the electronic excitation results in an ejected electron that moves to a metal center, resulting in reduced metal ions and collecting, instead, data better representative of reduced samples. Alternatively, the excited state accessed through the resonance excitation has a different reduction potential resulting in residue oxidation, and the observation of ferric enzyme.

We obviously sought to apply resonance Raman techniques to ascorbate peroxidase Compound II. This was thoroughly examined and unsuccessful. It appears that APX-II is very photoreducible, as all observed spectra gathered through resonance Raman show signs of really being ferric enzyme. Briefly, all APX-II samples showed no signs of the $\nu_4$ vibrational mode shifting with a raise in oxidation state consistent with a ferryl species. Rather, $\nu_4$ consistently aligned with what is known for ferric enzyme. Additionally, we are unable to identify this as a ferric hydroxide species, as the Fe-O stretching region seems precluded or otherwise covered and is not sensitive to deuteration. we have explored several data collection strategies to work around the photoreduction problem, but with no success. Flowing liquid APX-II samples through a capillary tube during data collection, and spraying through a crushed needle tip, consistently showed the same $\nu_4$ feature and no sign of a distinguishable Fe-O bond at all wavelengths surveyed.

For the above reasons, we decided to pursue a new technique for vibrational spectroscopy on this intermediate, Nuclear Resonant Vibrational Spectroscopy, or NRVS. A description of the theory and experiment are in the next section.

## Principles of NRVS for hemes[11,12,13]

NRVS is, at its most basic conceptualization, a marriage between resonance Raman and Mössbauer spectroscopies. NRVS observes interatomic vibrational modes coupled to the nuclear resonance of a Mössbauer-active isotope, similar to how resonance Raman observe the vibrational modes coupled to the electronic excitation of the heme macrocycle. This provides first the advantage of doing away with the selection rules for Raman, providing a more complete picture around the probe nucleus. By this manner, one observes only the Fe-involved vibrations, and the data are less complicated.

The most relevant advantages provided here by NRVS over other vibrational techniques are the much lower photon flux over the sample compared to a resonance Raman experiment, drastically reducing the amount of ionizing radiation falling upon the sample, and the nuclear coupling. Compared to resonance Raman, there is not an electronic transition involved in NRVS and no electronic excited state. We speculate that the excited state may be the more photoreducible state of APX-II, and that pursuing nuclear resonance instead of electronically-coupled measurements would be more successful for preserving the ferryl state. Compared to X-ray crystallography (~2-5 * $10^{11}$ to $10^{13}$ photons/second) the incident beam during an NRVS experiment is smaller at 5 * $10^{9}$ photons/second. However, a single sample may be examined for multiple days as multiple scans are gathered – this allows scans from the middle of the experiment to be compared to the first scans and provides a method to investigate changes due to any hypothetical sample reduction. While the same can be said for techniques like resonance Raman, as discussed earlier, there was no sign of ferryl enzyme in the first spectra of those experiments. The experimental challenges facing this approach are that additional energy needs to be added upon the 14.4 keV photon for the $^{57}$Fe nuclear resonance in order to access the vibrational quanta. The additional energy is directly absorbed into a vibrational state, as is the case for an infrared absorption spectroscopy experiment.

Accessing those energies on the incident photon is not possible through conventional Mössbauer spectroscopy instrumentation. A traditional $^{57}$Fe Mössbauer experiment uses a $^{57}$Co source to generate the incident 14.4 keV photon. With the source situated on a motor moving back and forth quickly, the neV scale of energies required to access the various nuclear states can be sampled, given the typical magnetic field strengths employed (~50 mT). In order to sample vibrational quanta, one needs to sample energies on the scale of meV - this corresponds to meters-per-second velocities for the motor setup described, which is not feasible. Therefore, it's necessary to use a synchrotron and a monochromator to access the required incident energies.

Figure 4.2 shows an overview of an NRVS experiment for $^{57}$Fe. Photons that are absorbed by the sample at any given wavelength are determined by measuring the resulting 6.4 keV atomic fluorescence emitted from the excited $^{57}$Fe atoms. Detection is formally through fluorescence, despite the fact that the experiment is investigating absorption phenomena. At the correct energy to excite the $^{57}$Fe nucleus, the nuclear state will excite from the 1/2 spin state (ground nuclear state 0) to 3/2 ($E_0$) and relaxation of this will produce some degree of internal conversion. This will produce an ejected K-shell electron with a 6.4 keV fluorescence event as that hole is subsequently

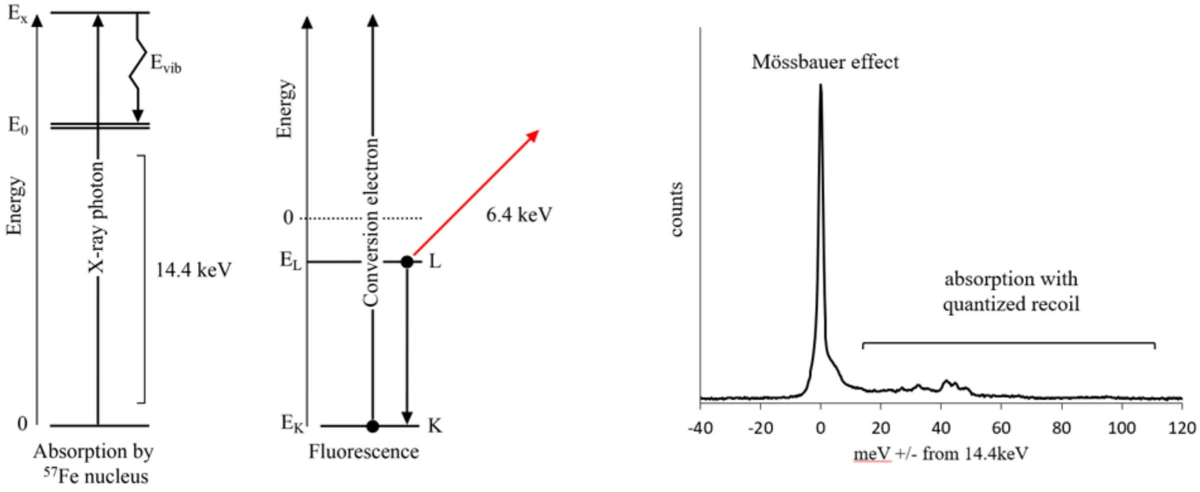

**Figure 4.2**: (Left): Overview of the nuclear absorption / photon emission event producing the 6.4 keV signal photon. Note, depicted are the simultaneous absorption by the nucleus (Mössbauer resonance) and some vibrational quanta ($E_{vib}$). (Right): Raw data for APX-II demonstrating the high signal for the nuclear resonance and signal falloff as energy is moved away from the nuclear cross section.

filled by a L-shell electron. With additional energy to access $E_x$, $E_{vib}$ is contained in $\Delta E$ from 14.4 keV, corresponding to a phonon produced for a particular vibrational mode at the proper energy from the Mössbauer resonance peak (Mössbauer-resonant condition + phonon energy).

Figure 4.3 details the physical experimental setup: Synchrotron radiation is generated from the electron beam by an undulator magnet that makes the electrons turn at hard angles to generate cascades of synchrotron radiation. This is focused first by heat load monochromators, then by ultra-high resolution monochromators. The focused beam is then passed through the sample with a narrow 1 mm x 10 mm footprint, and signal is detected through an avalanche photodiode detector transverse to the sample. The sample is affixed to a cryostat for the duration of the experiment. Pictures of the cryostat and sample setup can be found at the end of this chapter.

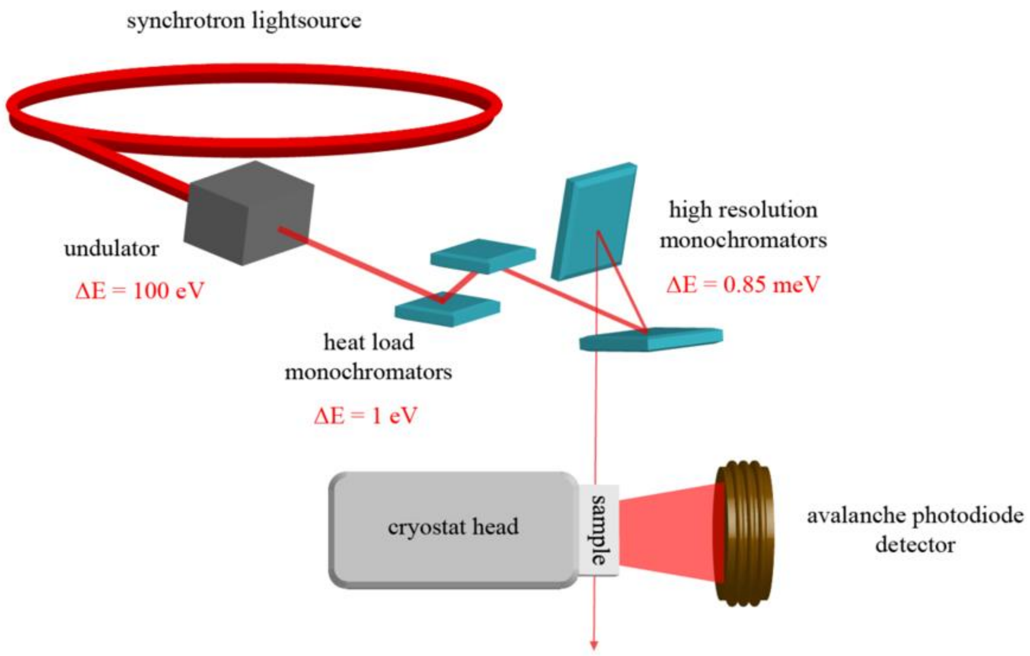

**Figure 4.3**: Overview of the beam path for an NRVS experiment at the Advanced Photon Source, Argonne National Laboratory. This is generalizable to other beamlines.

Figure 4.4 shows a simulated Fe-only vibrational density of states (VDOS, or PVDOS for *partial* vibrational density of states) for a simple model: protoporphyrin IX with a central Fe atom, distal oxygen ligand and proximal imidazole ligand. This loosely reflects the heme center of Compound II of a peroxidase, with a +4 oxidation state on the Fe atom and a short Fe-O double bond. The Fe-O stretching mode is clear as no other iron-involved motions cover this frequency range. Generally, the 500 – 900 cm$^{-1}$ region is devoid of other features, making it an excellent field for fine detail around ligand bonding. In this model, there is no hydrogen bonding or more complex structure to impact the simulated NRVS spectrum, and as of such we observe a single Fe-O stretching feature at 802 cm$^{-1}$. The Fe-O tilting features (300 – 400 cm$^{-1}$) are from vibrational modes at 330, 325, and 313. Figure 4.5 shows the model used for this simulation, along with the vibrational modes at 330 and 313, to demonstrate Fe-O tilting.

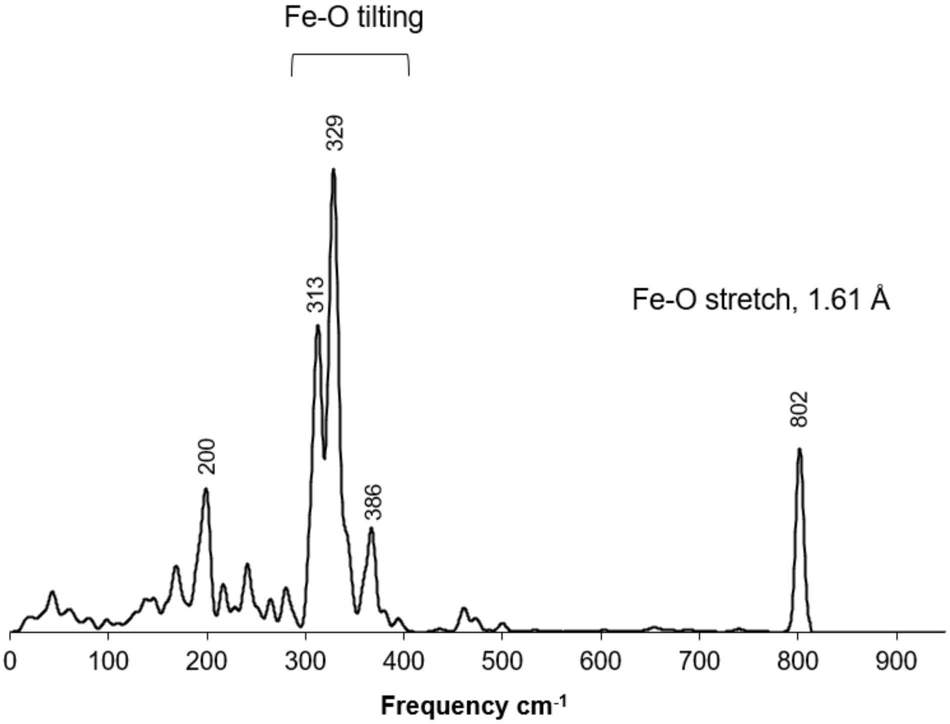

**Figure 4.4**: Simulated Fe-PVDOS spectrum of a histidine-ligated heme with a distal oxo ligand. The model utilized is shown in Figure 4.5. The Fe-O tilting region has been highlighted – this is generalizable to other heme systems and is sensitive to changes in protonation, in which the prominent tilting mode feature (here observed as an overlap of 330 and 325) are further split, such that two prominent tilting features are observed from increased separation. Calculations were performed as described in the methods section.

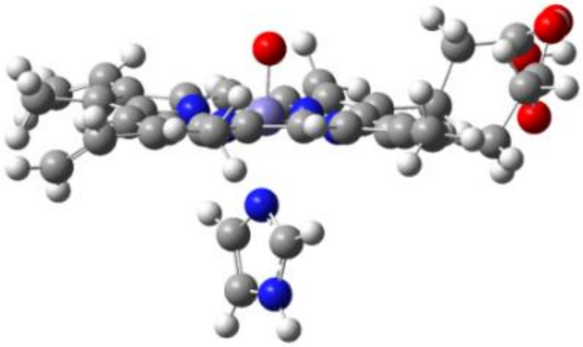

**Figure 4.5**: (Top): The model used for Figure 4.4 calculations. The model consists of a heme macrocycle and proximal imidazole ligand and distal oxo ligand. Starting geometry came from the X-ray crystal structure for ascorbate peroxidase, PDB: 5JQR. (Bottom): Fe-O tilting modes from the frequency calculation. Arrows show the displacement vectors for the atom. Red atoms are oxygen, grey atoms are carbon, blue are nitrogen, and white are hydrogen. The vibrational mode at 330 $cm^{-1}$ (left) demonstrates more oxygen involvement than 313 $cm^{-1}$ (right).

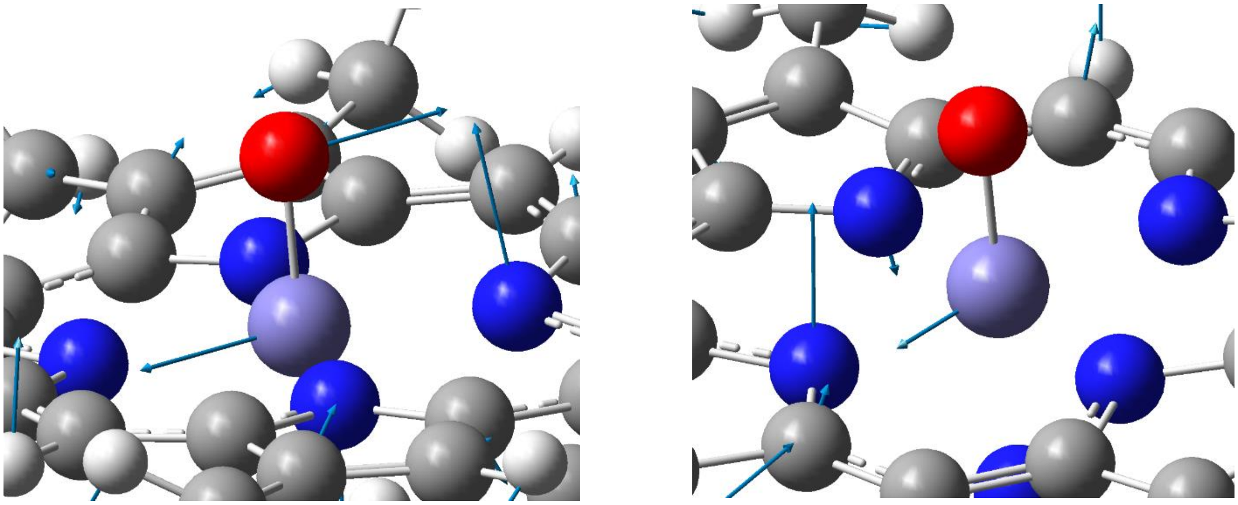

**Applications of NRVS:**

Interpretation of NRVS spectra has been greatly assisted by DFT calculations, as illustrated above. Because the vibrational modes observed during the experiment are only those involving the probe nucleus, the $^{57}$Fe atom, using simple models for the Fe center to produce simulated NRVS spectra provide accurate descriptions of the data. Only the immediate interatomic environment around the iron is relevant to the spectroscopy. By including these features in Gaussian calculations, researchers can simulate the complete set of vibrational modes, keep only the iron-involved motions, and compare to experimental data.

In heme enzymes, NRVS has been useful for understanding ligands through comparison to DFT and synthetic complexes. For example, NRVS data were collected on nitric oxide complexes with myoglobin (MbNO) and compared to data on the synthetic analogue Te(TPP)(NO) and Te(TPP)(1-MeIm)(NO) to demonstrate that the imidazole ligand lengthens the Fe-NO bond, supporting a proposed mechanism for NO activation in heme proteins.[14] This measurement stood out as contrasting with previous vibrational data indicating the Fe-NO frequencies in MbNO were 521 cm$^{-1}$ in a five-coordinate complex (no proximal histidine) and 552 cm$^{-1}$ in six-coordinate, suggesting a *shorter* Fe-NO bond distance despite the trans influence of the proximal ligand.[15] This contrasted with what was known for model Compound structures, which supported a lengthening of the Fe-NO bond due to the trans influence of an imidazole ligand.[16] NRVS data of (TPP)(1-MeIm)(NO) in the MbNO study showed a Fe-NO stretching frequency at 440 cm$^{-1}$, analogous to the feature in MbNO in the 440-450 cm$^{-1}$. The shorter Fe-NO bond distance appears to be a misassignment.

Further examination of myoglobin by NRVS was soon after performed on Compound II (Mb-II). Mb-II possesses a proximal histidine ligand and a distal oxygen ligand of debated identity. Crystallographic investigations of ferryl myoglobin point to a long Fe-O bond, while EXAFS suggested a short oxo species.[17,18] NRVS of Mb-II unambiguously revealed a Fe-O stretching feature at 805 $cm^{-1}$, showing a sharp feature without any sign of photoreduction.[19]

In the synthetic literature, NRVS has been much more readily applied. This stems from the concentration requirements for the experiment – signal count rate can be improved for every additional $^{57}$Fe atom in the sample. Crystals of a sample are ideal, followed by very high concentrations that are just not achievable with protein samples. A study by Weitz et al. highlights the utility of this technique, in which a series of $Fe^{III}$-hydroxo and $Fe^{IV/III}$-oxido complexes with a series of intramolecular H-bond changes was investigated.[20] The researchers elegantly demonstrate the effects of hydrogen bonding on the Fe-O vibrational mode, showing that singular changes in the hydrogen bonding environment drastically changes the Fe-O vibrational frequency, and accordingly, Fe-O bond length.

The experimental challenges with an NRVS experiment begin with the sample concentration. Ten mM is not readily achievable for most proteins and being able to prepare a reaction intermediate species at such a concentration is rare. Unfortunately, without a high concentration, the count rate will not be sufficient to collect data very far from the recoilless Mössbauer peak. This is because the vibrational modes in an NRVS spectrum span hundreds of meV, significantly far from the nuclear cross section, with a few counts per second for a particular vibrational mode that yields hundreds of counts per second.[11] For biological samples, it can be roughly estimated that one would obtain 30 counts per second on the elastic peak per mM $^{57}$Fe, meaning a 10 mM [monoheme enzyme] may get 300 counts on the elastic peak, but at ~800 cm$^{-1}$ it may get one count every ten seconds and require days' worth of data collection to achieve a usable signal-to-noise ratio.

## Experimental Methods:

### Growing and purifying APX:

$^{57}$Fe ascorbate peroxidase from glycine max was recombinantly expressed and purified as previously described in this text. Briefly, BL21(DE3) cells were grown in M9 minimal media to OD 0.6. and IPTG was used to induce expression for 24 hours at 30°C. Purification was performed by ammonium sulfate fractionation and ion exchange chromatography to Rz 2.2.

### Preparation of APX-II samples for NRVS and Mössbauer:

$^{57}$Fe APX was concentrated to 10 mM in a 50 mM potassium phosphate buffer then mixed 2:1 with oxidant such that the final concentration of MCPBA is 5 equivalents, and the final APX concentration is 6.66 mM. This was aged over 30 seconds as we pipetted this into a Mössbauer cup and NRVS sample cells, then froze in liquid nitrogen after the cell window was placed in. Assembly of the NRVS cell on to the copper adapter happened at the same time. The 30 second time point reflects when the Mössbauer cup was frozen.

Mössbauer Spectroscopy of APX-II:

Data were collected using a spectrometer from WEB research in constant acceleration mode using transmission geometry and a 50 mT magnetic field applied parallel to the $\gamma$-beam. Spectra were recorded at 77 K using a Janis SVT400 cryostat. Isomer shifts were calibrated using the centroid of the spectrum of a foil of $\alpha$-Fe at room temperature. Data analyses were performed using the program WMOSS from WEB research.

NRVS of APX-II:

Nuclear Resonant Inelastic X-ray Scattering data for $^{57}$Fe were collected at sector 3-ID-D of the Advanced Photon Source at Argonne National Laboratory. Electron bunches were passed through an undulator inserted in the storage ring that produced broad bands of synchrotron radiation that were monochromated to 1 eV centered around the nuclear resonance energy of the $^{57}$Fe isotope, 14.4 keV. This was further narrowed to a ~1 meV resolution. The energy range was scanned from -30 to 120 meV from the nuclear resonance in 0.25 meV steps. The emitted X-rays were detected by an avalanche photodiode (APD) detector that was timed to exclude the X-ray pulses but observe nuclear-delayed photons (121 ms). The photons detected included Fe k-alpha fluorescence at 7.4 keV and 14.4 keV direct nuclear emission. Data were collected at a count rate of 300 Hz at the nuclear resonance peak for the APX-II in $H_2O$ experiment, and 150 for the $D_2O$ experiment. The general data collection strategy spent 3 seconds at each energy point. 138 scans were used to produce the APX-II in $H_2O$ spectrum. Data were collected at ~ 25 K. Measured NRVS data were processed using the program PHOENIX.

## Simulating Fe-PVDOS Spectra:

Gaussian16 was used to calculate vibrational frequencies and normal modes.[21] Calculations were performed at the B3LYP/6-311G level. Atomic masses and normal mode vectors were then used to calculate the mode composition factors, which gave the fraction of the $^{57}$Fe kinetic energy in each mode. NRVS spectra were generated by weighting a gaussian centered at each vibrational frequency by the appropriate mode composition factor. A line width (FWHM) of 10 cm$^{-1}$ was used. The FORTRAN program for generating PVDOS spectra from the Gaussian 16 output files was written by MTG and can be found with the published APX-II Fe-PVDOS spectrum.

## Sample holders:

***APS Rectangular Cell*** – provided by Dr. Jiyong Zhao at Argonne National Lab, Advanced Photon Source sector 3. Design is by Dr. Timothy Sage at Northeastern University.

This is a HDPE sample holder that attaches to a Cu base plate, sandwiching a rectangle of sapphire between the two. This assembly is mounted on to the cryostat head at the beamline. This was the sample holder provided for the 2019 experiment. Liquid protein sample was pipetted into the narrow groove of the sample cup and the sapphire plate was inserted into the top of the cup, covering the protein-filled groove, prior to freezing the cup in liquid nitrogen. Once frozen, the sample holder was attached to a pre-frozen (immersed in $LiN_2$) base plate with screws in the corners. This was finally attached at the beamline by a screw slotted in the Cu base plate. The purpose of the sapphire is for better thermal conductivity than the Cu, meaning the sample can be better cooled during the course of an experiment.

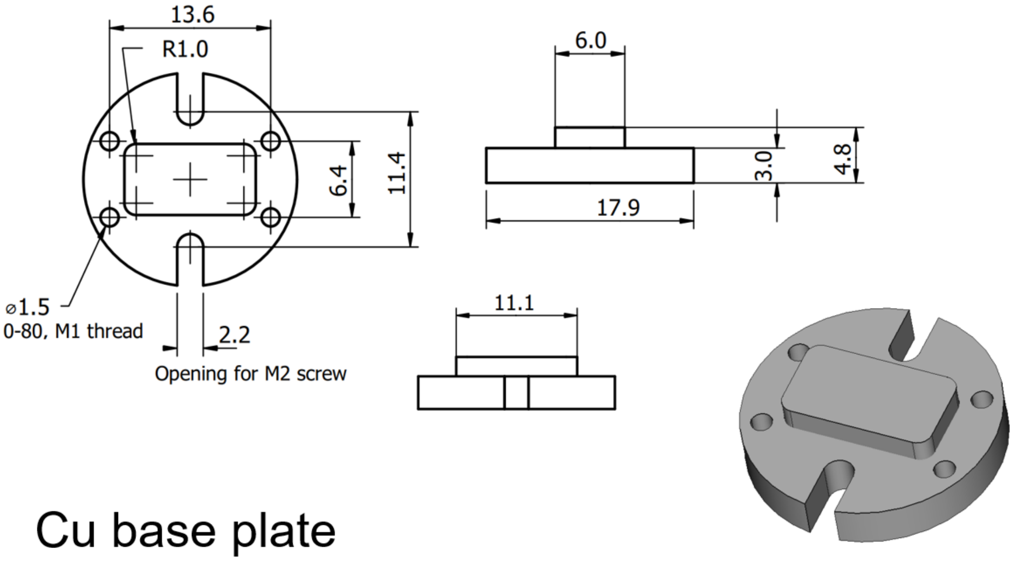

Cu base plate

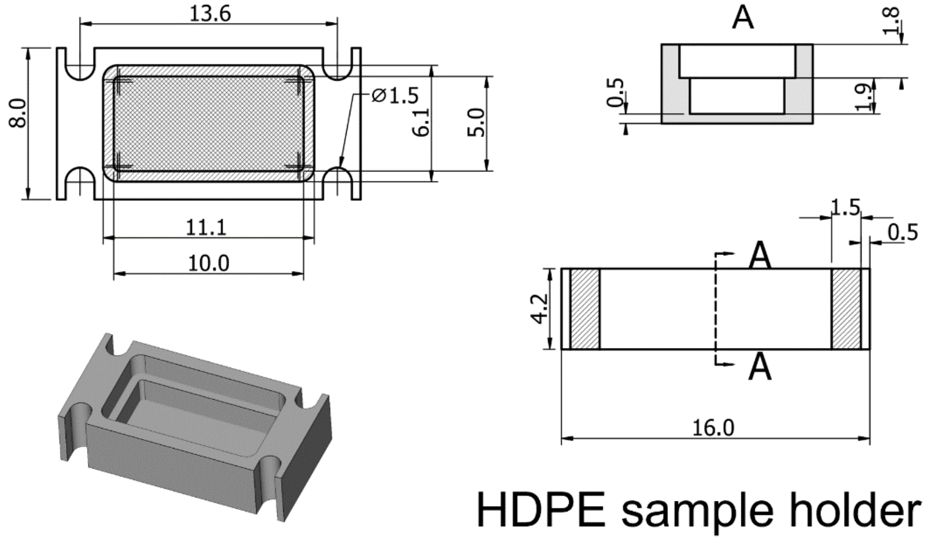

HDPE sample holder

**Figure 4.6**: The APS rectangular-style sample holders (designed by Dr. Timothy Sage) – these are the sample holders used for the NRVS measurement that produced Figure 4.4. Four screws secured the inverted HDPE sample holder onto the Cu base plate, sandwiching a sapphire window that fits in the larger groove of the sample holder.

### ***Mössbauer Jr. Cell***

Important to our experimental efforts is the ability to use multiple techniques on the same exact sample. Previously, our solution for this was to react large volumes of reactions such that we could distribute the reaction between various sample containers – this is an issue when trying to create highly concentrated protein intermediate samples due to the amount of enzyme used to determine optimal conditions. Therefore, we pursued creating a sample holder that could be used with our Mössbauer spectrometer and then fit on the NRVS beamline, such that a minimum amount of sample could be used. This sample holder was designed to fit in the Mössbauer sample holder slot with the help of an adapter ring to increase the cylinder's footprint. The brass mount depicted below was designed to be compatible with the Cu base plate from the earlier design.

Our sample holder was made from Delrin, instead of HDPE. Delrin is much less transparent to photons of our energies of interest, meaning we receive less signal using Delrin sample holders versus HDPE. The mistake here was the assumption that because our Mössbauer cups are Delrin, this would be good for NRVS too – instead it appears that creating our Mössbauer sample holder cups from HDPE may be an avenue to increase signal for that instrument. Unfortunately, this means that the Mössbauer Jr. sample cups yield about 2/3rds the signal of the *APS rectangular*-style sample holders. Beyond this, the sample holder only takes up 7.5 mm of the 10 mm beam footprint, further reducing counts compared to the rectangular-style NRVS sample holder. This narrower size was chosen because of the position of the mounting screws that attach the adapter to a spacer on the cryostat head. The spacer has threads for the mounting screws. In the updated design at the end of this chapter, we redesign the spacer to accommodate wider mounting screw positions and larger sample holders.

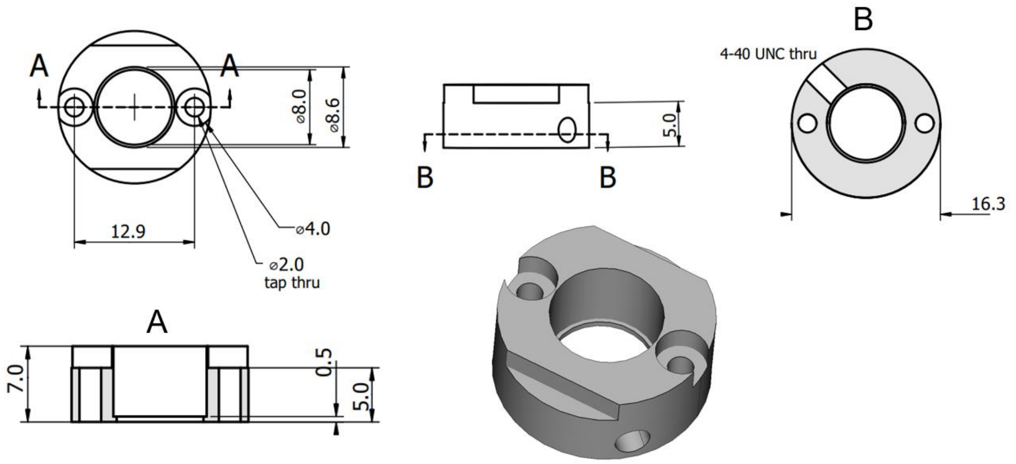

Brass Adapter for Möss Jr.

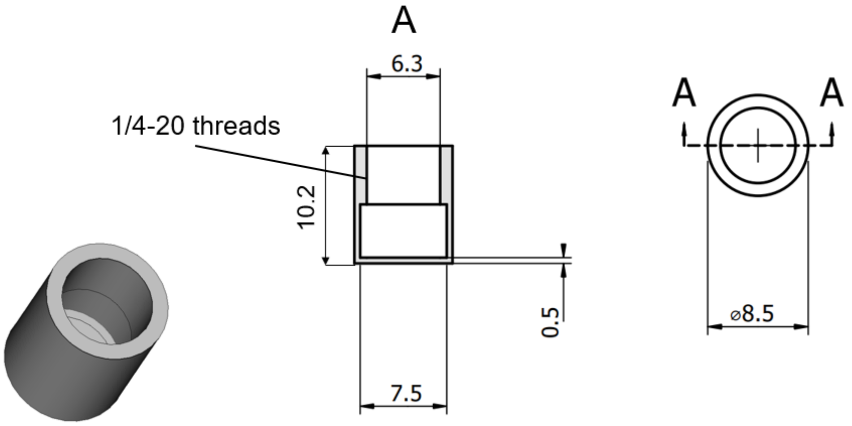

Delrin Möss Jr. sample holder

**Figure 4.7**: The Mössbauer Jr. sample holder and adapter. Note the 8.5 mm cup diameter, as opposed to the 10.5 mm cup diameter of the Mössbauer Sr. cup (future directions). A cap with threads is needed to form the top of the sample holder that can couple with the internal threads of the cup to secure the sample inside. For the 2020 NRVS $D_2O$ experiment, it was necessary to file the height of the sample holder down from 10.2 mm to allow the sample / adapter to fit at the beamline.

## Results and discussion:

### NRVS of APX-II:

APX was reacted with *m*-CPBA at pH 7 to generate APX-II at 6.66 mM. The reaction mixture was pipetted into NRVS and Mössbauer sample holders, and the reaction was quenched simultaneously by placing both sample holders into liquid nitrogen 30 seconds after mixing. Because of the high protein concentration, a freeze-quench apparatus was necessary to use as a mixer because the syringe-driven, grid-mixer setup allowed thorough mixing that could not be achieved with a hand quench. APX-II was isolated as a single species via Mössbauer prior to the NRVS experiment to establish it was void of APX-I or other iron species (Figure 4.8). Mössbauer spectroscopy is sensitive to the oxidation state and electronic structure of the $^{57}$Fe nucleus; thus, we are confident in stating that the sample used for the NRVS experiment is >90% APX-II. The Mössbauer parameters $\Delta E_q = 1.66$ and $\delta = 0.05$ mm/s are consistent with an Fe(IV) species, and consistent with what has been shown earlier in chapter II of this work.

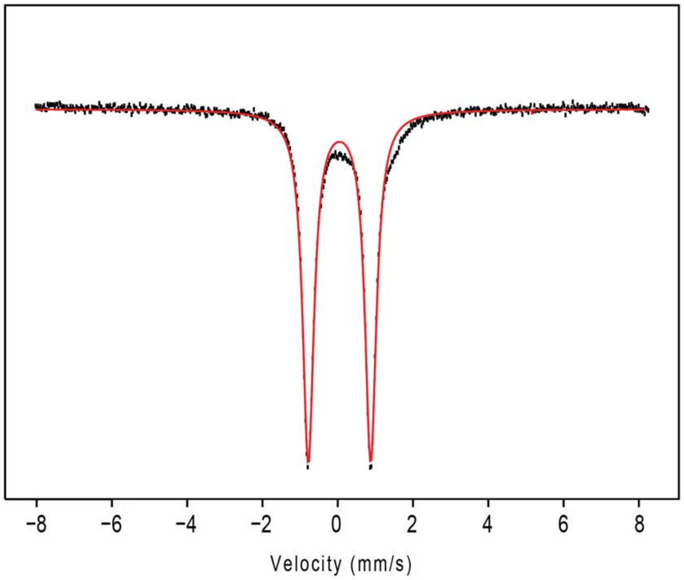

**Figure 4.8**: Mössbauer spectrum (77 K, 50 mT ||) of the APX-II sample. Analysis of the spectrum reveals that APX-II was generated in high yield (~90%). The Mössbauer parameters $\Delta E_q = 1.66$ mm/s and $\delta = 0.05$ mm/s are consistent with an Fe(IV) species and in agreement with those previously reported for APX-II at 4K.

Figure 4.9 shows the Fe-PVDOS spectrum for APX-II. The spectrum is similar to what has been previously observed for an oxo ligand on the histidine-ligated heme of myoglobin Compound II.[19] While the NRVS data for Mb-II show a sharp Fe-O vibrational resonance at 805 $cm^{-1}$, what is observed in Figure 4.9 is more broad. The data for APX-II suggest two features in the Fe-O stretching range (600 – 900 $cm^{-1}$) both within the expected frequency for an oxo species. The peaks at 732 $cm^{-1}$ and 770 $cm^{-1}$ correspond to Fe-O distances of 1.69 Å and 1.67 Å, respectively, for APX-II. This agrees with our previous work using EXAFS to demonstrate APX-II is an iron(IV) oxo.

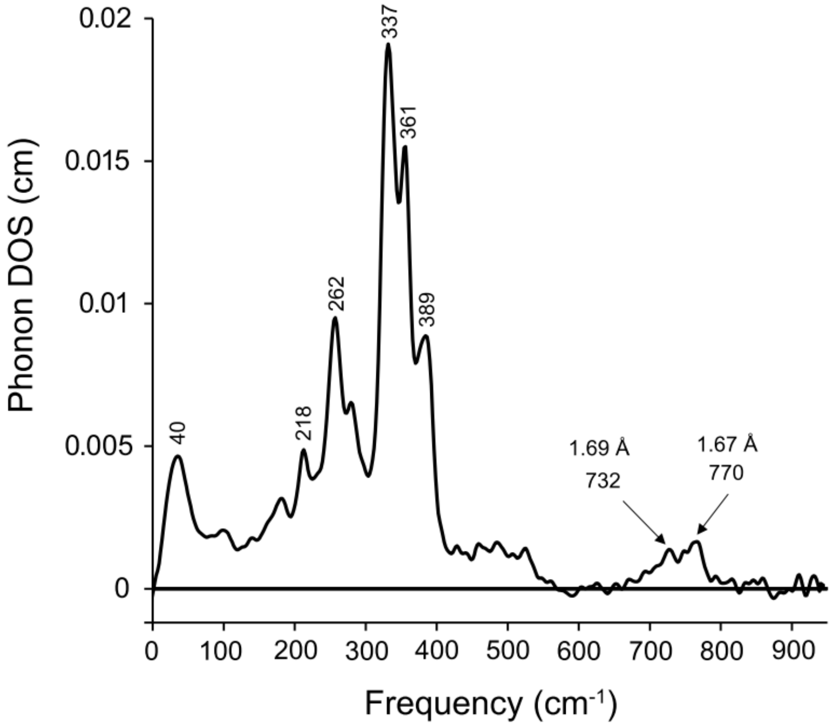

**Figure 4.9**: Fe-PVDOS spectrum of APX-II, pH 7. Peaks in the iron(IV) oxo stretching region are labeled. The distances obtained from Badger's rule are shown.

Our NRVS experiments support that APX-II is an Fe(IV)=O species. Data were collected at the Advanced Photon Source at Argonne National Laboratory over four days. In the 700-800 cm$^{-1}$ region, we believe the data are best described as two separate features from overlapping Fe-O vibrational modes. Only the Fe-O bond would vibrate at frequencies that high (considering that NRVS only observes Fe-involved phonons), and the features taken together as one singular feature would be too wide. Our calculations and comparison to literature data indicate that features at 337, 361, and 389 cm$^{-1}$ correspond to Fe-O tilting modes. The prominent features at 218 and 262 cm$^{-1}$ and the lower frequency features are not easily modeled – these appear to be Fe-N vibrations sensitive to changes in the heme geometry and the hydrogen bonding of the proximal histidine ligand.

During the course of the NRVS experiment, we were concerned that photoreduction of the sample was occurring and that we would encounter the same issue that limited resonance Raman experiments on APX-II. We sought to look for changes across various days of sample examination that would indicate a change in oxidation state or moving Fe-O vibrational feature. Shown in Figure 4.10 are the data that produced Figure 4.9, broken up into the first and second half of the data set. We see no sign of photoreduction in these data. Specifically, there is no growing sign of a Fe(III)-OH vibration is noticeable as no single feature grows in over the course of the experiment.

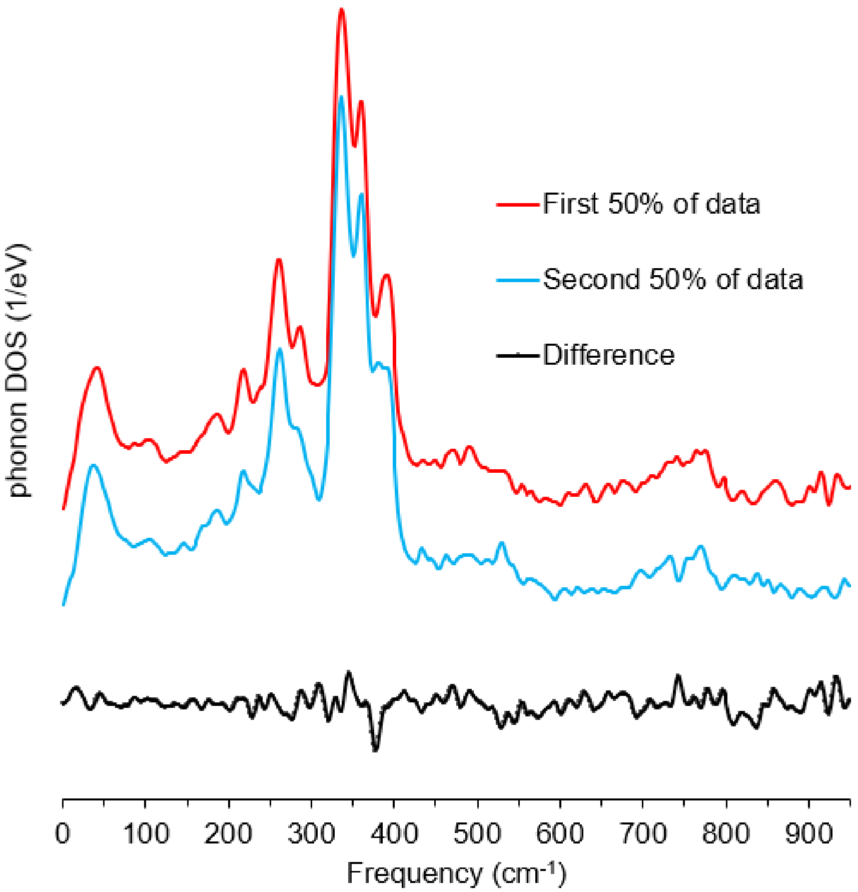

**Figure 4.10**: Fe-PVDOS data for APX-II split into the first and second 50% of data to explore changes in the spectrum during data collection.

The actual feature maxima have been labeled in Figure 4.9. We also explored fitting the vibrational features – Figure 4.11 shows two fitting scenarios using two gaussians. In fit 1, the 770 and 732 features are treated separately with narrower FWHM (37.0 and 39.8 cm$^{-1}$, respectively). This does well to describe the two features separately but neglects a region between the two at ~750 cm$^{-1}$, and the lower frequency shoulder of the 732 cm$^{-1}$ feature. The adjusted R$^2$ for this fit is 0.82. Fit 2 shows a minor improvement with an R$^2$ of 0.89, instead describing the 732 cm$^{-1}$

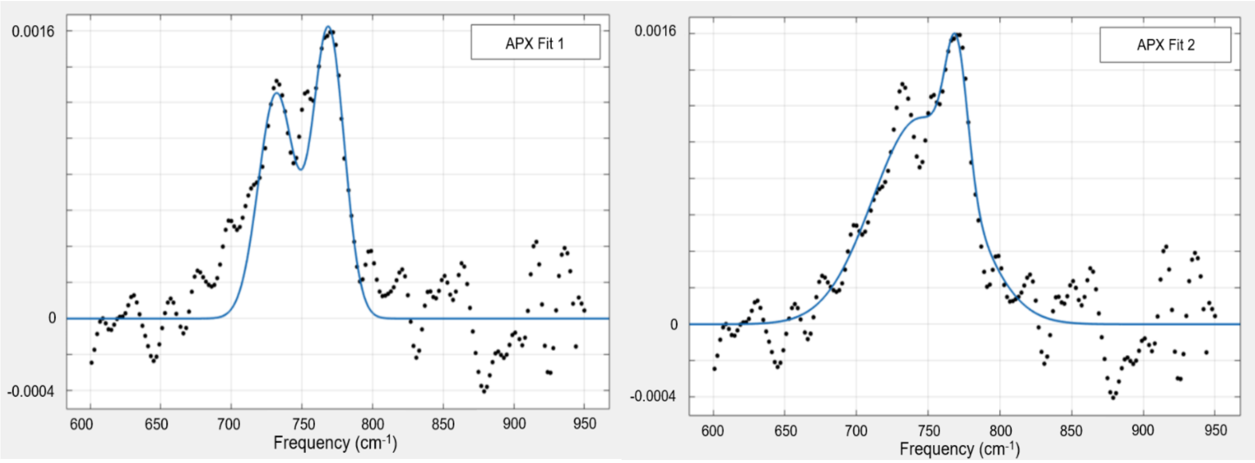

**Figure 4.11**: Fitting APX-II Fe-PVDOS spectrum in the 700 – 950 cm$^{-1}$ region. Fits were performed using MATLAB and a two gaussian model. (Left): Detailing two Fe-O stretches of narrower gaussians comparable to the single narrower feature seen in Mb-II. (Right): The leftmost gaussian is instead broad, FWHM 110.9 cm$^{-1}$, reflecting a distribution model of Fe-O stretches covering the 700 – 800 cm$^{-1}$ region.

feature as a broad 745 cm$^{-1}$ gaussian with a very broad 110.9 cm$^{-1}$ FWHM and the 770 feature instead a narrower FWHM of 25.71 cm$^{-1}$.

In order to better understand the features observed in APX-II, we turn to Mb-II for comparison. Figure 4.12 shows a reproduction of the Fe-PVDOS spectrum of Mb-II from Sage 2008, narrowed around the Fe-O stretching feature. Mb-II has a known Fe-O length of 1.65-6 Å.[22] The Fe-O stretching feature of Mb-II fits a singular gaussian at 806 cm$^{-1}$, 33.6 cm$^{-1}$ wide.

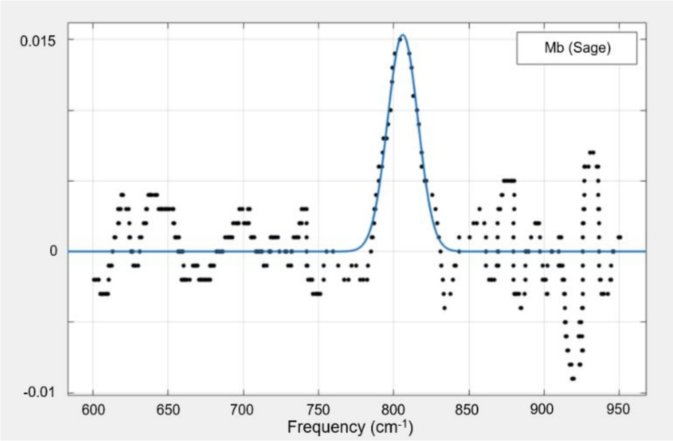

**Figure 4.12**: Fe-PVDOS data for Mb-II by Sage 2008. Data were reproduced using Engauge Digitizer. See prior chapter for methods. Fitting was performed using MATLAB. In the Fe-O stretching region, Mb-II shows a singular feature at 806 cm$^{-1}$ with a FWHM of 33.6 cm$^{-1}$.

The broadness of an iron(IV) oxo resonance is not unprecedented – it has been observed before in cytochrome c peroxidase Compound ES (CcP-ES).[23] There, the authors suggested that $H_2O$ vibrational rotational bands near 710 $cm^{-1}$ could mix with the Fe-O vibration, broadening the resonance and decreasing its intensity. This description is consistent with the sharpening of the CcP-ES ferryl resonance in $D_2O$, which has vibrational rotational bands that are lower in energy that do not mix with the Fe-O vibration. It is difficult to determine the band broadening in the resonance Raman spectra of CcP-ES because of the background signal, but the difference spectrum between $^{16}O$ and $^{18}O$ isotopic labeling ($H_2O_2$ and $H_2O$) suggest the sharp feature produced with $^{18}O$ labeling is spread across ~15 $cm^{-1}$ with $^{16}O$. Broad Fe-O stretching features would not be unexpected, given the network of hydrogen bonds to the ferryl oxygen in structures of APX.

Before continuing our discussion on hydrogen bonding, we would like to acknowledge the possibility of two different active site states being present in APX-II at pH 7, near the $pK_a$ of some amino acid residue. This concept has been shown before in horseradish peroxidase Compound II where the Terner group observed the Fe-O bond's vibrational mode change frequency from pH 5 to pH 9 by 11 $cm^{-1}$. The residue responsible for this is thought to be a histidine located in the distal pocket that is variably protonated over this pH range. APX similarly possesses a histidine residue in the distal pocket. A similar $pK_a$ *near* 7, the pH where the NRVS sample was prepared, could produce a mixture of two Fe-O vibrational modes reflecting unprotonated and protonated forms of the distal histidine. Crystal structures of APX-II show water molecules in the active site hydrogen bonding to the distal heme ligand and the distal histidine residue – it is plausible that the water molecules in the hydrogen bonding network will change position as the protonation state on the distal histidine changes, reflecting two hydrogen bonding environments for the Fe-O moiety. Two states of different hydrogen bonding networks could produce a broader Fe-O resonance. Consistent with this, the sharper Fe-O feature is the shorter one, as it would be expected to have less hydrogen bonding interactions and a stronger Fe-O bond.

The separation between the two vibrational modes from the Fe-PVDOS data of 39 $cm^{-1}$ is considerably larger than the 11 $cm^{-1}$ change in frequency of the Fe-O stretching mode observed in HRP-II. Structural data suggest HRP-II has a more simple hydrogen bonding network compared to APX-II, with a single-file chain of water molecules leading to the ferryl moiety while APX-II has 2 oxygen atoms within 3 Å of the ferryl oxygen.[24] NRVS experiments conducted on myoglobin Compound II (Mb-II, a histidine-ligated Fe(IV)=O species) in 2008 by Sage et al. identified the Fe-O stretching mode at 805 $cm^{-1}$. This frequency is consistent with our calculations for an Fe(IV)=O porphyrin without any hydrogen bonding interactions on the ferryl oxygen and aligns with structural data on Mb-II indicating that there is no room for water molecules to hydrogen bond with the ferryl oxygen. Could a population of two extensive hydrogen bonding environments in APX-II describe the Fe-O vibrational modes' shift to a lower frequency (lengthening of the Fe-O bond) and two features?

Figure 4.13 shows the active sites of APX-II, HRP-II and Mb-II. The yellow density is the pocket containing the heme cofactor generated using the program GHECOM.[25] The heme group was not included in modeling this density. This method suggests Mb-II has a pocket volume of 762 Å, where the volume of the heme itself is 530 $Å^3$ in this structure (as determined through ChimeraX). The figure shows the closest water molecules to the ferryl oxygen represented as just singular oxygen atoms. Mb-II does not have any of such water molecules involved in hydrogen bonding, and the heme takes up 70% of the pocket's volume. In APX-II, there is room for multiple waters in the active site in a more extensive hydrogen bonding network than what is observed with HRP-II. APX-II shows two oxygen atoms that could be reasonably interpreted as water molecules within hydrogen bonding distance, while HRP-II has a single chain of 3 oxygen atoms, and narrower access to the ferryl oxygen. Via GHECOM, the active sites of APX-II and HRP-II were of equal volumes (1,339 and 1,336 $Å^3$).

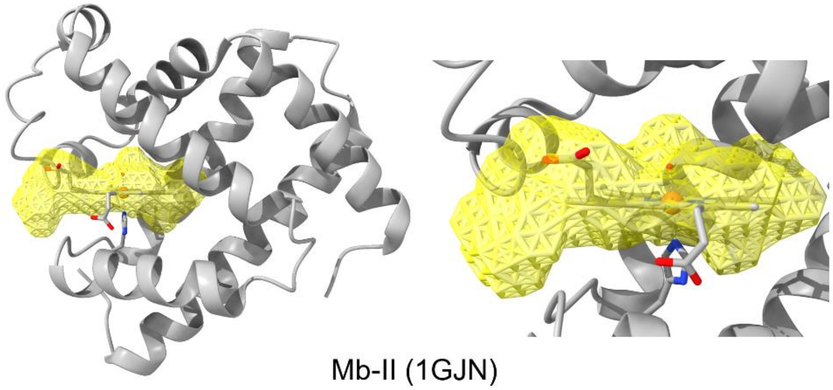

Mb-II (1GJN)

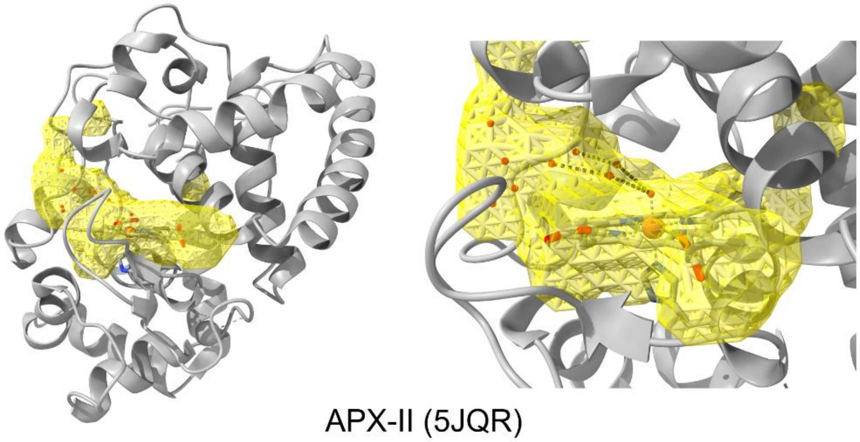

APX-II (5JQR)

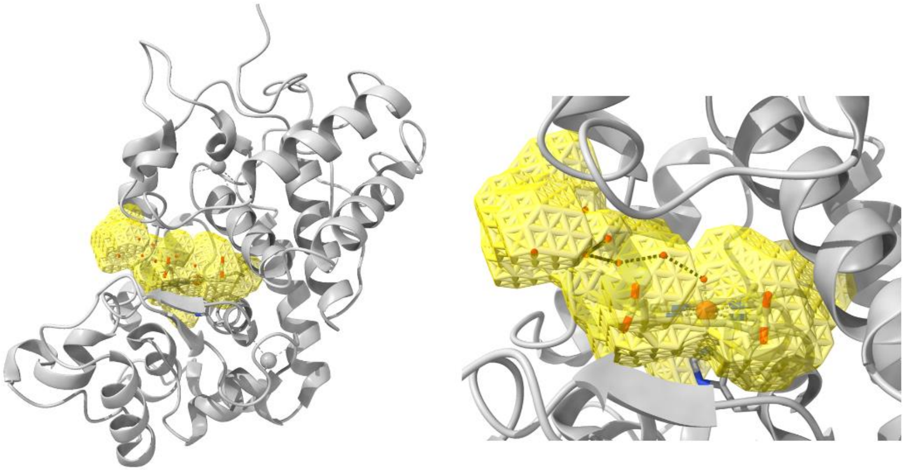

HRP-II (1H55)

**Figure 4.13**: (Top): Myoglobin Compound II, PBD: 1GJN. (Middle): Ascorbate peroxidase Compound II, PDB: 5JQR. (Bottom): Horseradish peroxidase Compound II, PDB: 1H55. The yellow density is the active site pocket modeled with GHECOM using the PDB structure. The hydrogen bonding networks for the closest water molecules to the ferryl oxygen is shown for APX-II and HRP-II.

To continue the discussion of hydrogen bonding interactions and vibrational spectroscopy, we turn to the guidance of DFT simulation in the following section.

## Gaussian Models for simulated Fe-PVDOS:

In order to investigate the effects of hydrogen bonding in the active site, we performed density functional calculations on models of APX-II. Fe-PVDOS spectra were produced from Gaussian 16 output files for frequency calculations of geometry-optimized structures. However, because of the complex nature of the model, with active site water molecules and flexible propionate groups, we would first like to discuss a simpler complex in which we can explore the effects of iterative hydrogen bonding.

Figure 4.14 shows a series of simulated NRIXS spectra of ferryl complexes with variants of a tris[N'-*tert*-butyluraylato)-N-ethyl]aminato ($[H_3 1]^{3-}$) ligand, where the *tert*-butylimido groups of $[H_3 1]^{3-}$ have been instead replaced with hydrogens or methylimidos (models in Figure 4.15). Inspiration to use this complex as a model comes from work by the Borovik group, which initially synthesized the complex in 2003, and Green's 2006 work on parameterizing Badger's rule for Fe-O bonds, which included Borovik's complex.[3,26] The model set produced a series of 0 – 3 hydrogen bonds on the ferryl oxygen. In this system, the effects of hydrogen bonding alone without coupled vibrational rotational motions to hydrogen bonding water molecules, or more complex interactions with the propionates, can be explored. We observe a Δ17-20 $cm^{-1}$ of the Fe-O stretching feature with the addition of additional hydrogen bonds. The model without hydrogen bonds demonstrates two Fe-O stretching modes, one at 830 and another at 840 $cm^{-1}$. We observe that the difference between these two vibrational modes is the clockwise or counterclockwise (respectively) orientation of the hydrogen atom wags of the bridging methylenes connected to the proximal nitrogen atom, when viewed through the proximal nitrogen and through the Fe-O bond. This produces the left shoulder of the feature observed in the no hydrogen bonding spectrum (black). The Fe-O tilting region, 300 – 400 $cm^{-1}$, displays splitting based upon the symmetry of the complex. Importantly: hydrogen bonding lengthens the Fe-O bond.

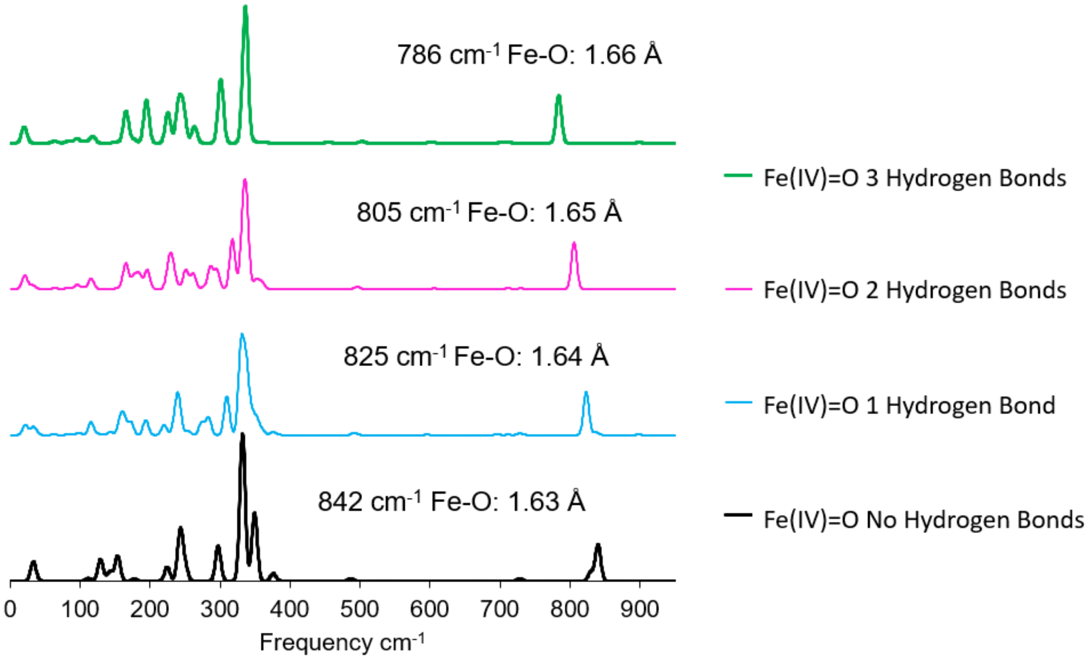

**Figure 4.14**: Simulated Fe-PVDOS spectra for the complexes shown in Figure 4.15. The feature maximum is labeled (786 cm$^{-1}$ etc.) along with Fe-O bond distance determined through Badger's rule analysis at this energy. Calculations were performed in Gaussian 16 at the B3LYP/6-31+G* level.

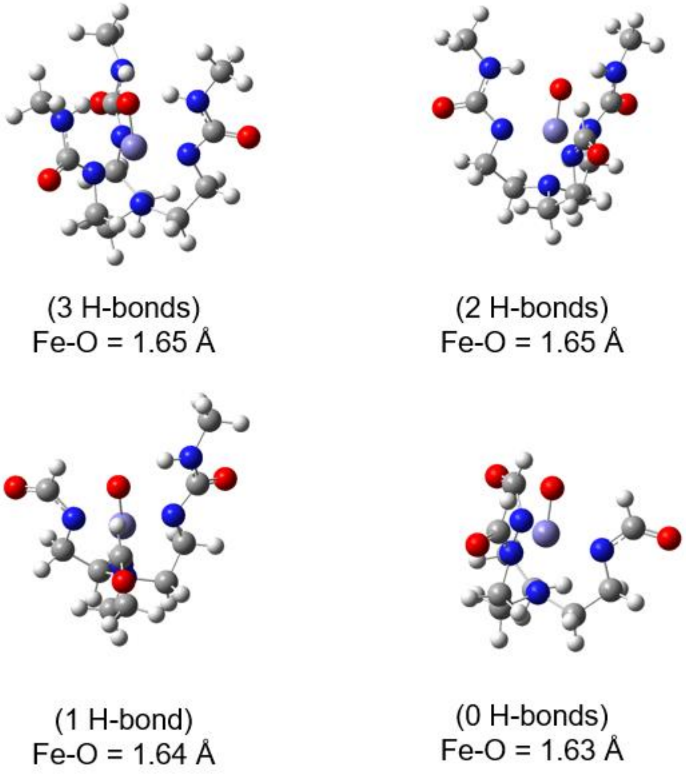

(3 H-bonds)
Fe-O = 1.65 Å

(2 H-bonds)
Fe-O = 1.65 Å

(1 H-bond)
Fe-O = 1.64 Å

(0 H-bonds)
Fe-O = 1.63 Å

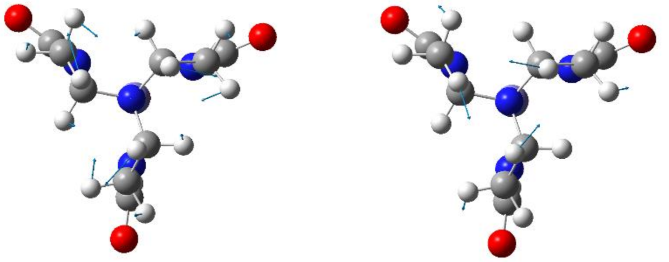

**Figure 4.15**: (Top): This shows the tris[N'-tert-butyluraylato)-N-ethyl]aminato ([H31]3-) ligand, where the tert-butylimido groups of [H31]3- have been instead replaced with hydrogens or methylimidos. Structure geometries were optimized with B3LYP, 6-31+G* in Gaussian 16. The 3 hydrogen-bond model has an Fe-O length of 1.654 Å, while the frequency from the simulated spectrum reflects a 1.66 Å distance using Badger's rule. (Bottom): Fe-O stretching modes of the 0 H-bonding model looking upwards through the N-Fe-O axis. Arrows represent vibrational mode displacement vectors. Left: mode 36 at 830 cm$^{-1}$. Right: mode 37 at 840 cm$^{-1}$.

As discussed earlier, APX contains extensive hydrogen bonding from active site water molecules and amino acid residues. To best simulate these effects, we explored models that included the active site arginine, histidine, and tryptophan residues, along with 2 – 7 water molecules in the active site, in addition to the heme macrocycle and proximal imidazole ligand. These modeling efforts are presented in Figure 4.16. Models began using the geometry from a PDB model of APX-II, 5JQR, generated through X-ray crystallography. For water molecules, only the oxygen atom density was considered, and this was protonated afterwards when constructing the model such that the hydrogen atoms did not start in any hydrogen bonding position. This was to avoid bias of a protonated ferryl species from the report that produced the PDB structure, which we believe to be a misassignment.[27] Optimization was carried out at the B3LYP/6-311G level. We show the spectra in Figure 4.16 to demonstrate alternative hydrogen bonding environments around the general peroxidase's Fe(IV)=O moiety, although for later discussion we focus upon a model containing 7 water molecules that is not included in this figure.

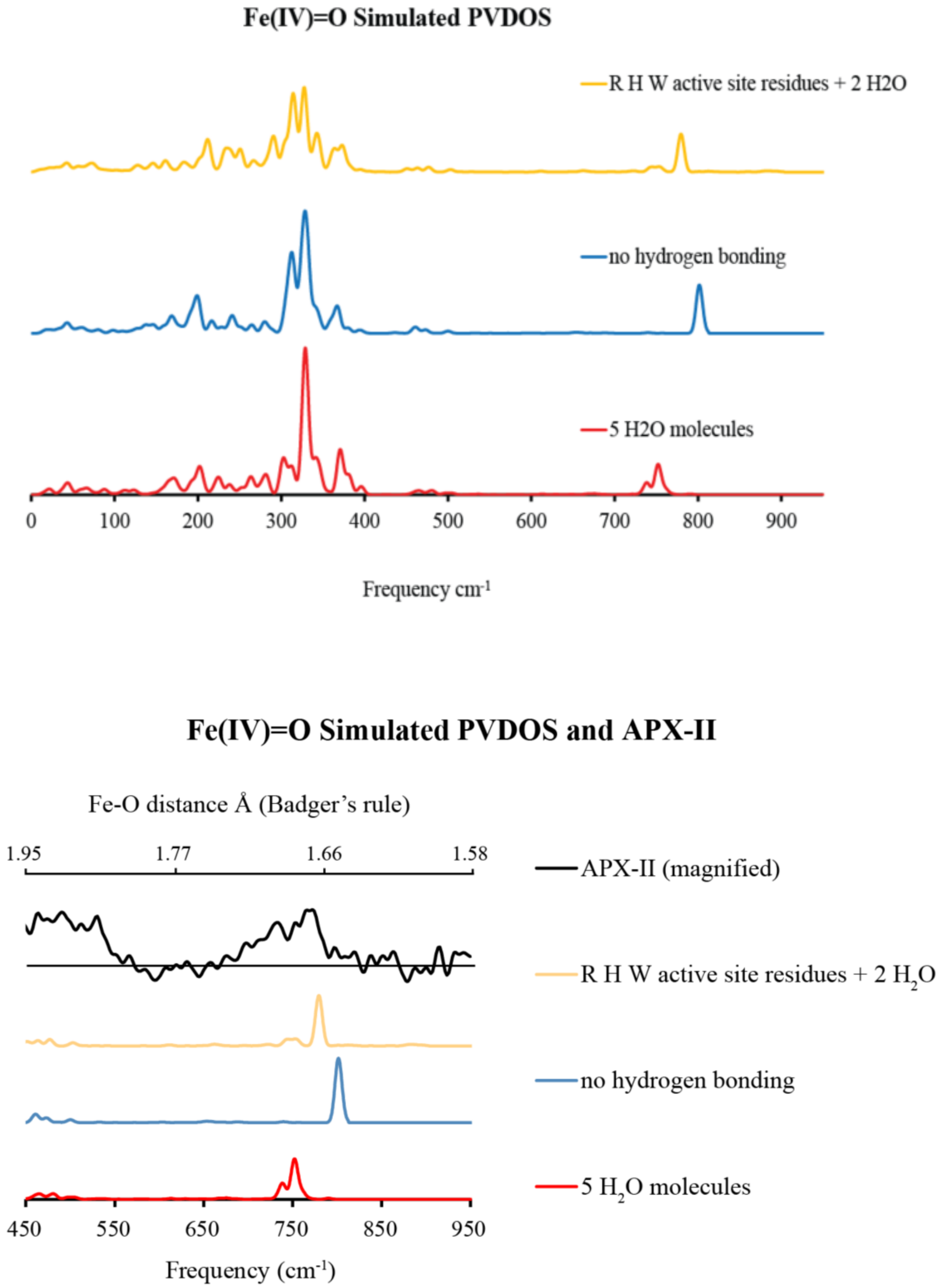

**Figure 4.16**: (Top): Simulated Fe-PVDOS spectra of the models shown in Figure 4.17. Simulations here describe the splitting of the Fe-O feature observed in APX-II. These show the full spectrum of the simulations. (Bottom): Focusing in on the 450 – 950 cm$^{-1}$ region and comparing to experimental APX-II data.

DFT calculations suggest that including the active site water molecules from APX-II's crystal structure can split the Fe-O stretching feature of a histidine-ligated heme model with an Fe(IV)=O in a similar manner to what is seen in the experimental data (Figure 4.16). The bottom part of Figure 4.16 shows a comparison of Fe-PVDOS data for APX-II with Gaussian models with and without the active site water molecules and active site amino acid residues. In the water-free model, the feature at 803 $cm^{-1}$ is a single vibrational mode. This models myoglobin Compound II very well (805 $cm^{-1}$)[14], a system where there is not enough room above the ferryl oxygen for any water molecules to hydrogen bond and contribute to the Fe vibrations. Including 5 of the water molecules from the crystal structure of APX-II as the starting point for geometry optimization instead produces three Fe-O stretching modes at 738, 752, and 761 $cm^{-1}$, reflecting stretches coupled to motions in the active site waters. This presents as two features at 741 and 755 $cm^{-1}$. The water molecules similarly affect the Fe-O tilting motions between 300-400 $cm^{-1}$ to yield a spectrum more similar to the experimental data of APX-II. Notably the water-free model also better reflects published data for Mb-II in the 300-400 $cm^{-1}$ Fe-O tilting range, particularly the splitting between the 313 – 329 – 369 features of the water-free model to the 332, 362 features in Mb-II. Features below 300 $cm^{-1}$ have proven difficult to model but appears to be most sensitive to geometrical changes in the heme structure itself.

The splitting between the Fe-O stretching peaks in the 5 $H_2O$ model is just 14 $cm^{-1}$ (maxima 741 and 755), or 1.68 and 1.67 Å distance. While the splitting alone seen in the spectrum seems that it could be descriptive of APX-II, it is more likely that the APX-II spectrum at pH 7 shows a combination of two hydrogen bonding environments – one supported by an extensive hydrogen bonding network, and one that is not, taking the maxima from both the R H W active site residue

+ 2 $H_2O$ model and the 5 $H_2O$ model together. The position of the dominant peak in the 5 $H_2O$ spectrum closer to the 732 $cm^{-1}$ peak of APX-II than the 770 $cm^{-1}$ peak of APX-II.

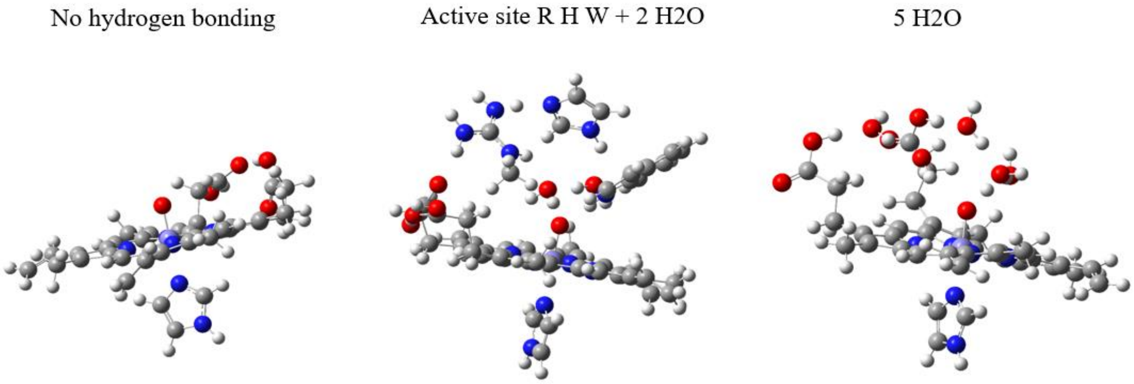

**Figure 4.17**: These are the models used for the above simulations in Figure 4.16. Models started from the PDB: 5JQR for APX-II. Calculations were carried out at the B3LYP/6-311G level. The model with 5 $H_2O$ molecules used the closest water molecules to the ferryl oxygen atom in the structure. The active site R H W + 2 $H_2O$ model uses the closest two water molecules. We note that in the 5 $H_2O$ model, the propionates are participating in the hydrogen bonding network of the water molecules, which is not what is observed in the crystal structure.

To continue our discussion of water molecules splitting the Fe-O stretching mode, we turn to a model from the crystal structure of APX-II that includes the 7 closest water molecules from the active site. The water channel in APX is located clockwise 90° from the propionates (when viewed from above). Supplemental Figure 4.S1 shows the starting and finishing geometries for the 7-water molecule model. We find this is best representative of the stretching modes observed in the Fe-PVDOS spectrum of APX-II. Figure 4.18 shows the full spectrum of this model compared to the no hydrogen bonding model in Figure 4.16, along with a narrowed 700 – 900 $cm^{-1}$ region. We also show the 7-water molecule spectrum when the hydrogen atoms are replaced with deuterium. Our calculations indicate that hydrogen bonding interactions between the ferryl oxygen and the water cluster can mix or spread the Fe-O vibration across multiple normal modes, such that the signal is broadened and the Fe-O stretching envelope intensity is decreased. The 7-water molecule displays Fe-O stretching modes at 785 and 805 cm$^{-1}$. Upon deuteration, there is only a singular Fe-O vibrational mode at 791 cm$^{-1.}$ In both structures, the Fe-O bond distance is 1.67 Å. The 7-water cluster model is shown in Figure 4.19.

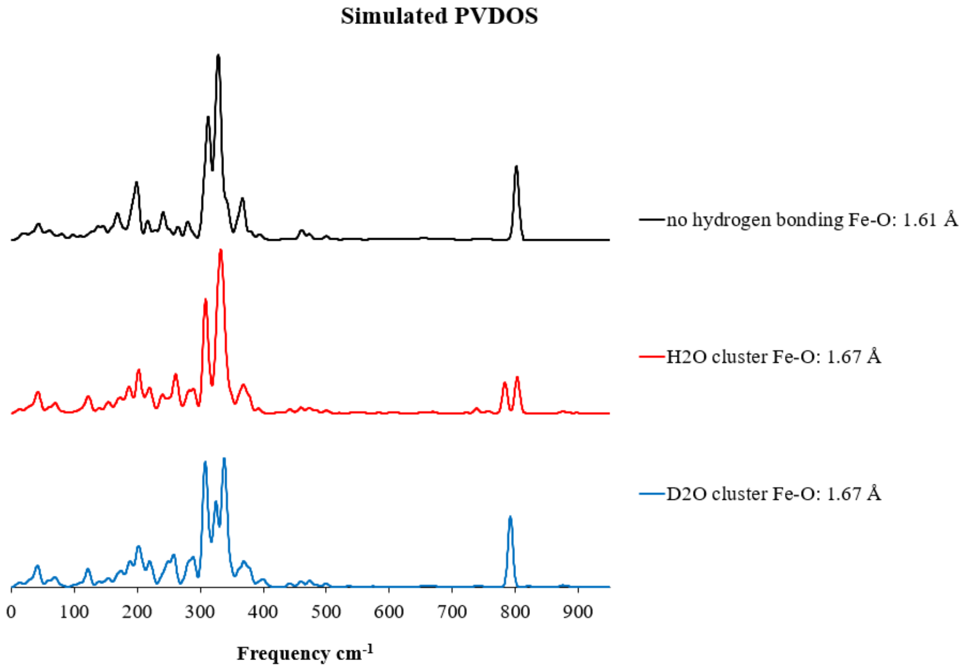

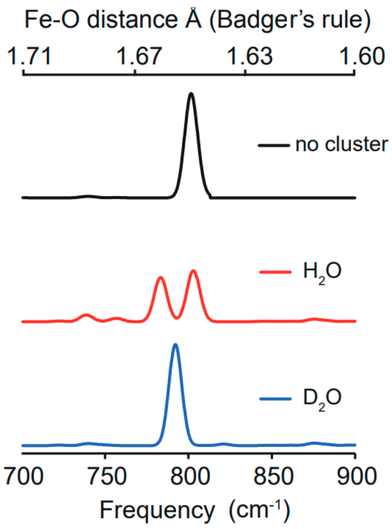

**Figure 4.18**: (Top): Full-range spectra of the 7-water model (red) compared to the model without any hydrogen bonding interactions (black) and the 7-water model, where the $H_2O$ molecules have been replaced with $D_2O$ (blue). (Bottom): Comparison of calculated Fe-PVDOS spectra in the iron(IV) oxo stretching region. Interactions between the ferryl oxygen and a cluster of 7 water molecules spreads the Fe-O vibration among several normal modes. In $D_2O$, the stretching frequency shifts to lower energy due to hydrogen bonding, but there is not significant mixing of the Fe-O vibrational modes with that of the $D_2O$ cluster.

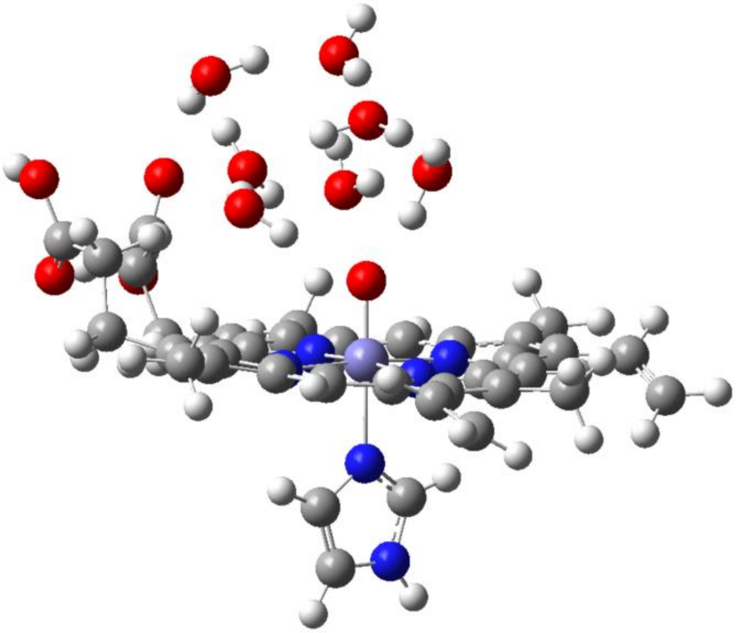

**Figure 4.19**: The 7-water molecule model used for Figure 4.18.

$D_2O$ APX-II experiment:

In order to test the hypothesis that the Fe-O vibrational mode was mixing with active site water molecules, we pursued obtaining the Fe-PVDOS spectrum of APX-II in $D_2O$, as we expect deuteration to produce a single Fe-O feature (Figure 4.18). We prepared $D_2O$ APX-II as we did $H_2O$ APX-II for NRVS, with the exception that we buffer-exchanged APX into 50 mM potassium phosphate pD 7 (measured as pH 7.4 via pH meter), and *m*-CPBA was prepared in a 30% acetonitrile / 70% $D_2O$ solution.

For the $D_2O$ measurement, we used the Mössbauer Jr. style sample holder instead of the *APX rectangular*-style sample holder. This was done so we could cross-verify sample purity via Mössbauer spectroscopy in the same sample holder used for the NRVS experiment, which would allow us to re-examine the sample with Mössbauer after the NRVS experiment and allow us to look for signs of sample reduction or other changes. This, ultimately, was the reason for the significantly lower signal for the $D_2O$ experiment than the $H_2O$ APX-II experiment (~150 Hz counts vs ~300 Hz). The Mössbauer Jr. sample holder does not take advantage of the full beam footprint (~10 x 1 mm), only covering at most 75% of that. Additionally, as discussed in the next section and shown by Table 4.1, the material used for the Mössbauer Jr. sample holders, Delrin, is significantly less penetrable to photons of the relevant energies for an Fe NRVS experiment, further decreasing signal from what was feasible over four days of data collection (APX-II $H_2O$ in 2019) to too little signal to be informative (APX-II $D_2O$ in 2020, Figure 4.20).

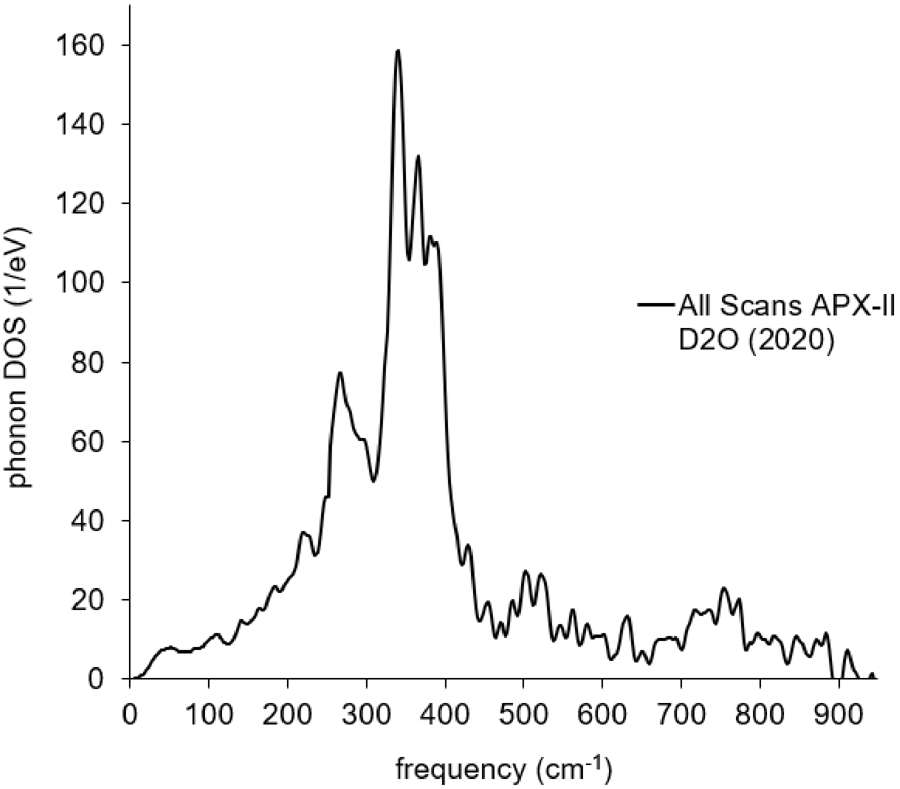

**Figure 4.20**. Fe-PVDOS spectrum of APX-II in $D_2O$, pD 7. Data are from scans summed over four days of collection. APX-II was prepared at 6.66 mM and confirmed in high yield (> 90%) by Mössbauer spectroscopy.

The signal in Figure 4.20 is not sufficient in the Fe-O stretching region to be informative as to the effects of deuteration. Directly comparing data to APX-II in $H_2O$ (Figure 4.21) shows that they loosely look similar to each other, but the signal-to-noise in the $D_2O$ spectrum is not high enough to make features distinguishable. There is something ~750 $cm^{-1}$ in the $D_2O$ spectrum, but the broader 700 – 750 $cm^{-1}$ signal cannot be said to be a discrete feature, nor the sharper peak ~775 $cm^{-1.}$

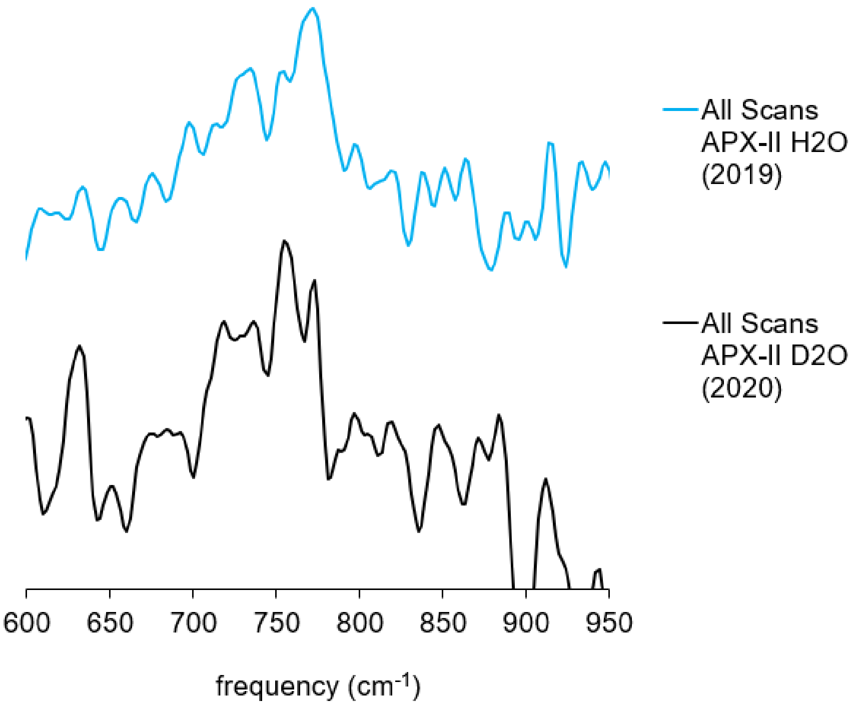

**Figure 4.21**: Comparison of Fe-PVDOS spectra for $H_2O$ and $D_2O$ forms of APX-II in the Fe-O stretching region.

Sample cells for further experiments:

At beamline 3-ID-D of the Advanced Photon Source at Argonne National Lab, the area where the incident beam contacts the NRVS sample with 14.4 keV +/- meV-scale energy is a 1 mm x 10 mm footprint. The *APS rectangular-style* cell used for the APX-II $H_2O$ measurement took advantage of the entire beam footprint to provide all the space with sample. The cell depicted in Figure 4.6 is a larger variant of the cell – there is an alternate version with only a 1 mm groove in the center of the cell, such that less sample volume can be used. This is not very useful for our methods of generally manipulating easily disturbed frozen powder sample under liquid nitrogen. We pursued the Mössbauer Jr. sample holder design because it would use less sample than having to freeze both a standard Mössbauer sample holder (Figure 4.21 design, although standard Mössbauer sample holders have been made of Delrin) and allow for examination of the same exact sample observed by NRVS before and after the experiment.

The smaller size of the Mössbauer Jr. sample holder relative to the Mössbauer Sr. sample holder was because of limitations for the brass adapter piece (Figure 4.7), where the screws that attach the adapter to the cryostat head on at the beamline were too close together to accommodate a full-sized Mössbauer cup. We used the material, Delrin, with the assumption that it would not interfere with the NRVS measurement. Table 4.1 illustrates the mistake in this assumption. An additional problem with this design was that the smaller sample size meant more time on the Mössbauer spectrometer was required to resolve a sufficient spectrum.

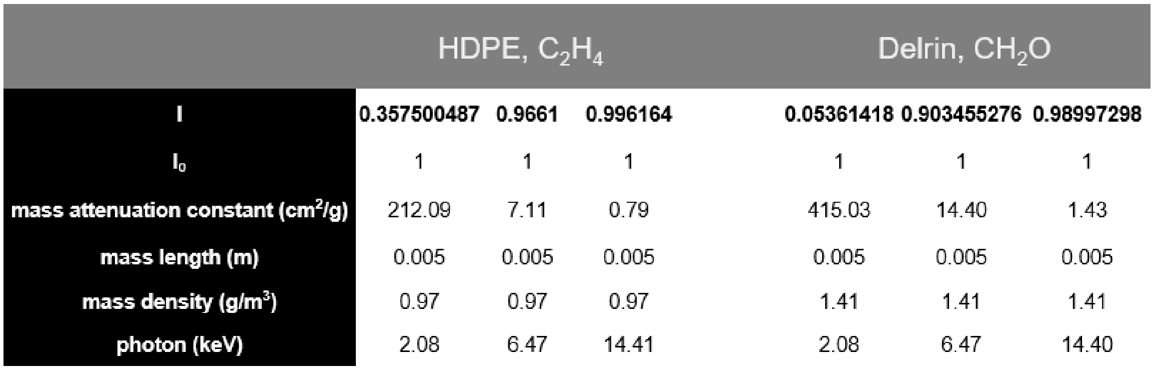

| | HDPE, $C_2H_4$ | | | Delrin, $CH_2O$ | | |
|---|---|---|---|---|---|---|
| **I** | **0.357500487** | **0.9661** | **0.996164** | **0.05361418** | **0.903455276** | **0.98997298** |
| **$I_0$** | 1 | 1 | 1 | 1 | 1 | 1 |
| **mass attenuation constant ($cm^2/g$)** | 212.09 | 7.11 | 0.79 | 415.03 | 14.40 | 1.43 |
| **mass length (m)** | 0.005 | 0.005 | 0.005 | 0.005 | 0.005 | 0.005 |
| **mass density ($g/m^3$)** | 0.97 | 0.97 | 0.97 | 1.41 | 1.41 | 1.41 |
| **photon (keV)** | 2.08 | 6.47 | 14.41 | 2.08 | 6.47 | 14.40 |

**Table 4.1**: Theoretical transmittance calculated for Delrin ($CH_2O$ polymer) and high density polyethylene (HDPE, $C_2H_4$ polymer) for the 6.4, and 14.4 keV photons relevant in an NRVS measurement. The 2 keV photon is included for comparison as it is relevant for a Mössbauer experiment. This assumes a 5 mm thickness, which we note is ten times thicker than the sample holder wall (0.5 mm).

In Table 4.1, we can see theoretical transmittance of photon of 2.08, 6.47, or 14.41 keV through 5 mm of HDPE and Delrin. The 6.4 keV photon is about 6% less transmissible through Delrin than HDPE due to a higher mass attenuation coefficient. We believe this to be one of the contributing factors to the lower count rate (160 Hz) and signal-to-noise observed with the 2020 $D_2O$ experiment, compared to the 2019 $H_2O$ experiment. Transmittance of the incident photon was calculated using exponential attenuation law:

$$\frac{I}{I_0} = exp\left[-\left(\frac{\mu}{\rho}\right)x\right]$$

From which μ is the mass attenuation coefficient, ρ is the mass density, x is the mass thickness, and I and $I_0$ are the emergent photon intensity and incident photon intensity.

In developing the ideal sample holder for Mössbauer and NRVS measurements, we pursued an option that would let us take advantage of the full beam footprint and not reduce our sample volume for Mössbauer spectroscopy. What follows are designs for a HDPE Mössbauer sample holder that matches our standard Mössbauer cup design (Figure 4.21) and the copper adapter piece to attach it to the cryostat at the beamline (Figure 4.22). The wider distance between the screws that attach the adapter (22 mm) requires that a spacer piece be attached between the adapter and the cryostat head (Figure 4.23). For the *APS rectangular-style* and Mössbauer Jr. sample holders, a taller and narrower spacer is used. It is necessary to use the spacer ins Figure 4.23 to allow room for the full height of the Mössbauer Sr. cup at the beamline.

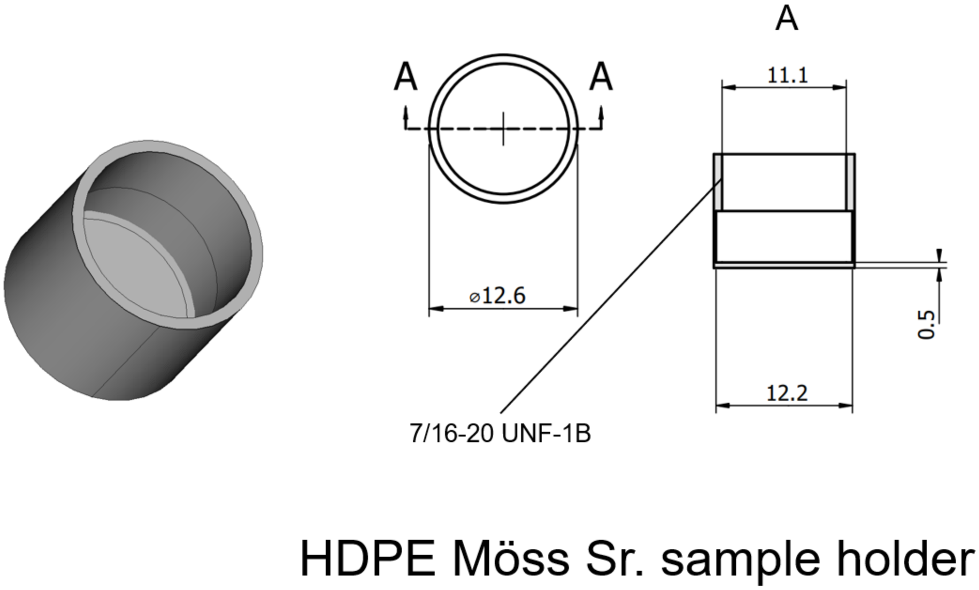

**Figure 4.22**: Mössbauer Sr. cup design. This is the same design used for the standard Mössbauer sample holder, which is typically made of Delrin. A compatible screw top is required for this sample holder. Powdered sample can be scooped in while half- or fully-immersed in liquid nitrogen, or liquid sample can be directly frozen.

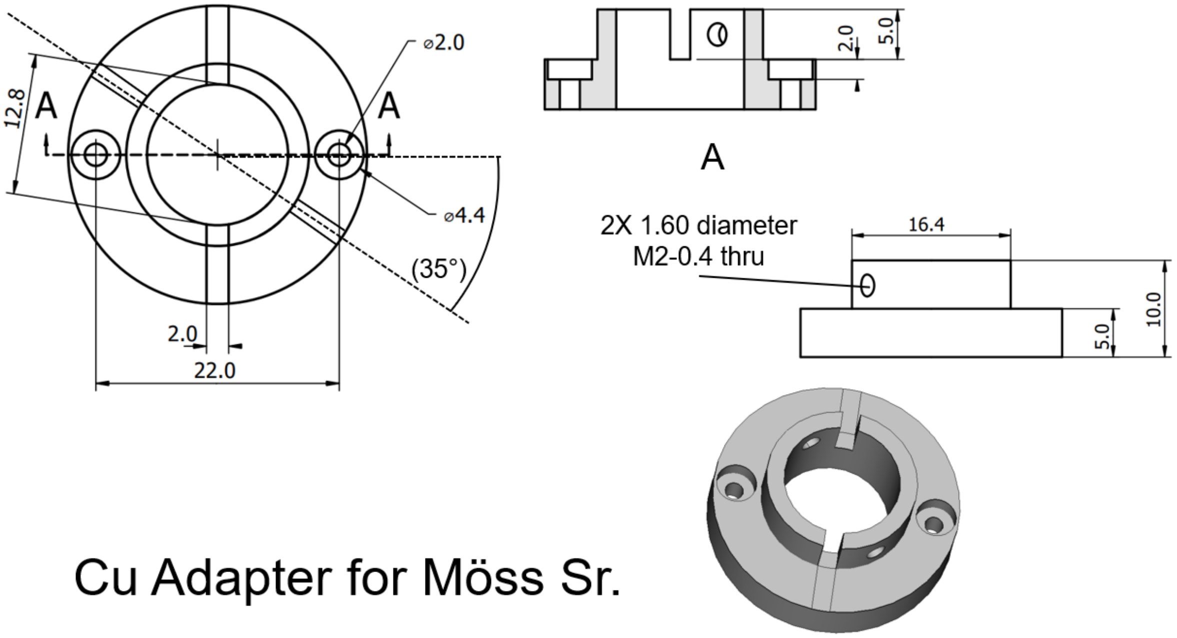

**Figure 4.23**: Adapter piece for Mössbauer Sr. cup. This is designed to hold the standard-dimension Mössbauer cup. Two threaded holes for set screws (M2) are accessible to secure the sample in place and allow for samples to be changed at the beamline without removing the adapter piece. The recessed copper from the bracing ring is to limit background signal during the NRVS measurement. The surrounding metal ring is to keep the sample cold during the experiment and help draw heat into the cryostat from the sample.

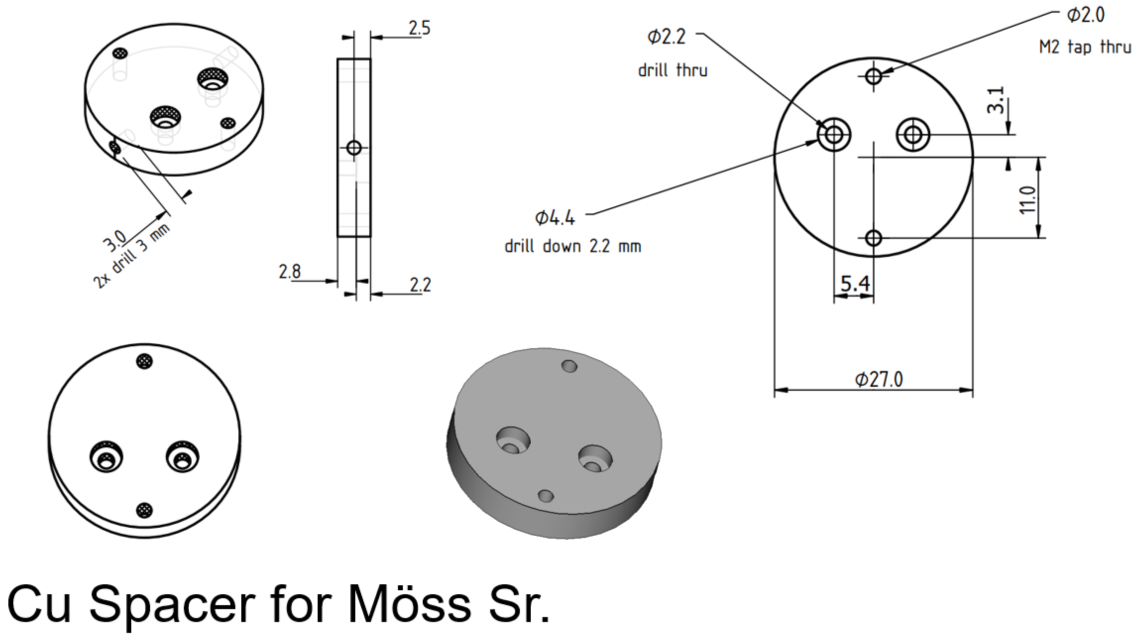

**Figure 4.24**: Spacer part for the Mössbauer Sr. adapter. This is required because of the 22 mm distance for the screws on the adapter piece (Figure 23). The two holes closer to the center of the disc are the securing points for the spacer to the cryostat head.

## Conclusions and Future Directions:

APX-II is an unprotonated iron(IV) oxo species. The Fe-PVDOS spectrum of APX-II unambiguously point to a short Fe-O bond, consistent with what we have detailed in chapter II. The broad vibrational feature in the range associated with Fe(IV)=O stretching (700 – 800 $cm^{-1}$) appears to have two peaks at 732 and 770 $cm^{-1}$, and the width of this vibrational envelope suggests the presence of a distribution of resonances. We believe this is linked to variations in hydrogen bonding interactions between the ferryl moiety and active site molecules at pH 7.

In addition to directly repeating the $D_2O$ APX-II experiment with the new HDPE Mössbauer Sr. sample holders, we believe preparing high- and low-pH forms of APX-II would be informative, along with $^{18}O$ labeling the ferryl oxygen. Scheduling beamtime, however, is the restricting element for more experiments. The four days of data collection required to produce a quality Fe-PVDOS spectrum is the challenge, but this can possibly be reduced to two or three days. Designing approaches to capture reactive intermediates at such high concentrations is challenging. With APX, the highest concentration that can be achieved is approximately 10 mM before the enzyme cannot be readily manipulated with a pipette. The 6.66 mM intermediate APX-II was resolvable in Figure 4.9, but just half the signal in the $D_2O$ sample produced insufficient data (Figure 4.20).

For the biochemist, the answer of how concentrated one’s samples should be for NRVS is straightforward: as high as possible. Having to scale that reaction up to distribute it across multiple sample holders is costly. These standardized sample holders for dual NRVS and Mössbauer should greatly reduce the amount of enzyme used in scaled-up reactions.

## Supplementary Information:

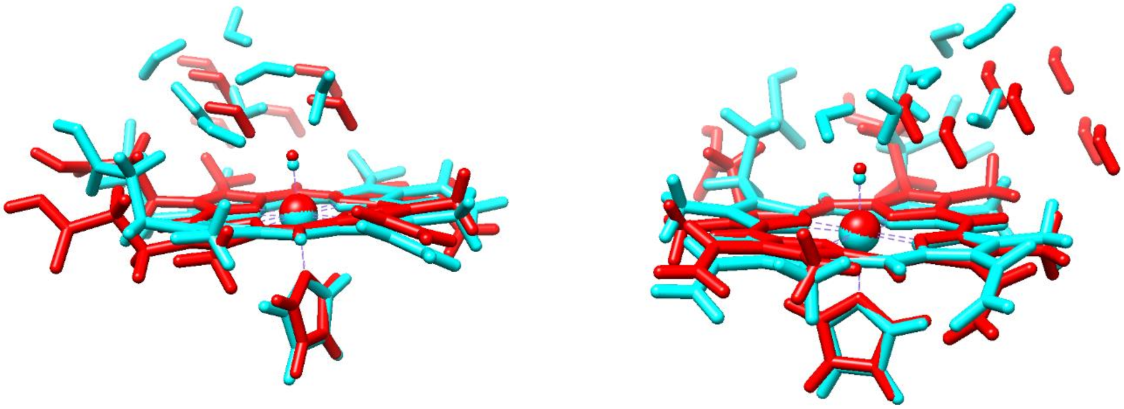

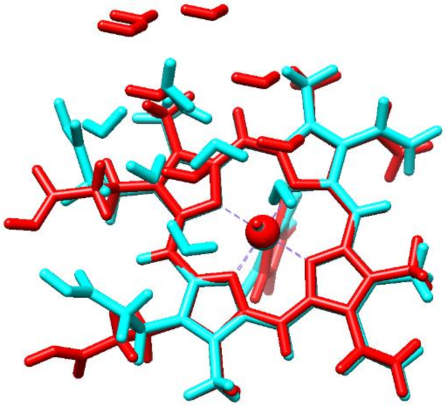

**Figure 4.S1**: The red structure is the starting model before optimization in Gaussian16 (B3LYP/6-311G). The blue structure is the final (optimized) model. The starting atom positions came from APX-II X-ray crystal structure (PDB: 5JQR), pruned down to the heme macrocycle including the propionates, 7 active site water residues (O-atoms), the distal oxygen atom ligand, and the proximal histidine was modeled as an imidazole. Hydrogens were added where necessary.

Images of the beamline:

Advanced Photon Source ring, from the balcony of the User Building.

Outside hutch 3-ID-D in 2019, during the APX-II $H_2O$ experiment.

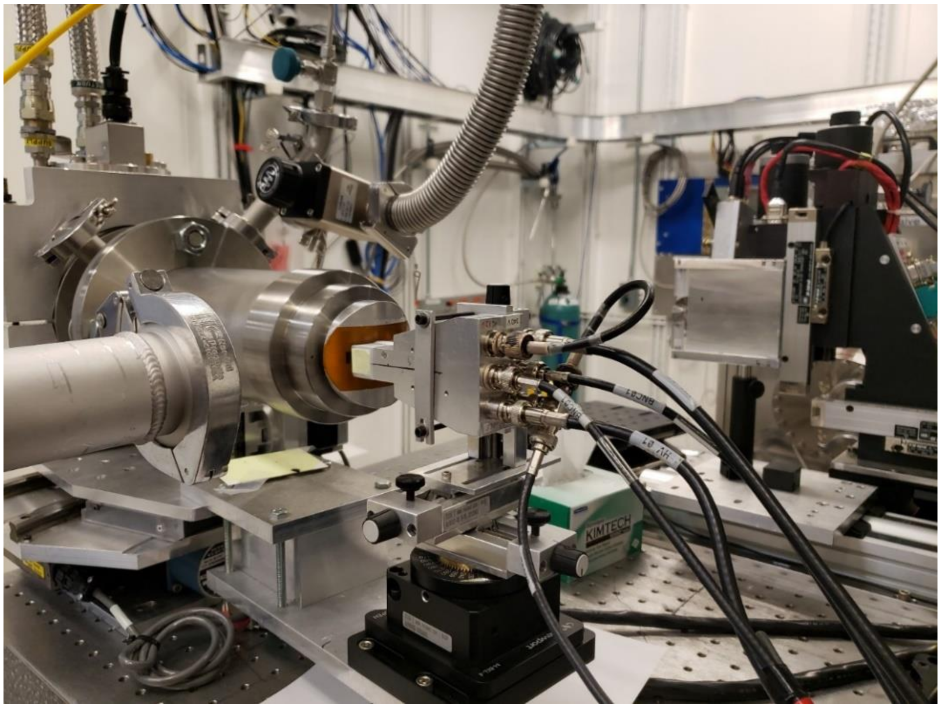

Cryostat and detector of 3-ID-D.

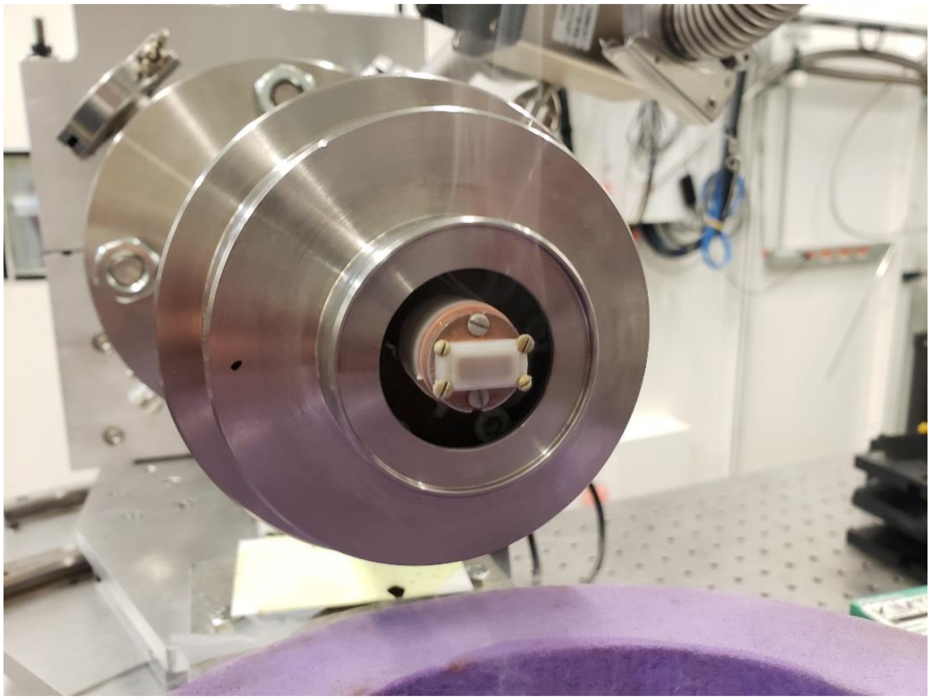

Sample mounted in an *APS rectangular-style* cell, affixed to cryostat head.

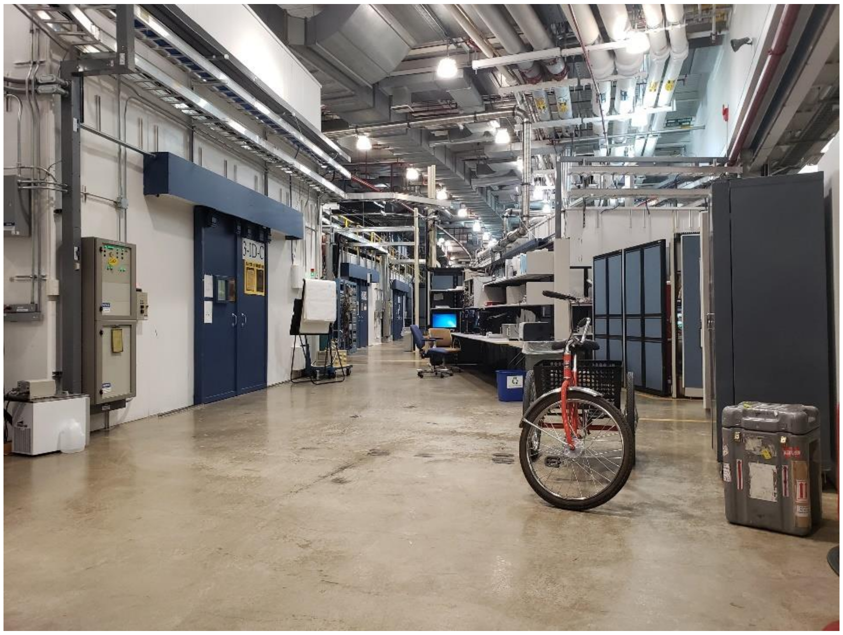

Outside the hutch. APS has bikes!

The hutch, door closed and during operation.

**References:**

1. Robert, B. Resonance Raman spectroscopy. *Photosynthesis Research*. **101** 147–155 (2009).

2. Badger, R. M. The relation between the internuclear distances and force constants of molecules and its application to polyatomic molecules. *J. Chem. Phys.* **3**, 710–714 (1935).

3. Green, M. T. Application of Badger's rule to heme and non-heme iron-oxygen bonds: An examination of ferryl protonation states. *J. Am. Chem. Soc.* **128**, 1902–1906 (2006).

4. Chance, B. *et al.* X-ray absorption studies of intermediates in peroxidase activity. *Arch. Biochem. Biophys.* **235**, 596–611 (1984).

5. Penner-Hahn, J. E. *et al.* X-ray absorption spectroscopic studies of high valent iron porphyrins. Horseradish peroxidase compounds I and II and synthetic models. *J. Biol. Chem.* **258**, 12761–12764 (1983).

6. HASHIMOTO, S., TATSUNO, Y. & KITAGAWA, T. Resonance Raman evidence for the presence of the Fe(IV)=O bond in horseradish peroxidase compound II. *Proc. Japan Acad. Ser. B Phys. Biol. Sci.* **60**, 345–348 (1984).

7. Terner, J., Sitter, A. J. & Reczek, C. M. Resonance Raman spectroscopic characterizations of horseradish peroxidase. Observations of the Fe(IV)= O stretching vibration of Compound II. *Biochim. Biophys. Acta (BBA)/Protein Struct. Mol.* **828**, 73–80 (1985).

8. Sitter, A. J., Reczek, C. M. & Terner, J. Heme-linked ionization of horseradish peroxidase compound II monitored by the resonance Raman Fe(IV)=O stretching vibration. *J. Biol. Chem.* **260**, 7515–22 (1985).

9. Sundaramoorthy, M., Terner, J. & Poulos, T. L. The crystal structure of chloroperoxidase: a heme peroxidase-cytochrome P450 functional hybrid. *Structure* **3**, 1367–1378 (1995).

10. Green, M. T., Dawson, J. H. & Gray, H. B. Oxoiron(IV) in Chloroperoxidase Compound II Is Basic: Implications for P450 Chemistry. *Science.* **304**, 1653–1656 (2004).

11. Wang, H., Alp, E. E., Yoda, Y. & Cramer, S. P. A Practical Guide for Nuclear Resonance Vibrational Spectroscopy (NRVS) of Biochemical Samples and Model Compounds. *Methods Mol Biol.* **1122**, 125–137 (2014).

12. Scheidt, W. R., Durbin, S. M. & Sage, J. T. Nuclear resonance vibrational spectroscopy – NRVS. *J. Inorg. Biochem.* **99**, 60–71 (2005).

13. Sturhahn, W. Nuclear resonant spectroscopy. *J. Phys. Condens. Matter* **16**, 497–530 (2004).

14. Zeng, W. *et al.* Direct probe of iron vibrations elucidates NO activation of heme proteins. *J. Am. Chem. Soc.* **127**, 11200–11201 (2005).

15. Tomita, T., Hirota, S., Ogura, T., Olson, J. S. & Kitagawa, T. Resonance Raman investigation of Fe-N-O structure of nitrosylheme in myoglobin and its mutants. *J. Phys. Chem. B* **103**, 7044–7054 (1999).

16. Wyllie, G. R. A., Schulz, C. E. & Scheidt, W. R. Five- to six-coordination in (nitrosyl)iron(II) porphyrinates: Effects of binding the sixth ligand. *Inorg. Chem.* **42**, 5722–5734 (2003).

17. Hersleth, H. P. *et al.* Crystallographic and spectroscopic studies of peroxide-derived myoglobin compound II and occurrence of protonated $Fe^{IV}$-O. *J. Biol. Chem.* **282**, 23372–

23386 (2007).

18. Powers, L., Chance, M., Kumar, C. & Chance, B. X-ray Absorption Studies of Myoglobin Peroxide Reveal Functional Differences between Globins and Heme Enzymes. *Biochemistry* **25**, 1259–1265 (1986).

19. Weiqiao  Zeng, † *et al.* Synchrotron-Derived Vibrational Data Confirm Unprotonated Oxo Ligand in Myoglobin Compound II. (2008) *J. Am. Chem. Soc.* **130**, 1816-1817 (2008).

20. Weitz, A. C. *et al.* Probing Hydrogen Bonding Interactions to Iron-Oxido/Hydroxido Units by $^{57}$Fe Nuclear Resonance Vibrational Spectroscopy. *Angew. Chemie Int. Ed.* **57**, 16010–16014 (2018).

21. Frisch, M. J. *et al. Gaussian 16*. (2016).

22. Yosca, T. H. *et al.* Setting an Upper Limit on the Myoglobin Iron(IV)Hydroxide pKa. *Jacs* **136**, 9124–9131 (2014).

23. Hashimoto, S., Teraoka, J., Inubushi, T., Yonetani, T. & Kitagawa, T. Resonance Raman study on cytochrome c peroxidase and its intermediate. Presence of the Fe(IV)=O bond in Compound ES and heme-linked ionization. *J. Biol. Chem.* **261**, 11110–11118 (1986).

24. Berglund, G. I. *et al.* The catalytic pathway of horseradish peroxidase at high resolution. *Nature* **417**, 463–468 (2002).

25. Kawabata, T. Detection of multiscale pockets on protein surfaces using mathematical morphology. *Proteins Struct. Funct. Bioinforma.* **78**, 1195–1211 (2010).

26. MacBeth, C. E. *et al.* Utilization of Hydrogen Bonds to Stabilize M-O(H) Units: Synthesis

and Properties of Monomeric Iron and Manganese Complexes with Terminal Oxo and Hydroxo Ligands. *J. Am. Chem. Soc.* **126**, 2556–2567 (2004).

27. Kwon, H. *et al.* Direct visualization of a Fe(IV)-OH intermediate in a heme enzyme. *Nat. Commun.* **7**, 13445 (2016).